Analysis and Design of MEMS-Based Multi-Functional Aperture Antennas

by

Hamid Moghadas

A thesis submitted in partial fulfillment of the requirements for the degree of

Doctor of Philosophy

in

MICRO-ELECTROMECHANICAL SYSTEMS AND NANOSYSTEMS

Department of Electrical and Computer Engineering

University of Alberta

Abstract

Future antennas consist of low-profile smart multi-functional radiating apertures which support multi-beams of multi-bands with multi-polarizations. They can scan the surrounding environment, choose the band of interest and generate the required beam shape. Such antenna can be utilized in numerous emerging applications such as vehicular satellite communication, software defined and cognitive radio, and also next generation of mobile networks (5G). This thesis develops MEMS-tunable orthogonally-polarized dual-band Resonant Cavity Antennas (RCA) and also reflectarrays as platforms for future multi-functional aperture antennas.

As an initial prototype, a high gain orthogonally polarized dual broadside beam RCA is designed, fabricated and measured. Also, an equivalent transmission line model and a design flow chart are extracted for the RCA in order to understand the dual band beam forming and facilitate the quick design. Furthermore, the independence and the arbitrary separation of the operating bands is demonstrated.

Next, a MEMS-tunable RCA is designed, fabricated and measured with an upper band vertically polarized broadside beam and a lower band horizontally polarized beam which is switched among all possible beam shapes of leaky wave antennas, i.e., broadside, symmetric conical, and also an asymmetric single beam which is either frequency scanned or steered at fixed frequency. Traditionally, a Full Phase-Gradient (FPG) Partially Reflective Surface (PRS) has been used in an RCA for generating beams off broadside. A FPG-PRS is a non-uniform aperture where a continuous phase gradient is applied between adjacent cells in the whole PRS. Here, the novel configuration of Half Phase-Gradient (HPG) PRS was offered where the phase gradient is applied between adjacent cells in half of PRS in order to utilize the inherent leaky wave phase progress inside the cavity. The HPG-PRS provides enhanced scan profile, faster real time tracking, and reduced DC power consumption which are all critical in wireless, space and military applications. Furthermore, a novel model is extracted for calculating the radiation of such RCAs with non-uniform

aperture and verified by comparison with measurements. This model can be applied to any leaky wave antenna with arbitrary unit cell shape and periodicity. Finally, the unit cell required for the beam shaping RCA is realized by hybrid integrated MEMS switches.

In the field of reflectarrays however, a phase tunable low loss double slotted patch reflective unit cell is designed and simulated for operation at 12 GHz with vertical polarization and 14 GHz with horizontal polarization for Ku band mobile satellite communication. The phase tuning is facilitated using an array of switches across both slots in order to dynamically control the equivalent slot length. A monolithic custom fabrication process is developed for fabrication of the proposed reflectarray unit cell with MEMS switches. Finally, this unit cells is measured inside a waveguide setup with DC bias pads to verify the phase tuning.

Preface

This thesis is an original work by Hamid Moghadas.

Chapter 2 of this thesis has been published previously as:

1. H. Moghadas, M. Daneshmand, P. Mousavi, A dual-band high-gain resonant cavity antenna with orthogonal polarizations, IEEE Antenna and Wireless Propagation Letters, vol. 10, pp. 1220-1223, 2011.

2. H. Moghadas, M. Daneshmand, P. Mousavi, Dual-band high-gain resonant cavity antenna with orthogonal polarisation using slotted patch partially reflective surface, electronic letters, vol. 48, no. 15, pp. 897-899, July 2012.

3. H. Moghadas, M. Daneshmand, P. Mousavi, Single-layer partially reflective surface for an orthogonally-polarised dual-band high-gain resonant cavity antenna, IET Microwaves, Antennas and Propagation 7.8 (2013): 656-662.

Acknowledgements

I am indebted to many people without whose support this thesis would not have been possible. First of all, I would like to express my gratitude to my supervisors, Dr. Mojgan Daneshmand and Dr. Pedram Mousavi for their continued support during the course of my PhD program. I would also like to thank the members of my supervisory committee, Dr. Vien Van and Dr. Kambiz Moez and my examining committee, Dr. mark freeman and Dr Ahmed Kishk for their careful reading of the thesis and for their valuable comments and suggestions.

Also, I wish to thank Collin Twanow (Vice President of Engineering at Micralyne Corp.) for answering all my non-stop questions about fabrication and process development during my experience in NanoFab facility.

My heartfelt appreciation goes to the many friends I made here in Edmonton and at the University of Alberta, especially Dr. Moslem Noori and Dr Mohsen Hajiloo. Their friendship has made my years here enjoyable.

Last, but not least, I wish to thank my parents, **Sedigheh** and **Ahmad**, my sister, **Samineh**, and my brother, **Mammad**. I am forever in their debt for their support throughout my life. I have been extremely fortunate to always have them.

Table of Contents

List of Tables

List of Figures

xiii

xiv

List of Abbreviations

Abbreviation	Description	First use
RCA	Resonant Cavity Antenna	6
EBG	Electromagnetic Band Gap	6
RF	Radio Frequency	3
MEMS	Micro Electro Mechanical System	3
LWA	Leaky Wave Antenna	3
PRS	Partially Reflective Surface	6
TEM	Transverse Electro Magnetic	8
TE	Transverse Electric	73
TM	Transverse Magnetic	61
HPG	Half Phase Gradient	55
FPG	Full Phase Gradient	55
$V - pol$	Vertically Polarized	26
$H - pol$	Horizontally Polarized	26
PECVD	Plasma Enhanced Chemical Vapour Deposition	75
RIE	Reactive Ion Etching	76

Chapter 1

Introduction

1.1 Definition of Problem

Future antennas are smart multi-functional radiating apertures which support multi-beams of multi-bands and multi-polarizations. They can scan the surrounding environment, choose the band of interest and generate the required beam shape. Such antenna can be utilized in numerous emerging applications such as mobile two way connectivity, vehicular satellite communication (Fig. 1.1), commercial aviation, software defined and cognitive radio, and also next generation of mobile networks (5G). As an example, if a car is driven on a road without cell-phone coverage, the car antenna needs to find the beam of a satellite in order to connect and transmit or receive data. These applications require low profile antennas which are not only operational in two orthogonally polarized bands, but also capable of independent beam forming in each band for sensing and tracking purposes. The major specifications required for these apertures are:

- low cost

- low profile, planar

- supporting dual bands of linear and orthogonal polarization

- beam forming and beam steering ability providing broadside, azimuthally symmetric conical, asymmetric single beam off broadside

The antenna design starts with selecting the antenna types which are easily fabricated and satisfy the physical features. Then, different technical specifications are added to the antenna step by step.
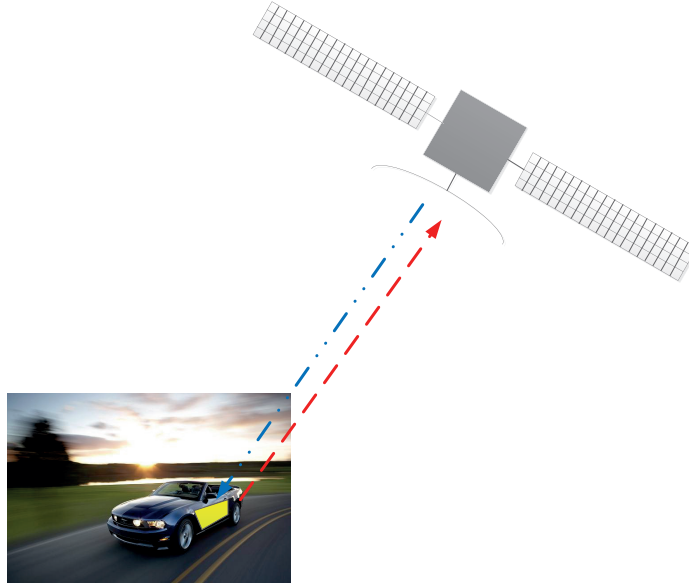
Figure 1.1. Vehicular two-way satellite communication [1].

1.2 Traditional Solution to the Problem

Phased array antennas are able to synthesize various beam shapes [2]. An antenna array is a collection of similar or different radiating elements. The total radiation of this collection depends on the radiation of each individual element and can be totally different from the constructing elements. The arrays are widely used due to their improved radiation gain and beam forming capacities. In a phased array, beam forming requires a phase shifter and an amplifier at each element for adjusting the radiating phase and amplitude of the element (Fig. 1.2). However, the phase shifters are nonlinear and the design of active circuitry adds to the product cost. Besides, a portion of the signal is attenuated in long transmission lines connecting the power generator to radiating elements. This motivates the search for other types of planar aperture antennas without phase shifters and different feeding type to reduce the signal loss. Nevertheless, the idea of collecting an array of individual radiators can be an effective way of solving the problem of antenna design for multi-functional apertures.

1.3 Potential Solution to the Problem

A major drawback of phased arrays is the signal loss in transmission lines connecting the power generator to each radiating element. Spatial power combining can be
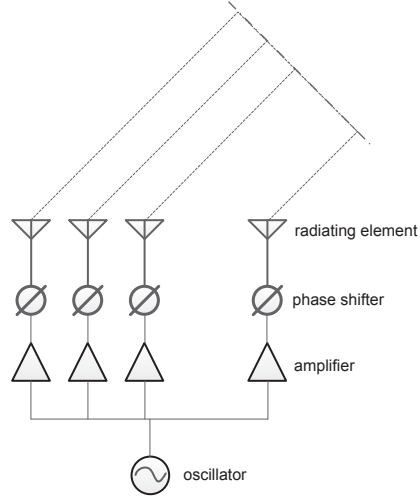
Figure 1.2. Schematic of a phased array with radiating elements, phase shifters, amplifiers and an oscillator. A phased array can scan its beam to a desired angle.

used to obviate the signal loss that occurs in the feeding network. Since regular transmission lines are not used in spatial power combining, the problem of matching the impedance of each element to its line and finally all the lines to the generator is eliminated. Two types of antennas with spatial power combining are the leaky wave antennas (LWA) and the reflectarrays. Both of these types of antennas have the array format and have been used for synthesizing different beam shapes.

Also, as a substitute to phase shifters, tuning elements can be integrated into the antenna radiating elements. Two common technologies for fabrication of the tuning elements are solid state and Radio Frequency (RF) Micro Electro Mechanical System (MEMS) .

1.3.1 Leaky Wave Antennas

Leaky wave antennas are planar and low profile aperture radiators that use spatial power combining, and consist of a group of single elements which can be individually controlled [3,4]. A leaky wave antenna has a waveguide-like structure that supports a leaky wave with complex propagation constant $k_{LW} = \beta - j\alpha$ where β is the phase constant and α is the leakage rate [5]. The leakage of the wave travelling inside the structure illuminates the radiating aperture. The most basic characteristic of the leaky wave antennas is the beam which is scanned with frequency. The scan angle (θ) for a weakly attenuated leaky wave ($\alpha \ll \beta$) depends on its phase constant through the approximate formula $\theta = \arcsin(\beta/k_0)$ where k_0 is the phase constant
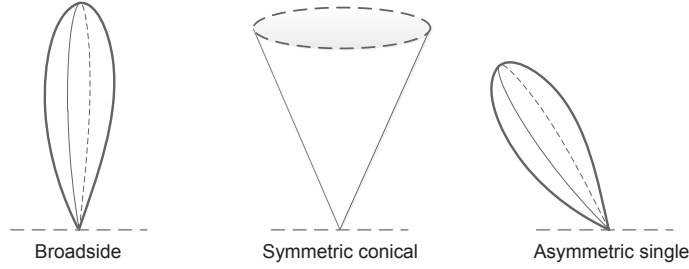
Figure 1.3. Different types of beams generated by RCA: Single broadside beam; cross-section of symmetric conical beam; asymmetric single beam off broadside.
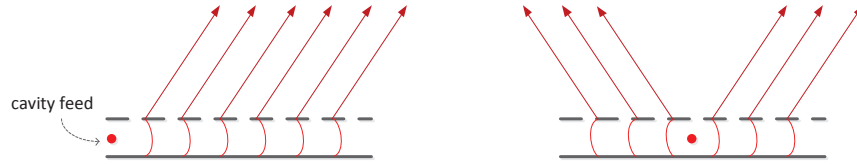
Figure 1.4. Different geometries of leaky wave antennas based on its excitation: feeding from one edge; feeding from center.

of wave propagation in free space at the frequency of operation [6, 7]. Generally, both β and α depend on the geometry of the antenna.

The radiating aperture of a leaky wave antenna consists of an array of metal patches which can be fabricated using simple and low cost printed circuit board technology. To add the beam forming capability, the characteristics of the radiating aperture should be controllable. Hence, each metal patch could be integrated with tuning elements.

Generally, leaky wave antennas are known to generate three different types of beams (Fig. 1.3) depending on their operating frequency and where the aperture is fed (Fig. 1.4); The leaky wave antennas that are fed from one end can generate a broadside beam or scan an asymmetric single beam with frequency [8–10]. However, the leaky wave antennas that are fed from center, can generate a broadside beam or a frequency scanned azimuthally symmetric conical beam. Resonant Cavity Antennas (RCA) are a common type of center fed leaky wave antennas which have a high potential to meet the specifications required by the above-mentioned applications.

1.3.2   Reflectarrays

Microstrip reflectarray antennas are the flat versions of conventional dish antennas with benefits of easy fabrication and tunability [11, 12]. A reflectarray includes an array of patches printed on a dielectric laminate with a ground plane, which are

4
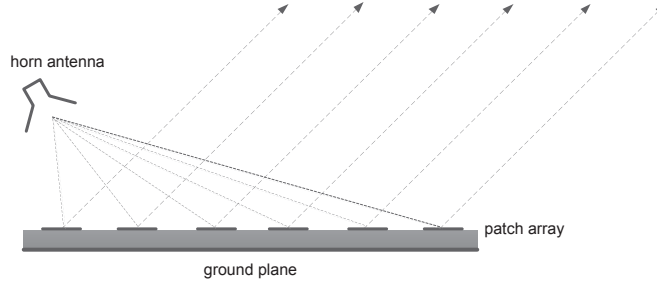
Figure 1.5. Schematic side view of a reflectarray.

usually illuminated by a horn antenna (Fig. 1.5). The radiation of the horn can be redirected to a specific angle by adjusting the reflection of each unit cell of the array. The overall directivity of this aperture antenna depends on the number of cells (panel size) and the accuracy of synthesis of the required reflection phase across the panel [13].

The reflection of unit cells is basically defined by the shape and size of patches. Previously, rectangular, circular and cross shaped patches with variable size or variable stub length have been offered [14]. Also, slotted patches have been proposed where the patch size is constant and the slot size varies over the reflectarray panel [15].

1.3.3 Tuning Elements

MEMS and solid state are the two options as the proposed technology of fabrication of tuning elements. In present thesis, MEMS is preferred since it outperforms solid state technology in terms of DC power consumption, nonlinear effects such as intermodulation distortion and also loss. Tuning elements can be either monolithic or hybrid integrated into antenna radiating aperture.

In the hybrid technique, the tuning elements are fabricated separately and then wirebonded into the radiating elements. In the design, the equivalent inductor and resistor of the wirebonds should be considered since these parasitic circuit elements can affect the antenna radiation.

But in monolithic technique, the tuning elements and the antenna radiating elements are fabricated in a single process together on the same wafer. Since the wafer size is limited to four inches for most of fabrication tools, the total size of tunable monolithic-integrated antennas is limited.

1.4 Resonant Cavity Antenna (RCA)

RCA is a type of leaky wave antenna which consists of a Partially Reflective Surface (PRS) parallel to a solid ground plane fed by a source between the two surfaces (Fig. 1.6) [16,17]. The source excites a cylindrical wave inside the cavity which leaks out of PRS and leads to RCA radiation. The PRS radiating aperture is composed of a uniform or nonuniform array of unit cells which could be hybrid or monolithic integrated with micro tuning elements to allow tuning and beam steering. Various structures have been used as the PRS including 3D multi-layer dielectric slabs, 3D volumetric Electromagnetic Band Gap (EBG) structures, and 2D dielectric laminate with metal-type implants [16, 18–24]. Among them, the 2D structures with metal-type implants are the easiest to fabricate.

1.4.1 RCA principle of operation

There are different methods for explaining the RCA principle of operation such as ray tracing [17] and unit cell dispersion [5]. These two methods are elaborated as follows:

Ray Tracing

In ray tracing method, the RCA is assumed as a resonant microwave cavity. According to ray tracing, the cavity resonates and produces a highly directive broadside pattern if the zero-th and the first order reflection of rays radiated by the source are in phase (Fig. 1.6). The phase of first order reflected ray is affected by PRS reflection phase ($\angle\Gamma$), propagation delay from PRS to ground ($-k_0 h$), ground reflection phase ($-180°$), and propagation delay from ground to PRS ($-k_0 h$) respectively. Hence, the phase difference (Ψ) between the zero-th and the first order reflected ray will be

$$\Psi = \angle\Gamma - k_0 h - 180° - k_0 h \tag{1.1}$$

where k_0 is the propagation constant in free space. To apply the resonance condition, Eq. 1.1 should be equal to integer multiples (N) of $360°$. Hence, the cavity height is calculated as:

$$h = \frac{c}{4f}(2N - 1 + (\frac{\angle\Gamma}{180°})) \tag{1.2}$$

where c is the light speed, f is the resonant frequency, N is an arbitrary integer number and $\angle\Gamma$ is the PRS reflection phase in degrees. In this method, the wave
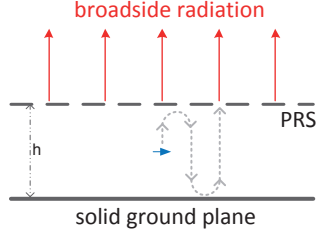
Figure 1.6. Ray tracing of the zero-th and first order reflection of rays radiated by the source.

characteristics of source electromagnetic radiation is ignored. To design a dual band RCA, the resulting resonant height should be the same for both operating band/polarizations.

Unit Cell Dispersion

Initially, the RCA height is calculated based on Eq. 1.1 for a broadside beam at its resonant frequency. At higher frequencies and with the same resonant height, RCA generates a frequency scanned azimuthally symmetric conical beam. This beam scanning is explained by the equation $\theta = \arcsin(\beta/k_0)$ which is generally presented for leaky-wave antennas. The cylindrical wave launched between the solid ground plane and the PRS can leak out because the PRS reflection amplitude is not equal to one (Fig. 1.7). The PRS reflection amplitude ensures that the leakage rate is small enough ($\beta \gg \alpha$). The eigenmode analysis of RCA unit cell (including PRS cell and the ground plane underneath) which is available in most commercial electromagnetic simulators can calculate β and α versus frequency (dispersion curve) in order to inspect the radiation pattern.

The dispersion curve is based on the concept of space harmonics. Consider a sample periodically loaded waveguide with unit cell periodicity of P and transmission direction of y. If the cross-sectional dependence and time variations, $e^{j\omega t}$ of the wave function are suppressed, Floquet theorem describes the wave function as

$$\Pi = \exp(-jk_0 y)F(y) \tag{1.3}$$

where

$$F(y + P) = F(y) \ . \tag{1.4}$$

Eq. 1.3 and 1.4 state that the field behavior is explained by a travelling wave component ($\exp(-jk_0 y)$) with propagation wavenumber k_0 and a standing-wave com-
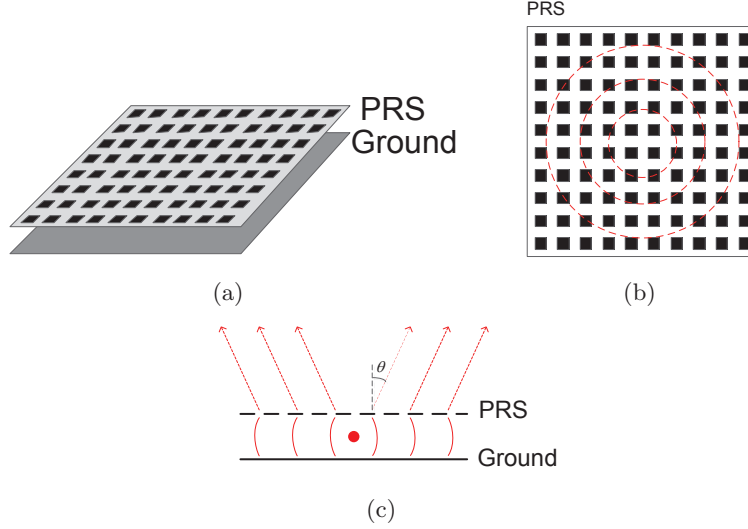
Figure 1.7. (a) Schematic of an RCA with PRS and ground plane. It is excited by an isotropic source at the center of RCA. (b) Top view of PRS demonstrating the cylindrical wave-front. (c) Side view of RCA demonstrating the leakage of waves through PRS.

ponent $(F(y))$ which is similar in all unit cells. If the Fourier series expansion of F,

$$F(y) = \sum_{n=-\infty}^{+\infty} F_n \exp(-j\frac{2n\pi}{P}y) \tag{1.5}$$

is inserted into Eq. 1.3, we get

$$F(y) = \sum_{n=-\infty}^{+\infty} F_n \exp(-jk_n y) \tag{1.6}$$

where

$$k_n = k_0 + \frac{2n\pi}{P}, \quad n = 0, \pm 1, ... \tag{1.7}$$

which shows that the field comprises an infinite number of traveling components which are each called a space harmonic and do not exist independently. Dispersion diagrams are the graph of frequency versus real (β) and imaginary (α) parts of the complex propagation wave-number k_n. Since the free space propagation constant, k_0, is proportional to the frequency, sometimes k_0 is preferred to f. In order to inspect the effect of space harmonics on the dispersion, initially an air-filled Transverse Electro Magntic (TEM) line is considered. The dispersion curve of an unloaded air-filled TEM line is depicted in Fig. 1.8(a) where the solid lines with slope 1 and -1 represent the wave propagating toward positive and negative y direction respectively.

8

However, this curve changes to Fig. 1.8(b) when the line is loaded with periodicity in a way that the initial structure is not totally perturbed. It is assumed here that the loading does not cause the interaction of space harmonics. However, in practice, the coupling of different space harmonics deviates the straight lines to curves depending on the type of coupling; Fig. 1.9(a) and Fig. 1.9(b) depict the directional coupler and the stop-band behavior in coupling of space harmonics respectively.

(a)   (b)
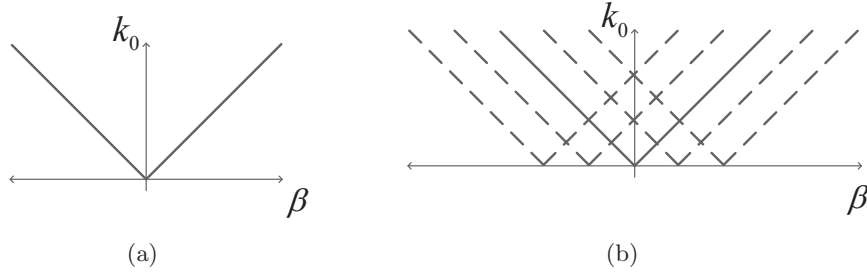
Figure 1.8. The dispersion curve of an air-filled (a) unloaded (b) loaded TEM waveguide.

(a)   (b)
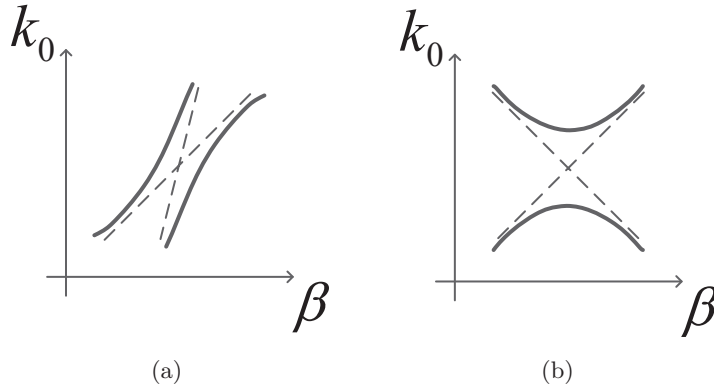
Figure 1.9. (a) Directional coupler and (b) stop-band behavior in coupling of space harmonics.

1.4.2 Dual-band Operation of RCA

Dual band operation of RCA has received great attention [22–31], while little effort has been put into developing RCAs where the polarization of each band is orthogonal to the other.

The current literature on linearly polarized dual band RCAs with 2D printed PRS can generally be divided into two groups. The first group uses two metallic printed periodic structures in the form of either two single sided PRSs [22,23,25,26], one double sided PRS [24], or using one single sided PRS and one artificial magnetic
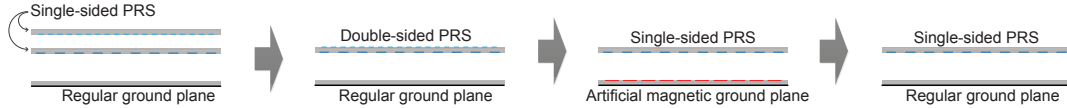
Figure 1.10. Different structures for dual-band RCA: two single-sided PRS; one double-sided PRS; single-sided PRS and artificial magnetic ground plane; one single-sided PRS.
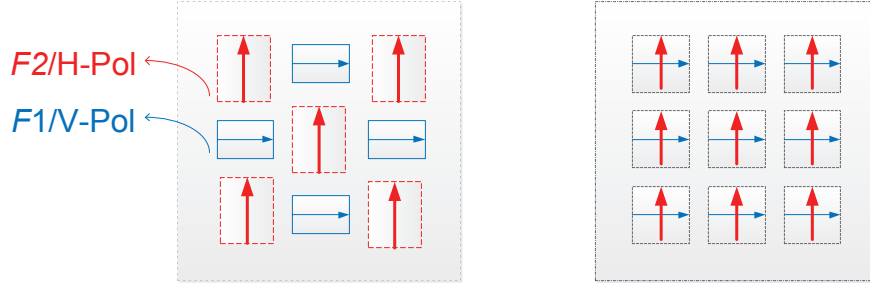
Figure 1.11. Single-sided PRS: interlaced single-polarized single-band cells; orthogonally-polarized dual-band cells.

ground plane (Fig. 1.10) [27]. In these configurations, having two periodic structures produces complication in design, assembly and increases the mass production cost. This has motivated the second group of studies to focus on using one periodic structure in the form of one single-sided PRS [28, 29]. Having one single sided PRS is most desirable because of the advantages of easier fabrication, lower cost, less thermal issues and higher compatibility in monolithic integration with tuning elements such as Micro Electro Mechanical System (MEMS) devices. For instance, [28] offers a slot array PRS with dual bands of the same polarization. To have bands of orthogonal polarizations, authors in [29] suggest interlacing single polarized single band unit cells where the cells operate either at the lower band with vertical polarization (f_1/V-pol) or at the upper band with horizontal polarization (f_2/H-pol) (Fig. 1.11). This, results in large spacing between the cells corresponding to each frequency/polarization (f/pol) and leads to higher grating lobes. Besides, the RCA gain drops in each f/pol, since only about half of the radiating area is assigned to each f/pol. Notably, this concept has previously been explored in reflectarray antennas [32], but to our knowledge, it is not utilized in PRS. Designing orthogonally-polarized dual-band single-layer single-metallization PRS unit cell design has its novelty since the principles and the reflection characteristics of PRS cells are totally different from reflectarray cells.

To date, there is no report of arbitrarily and independently-controlled orthogonally-
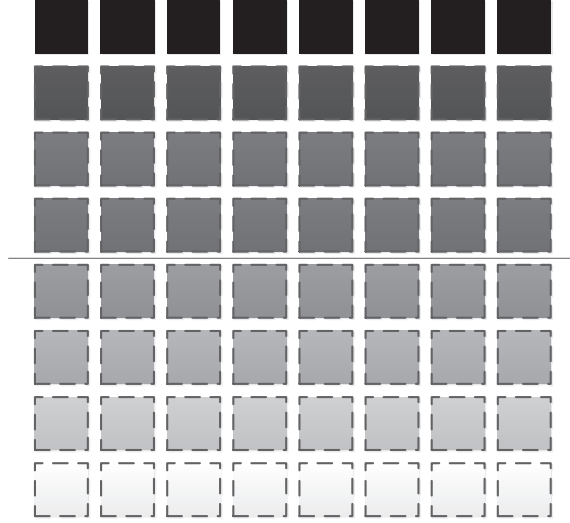
Figure 1.12. Phase gradient across a FPG-PRS. The unit cell phase is assigned to the spectrum between black and white.

polarized dual-band RCAs in literature.

1.4.3 RCA Radiation Pattern

For some applications, beam steering should occur at a fixed frequency since specific communication bands are assigned to transmission and reception. In order to steer the beam at fixed frequency, tuning elements should be integrated into PRS cells. One technique for beam steering at fixed frequency is using a tunable Full Phase-Gradient (FPG) PRS where a progressive phase shift is applied between adjacent unit cells across all PRS cells [33–36]. Fig. 1.12 demonstrates a FPG-PRS where the phase gradient is applied to it from top to bottom and the unit cell phase is represented by the color spectrum between white and black. Solid state varactors and MEMS switches have recently been reported for realizing broadside frequency-reconfigurable and broadside beamwidth-reconfigurable RCA [37–40].

1.5 Reflectarrays

1.5.1 Dual-band Operation of Reflectarray

Various methods are suggested for realizing dual-band/dual-polarized reflectarrays. The first method is interlacing reflective unit cells of different frequency/polarizations (f/pol) over one dielectric layer (Fig. 1.13(a)). This method suffers from emergence of grating lobes and the reduced radiation efficiency [32, 41]. The second method

11

is stacking two reflective layers of different f/pol (Fig. 1.13(b)) [42, 43]. In this method, the MEMS tuning elements can not be integrated in cells that are between two dielectric layers because of their electro mechanical actuation that requires displacement of a beam. The third method uses rings of different f/pol in a single cell (Fig. 1.13(c)) [44]. In this method, the bands are not arbitrarily controlled since the ring lengths and their corresponding bands have to be far apart. Furthermore, in both ring and stacking methods, the mutual coupling between elements of each f/pol deteriorates their independence. We have inspected the dual band operation of reflectarray in previous publications and developed novel unit cells providing independent orthogonally polarized dual bands (Fig. 1.13(d)) [45–47]. [32] presents a single layer reflective unit cell with orthogonal linear polarizations of the same frequency.
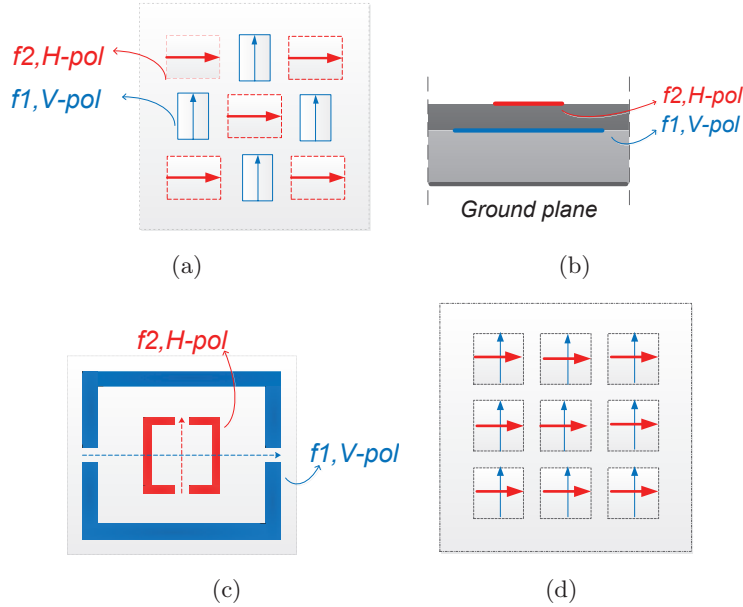
Figure 1.13. Different method for realizing dual-band and dual-polarized microstrip reflectarrays: (a) interlacing, (b) stacking (c) rings of different bands and polarizations, (d) orthogonally-polarized dual-band cells

1.5.2 Reflectarray Radiation Pattern

To facilitate beam steering in a reflectarray, the reflection of unit cells should be dynamically controlled. Integrating the patches with tuning elements leverages controlling the reflection phase across the panel with DC voltage commands [48–57]. Surface mount capacitors [48], solid-state varactors [49–51], solid state switches [52],

MEMS varactors [53] and MEMS switches [54] are the tuning elements that have recently been used. Especially for slotted unit cells, the tuning elements are mounted across the slot in order to tune the slot effective length and affect the reflection. The slot can be carved either out of the patch [48] or the ground plane [58].

1.6 Micro Electro Mechanical System (MEMS) Devices

Variable capacitors and switches can be fabricated by MEMS technology. The fabrication of MEMS devices is performed in clean room which is a laboratory with special environment and ventilation that is free from contamination and particles. The usual MEMS fabrication techniques are optical lithography, wet etching, sputtering, chemical vapor deposition, reactive ion etching, and electroplating [59]. These techniques are elaborated in Appendix A. The MEMS devices have a beam which is electrostatically pulled down by applying a DC voltage difference between the bottom electrode and the top beam. The micrometer range movement of the beam changes the equivalent capacitance between the beam and the bottom electrode. Cantilever beams and clamp-clamp beams are two common configurations of MEMS devices. A cantilever beam is anchored only at one end (Fig. 1.14(a)) while a clamp-clamp beam is anchored at both ends (Fig. 1.14(b)). The 3D view of a cantilever MEMS switch is depicted in Fig. 1.15. The gap and plate sizes are exaggerated in this Figure.

When actuating a MEMS device, as the voltage increases, the top beam starts to move down. As soon as the beam reaches one third the initial gap, it collapses and touches the bottom electrode. This phenomenon is called the pull-in. In order to avoid the short circuit between the beam and the electrode, the electrode is covered by an insulating dielectric layer such as Silicon Nitride or Silicon Oxide. The pull-in voltage of a specific MEMS product is its most important design parameter. Other MEMS design parameters are its up-state and down-state capacitance. For example, an efficient switch requires very low up-state capacitance which represents an open circuit and very high down-state capacitance which represents a short circuit. MEMS devices are modeled using multiphysics simulators with coupled electrostatic and mechanical forces.

The DC voltage is applied to electrodes through bias lines. For a reflectarray or a PRS where the bias lines are exposed to electromagnetic fields, the lines can not be made out of a highly conductive material such as Gold or Chromium because

they affect the field distribution over the aperture. This results in high power loss or even a very small tuned phase range. To minimize this effect, a highly resistive material such as doped PolySilicon [32,38] or Graphite paint [60] should be utilized.

This thesis investigates a custom fabrication process for hybrid or monolithic integrated MEMS-tunable reflectarray and PRS unit cell for building an orthogonally polarized independently controlled dual band aperture antenna with beam forming and beam switching ability.

Cantilever Beam

Anchor

Bottom DC
Electrode

(a)

Clamp-Clamp Beam

Anchor   Anchor

Bottom DC
Electrode

(b)
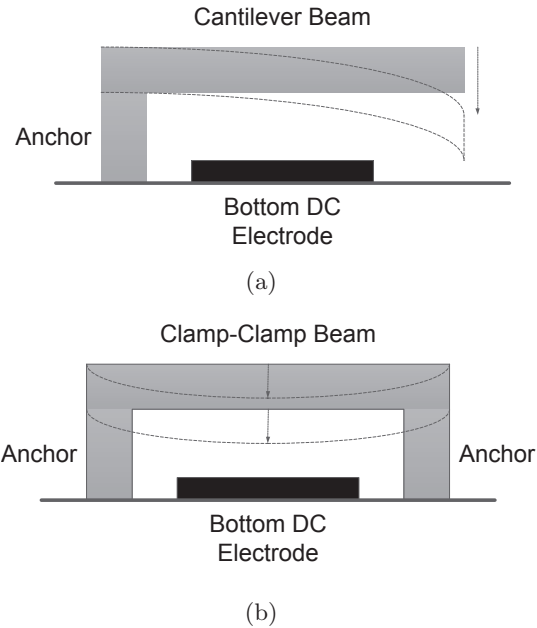
Figure 1.14. Two common configurations of MEMS devices: (a) cantilever beam, (b) clamp-clamp beam.

Switch Top Plate

Port 1   Port 2

DC   Switch Bottom
pad   Plate
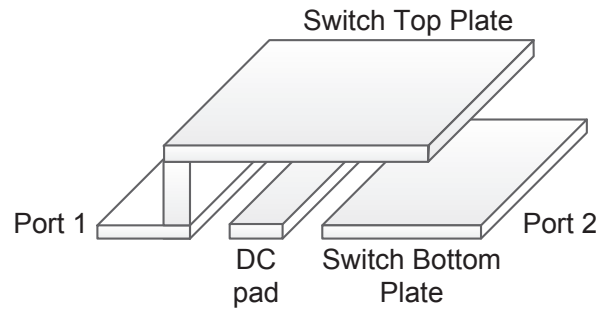
Figure 1.15. The 3D view of a cantilever MEMS switch.

1.7 Thesis Outline

This thesis investigates the potentials of two types of antennas - RCA and reflectarray - integrated with MEMS devices as platforms for future smart multi-functional aperture antennas. These antennas should be low-profile, low-cost, orthogonally-polarized independent dual-band and beam-steerable.

Chapter 2 describes the design procedure for dual-band RCA. This chapter introduces two different high gain dual broadside beam RCA designs; the first one has a dual layer dipole and the second one has a single layer slotted patch PRS. A microstrip patch antenna is also designed as the cavity feed for simultaneous reception and transmission in the upper and lower bands. This feed system is utilized in all chapters for feeding RCA.

In the first design, we offer a PRS with two single sided dipole array layers. The polarization of each band is orthogonal to the other. Because of their unique shape, dipoles are not able to operate in dual bands and polarizations. This requires two single sided dipole layers to cover for both bands. In order to make the RCA structure simpler, a dual band PRS unit cell should be designed to cover both bands with one single sided PRS layer. Besides, the unit cell has to be able to house the tuning elements for tuning and beam steering purposes.

Slotted patches can house the tuning elements across their slot. As the second design, Chapter 2 offers a slotted square patch as the PRS unit cell. This unit cell supports two orthogonally-polarized bands where the square forms one resonant frequency and the slot forms the other.

For both designs, the independence of bands was demonstrated. Also, in order to make the design procedure easier and understand the orthogonally polarized dual-band operation, a design flow-chart and an equivalent transmission line model is developed for both PRS structures.

Next, the beam steering capacity of the slotted-patch PRS was verified. In order to realize RCA with beams off broadside, a progressive phase shift has to be applied between adjacent cells across the whole PRS. In this Full Phase-Gradient PRS, the variation in slot length causes the gradient in phase across PRS. This method was applied to slotted patch PRS unit cell to realize an RCA with one horizontally polarized broadside beam and one vertically polarized beam steered up to 29° depending on the total phase variation across PRS.

Chapter 3 uses the same slotted patch cell, focusing on RCA beam shaping with two targets: realizing a tunable PRS unit cell and improving RCA beam steering capacities. For dynamic beam steering, tuning elements should be installed in PRS unit cells.

MEMS switches are hybrid integrated across the slot in the patch for tuning its phase. The MEMS switches are fabricated based on a custom process, wirebonded to the unit cell and then finally measured in a waveguide setup.

Chapter 3 inspects the inherent phase progress of the leaky wave inside the RCA cavity and proposes a novel method for beam steering. Opposed to the FPG-PRS, the phase gradient is applied only to half of PRS cells. This method is used both for beam scanning with frequency and also beam steering at fixed frequency. The Half Phase-Gradient (HPG) PRS is compared in detail with traditional FPG-PRS and shown to offer an enhanced scan profile, faster tracking, and also lower DC power consumption which are critical for wireless, space and military applications.

In order to gain a deeper understanding of the radiation phenomena in RCA with nonuniform PRS such as FPG or HPG-PRS, a radiation model is required. The current literature lacks a model that can be applied to non-uniform PRS. Chapter 3 proposes a radiation model for calculation of the radiation pattern for non-uniform apertures. To verify this model, it was applied to the novel half phase gradient structure and the calculated patterns are compared to the measurements. This model calculates the scan angle and the main-lobe beam-width within $5°$.

Finally, Chapter 3 explains the realization of a MEMS-tunable hybrid integrated PRS unit cell which is required for implementing the phase-gradient PRS. Using this cell, a beam shaping RCA is designed with an independent vertically polarized broadside beam and a horizontally polarized beam which is switched among all possible beam forms of leaky wave antenna depending on PRS configuration which is adjusted by MEMS switches and the operating frequency; i.e. a broadside beam, a symmetric conical beam, a frequency-scanned asymmetric single beam and also an asymmetric single beam which is steered at fixed frequency.

Chapter 4 studies the potentials of reflectarrays as orthogonally polarized dual band beam steering antennas. It presents a monolithic integrated MEMS-tunable low-loss double slotted patch reflective unit cell which operates at 12 GHz with vertical polarization and 14 GHz with horizontal polarization corresponding to Ku-band mobile satellite communication. The unit cells are measured inside a waveguide

setup with DC bias pads to control the MEMS switches.

Chapter 2

Dual-Band Resonant Cavity Antenna

Dual-band operation is the basic requirement for the antennas used as the multifunctional apertures. This chapter focuses on PRS designs with orthogonally polarized independent arbitrarily separated dual bands:

- The orthogonal polarization of the bands ensures their isolation.

- The arbitrary separation of the bands makes these antenna architectures compatible with a variety of applications that have their own operating bands.

- The independence of the bands allows forming two different beam shapes. This is further pursued in the following chapters.

There are several ways for realizing dual band RCA [22–25, 27, 28, 31, 61], the simplest of which is to use two periodic structures. Reference [24] offers a dual-band RCA with single layer double sided PRS. But, the bands are of the same polarization and their separation is not arbitrarily controlled since the gain enhancement occurs at odd modes of cavity transmission. In another design, the PRS is a single layer single sided slot array [28]. However, low radiation efficiency (6.7 % in the upper band) and inadequate flexibility in separation of the bands, limit its application. To our best of knowledge, the only reported dual band dual polarized antenna is reported in [23]. This design is based on double layer metamaterial structure. It lacks a methodology for arbitrary selection of bands. Similar to [28], it suffers from low radiation efficiency. Besides, each band radiates both linear polarizations which is different from the requirement of orthogonally-polarized bands.

Two PRS structures are investigated in this chapter; a dual layer dipole and a single layer slotted patch [26, 61, 62]. A complete design procedure is presented for these structures; Initially, a parametric sweep on each unit cell design parameter reveals the effect of each parameter on the frequency response of unit cell reflection. This is of critical significance since the RCA radiating aperture needs to be partially reflective at each operating band in order to ensure the generation of high gain broadside beam. Then, the RCA cavity height adjustment for dual band operation is explored. Traditionally, ray tracing method is used to calculate the cavity height which is a function of operating frequency and the reflection phase at that frequency. For a single layer PRS, operation at each band requires a different cavity height which is a paradox. This chapter proposes a method for height adjustment using different modes of operation for the bands. Finally, all these design keys are collected together in order to form an organized flow chart for quick design of a RCA with two broadside beams of different frequency and orthogonal polarization.

The above mentioned applications also have an extra requirement on independence of bands. For both of the novel single and double layer PRS structures proposed in this chapter, it is demonstrated how the two bands are independently adjusted. Also, it is shown that the separation of bands can be arbitrarily selected. This capacity allows using these RCAs in a variety of applications which have their own operating bands.

The study of orthogonally polarized dual band RCAs will be incomplete without an equivalent model. But, there has been limited studies on the operating principles, modeling and radiation phenomena of dual band RCAs. hence, this chapter presents an equivalent transmission line model with lump elements for the proposed RCAs in order to gain a better understanding of their operation.

2.1   Dual-Layer Dipole PRS

2.1.1   PRS Unit Cell Design

The proposed PRS is composed of two layers of printed dipole which should be orthogonally aligned to support independent bands. Fig. 2.1 demonstrates the top and side view of this PRS unit cell. The dipoles are printed on a TLX-8 laminate with thickness (t) of 1.52 mm, relative dielectric constant (ε_r) of 2.55 and dielectric loss tangent ($\tan \delta$) of 0.0019. The dipoles of the two layers could be of different

sizes. But each layer should be transparent to the other.

As the first design step, the amplitude and phase of the PRS infinite array reflection coefficient (Γ) should be inspected. The infinite array is simulated using periodic boundary condition around the unit cell. As an example, here, two resonant frequencies around 10 and 12 GHz are sought. To understand the cell operating principle and adopt the optimum unit cell sizes, the effect of each parameter on reflection is inspected.

(a)

(b)
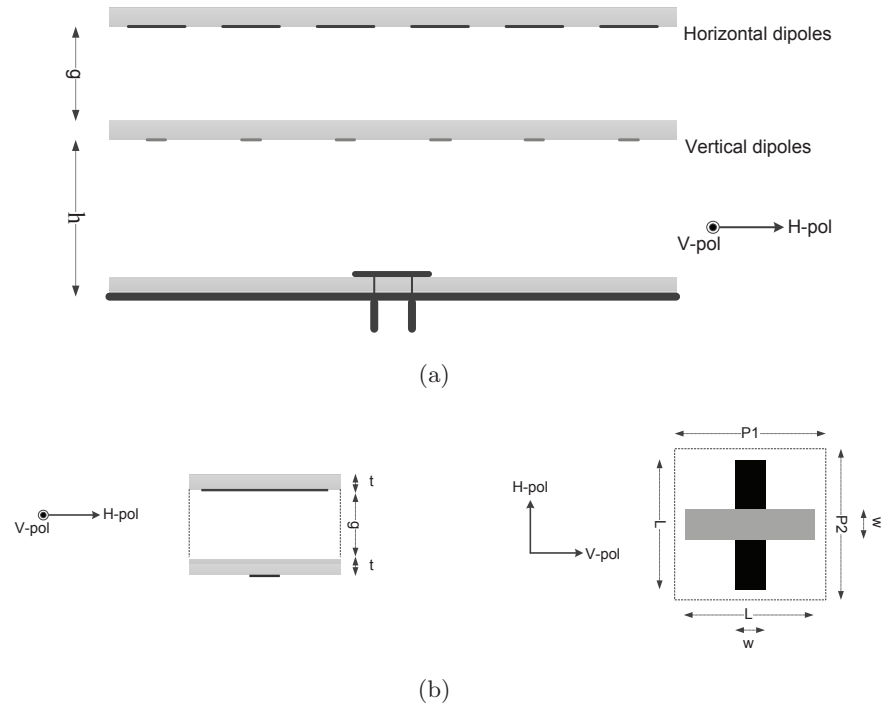
Figure 2.1. (a) Side view of the RCA with double-layer dipole array as PRS and microstrip patch antenna as the feed system; (b) Top and side view of the unit cell of the double-layer dipole PRS.

Dipole Length (L)

Fig. 2.2 shows the effect of changing L, on the reflection amplitude ($|\Gamma|$) of the double-layer dipole array. The resonant frequencies should be selected in the range where the reflection amplitude is close to unity which implies that the surface is partially reflective. Decreasing L, increases the frequency range where the proposed array is partially reflective. Thus the resonant frequencies will be higher.
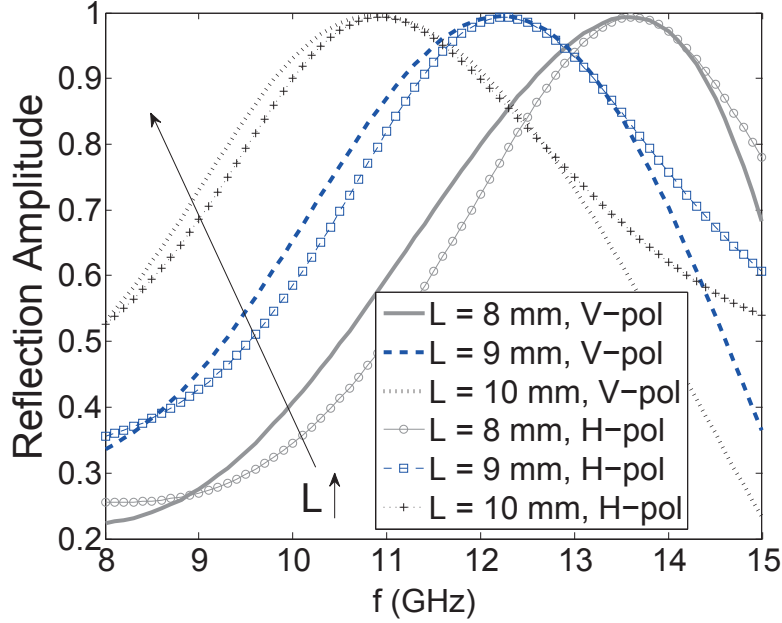
Figure 2.2. Reflection amplitude of the double-layer dipole infinite array for various values of L with V-pol and H-pol; $P = 11$, $g = 5$, $w = 1$ mm.

Dipole Width (w)

Each dipole array creates one of the resonant frequencies of the unit cell at each linear polarization. For each operating band and each polarization, one of the dipole arrays is partially reflective and the other dipole array is partially transparent. To inspect the effect of w, a unit cell consisting of a single-layer dipole is simulated (Fig. 2.3). Fig. 2.4 demonstrates the effect of changing w on the reflection amplitude of the single-layer dipole array at vertical and horizontal polarizations. It shows that if the polarization of the incident plane wave is parallel to the dipole axis, it is partially reflective and if the polarization of the incident plane wave is perpendicular to the dipole axis, it is partially transparent. Increasing w, causes the dipole structure to deviate to a patch configuration. It also increases the frequency range where the array is partially reflective. But the dual-polarization performance of the single-layer dipole unit cell is disrupted. Increasing w, deteriorates the transparency of dipole array at the polarization perpendicular to its axis. This is not a desirable phenomenon for the proposed unit cell. Hence, it is recommended to adopt $w < L/10$.
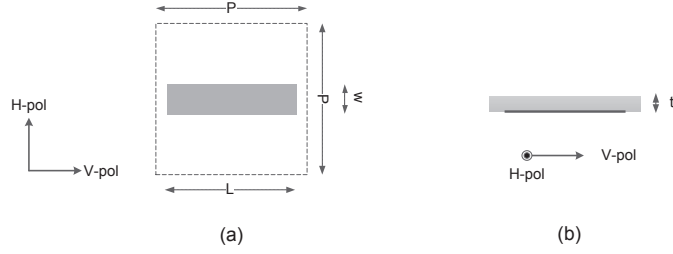
Figure 2.3. (a) Top view, (b) side view of the unit cell of the single-layer dipole array.
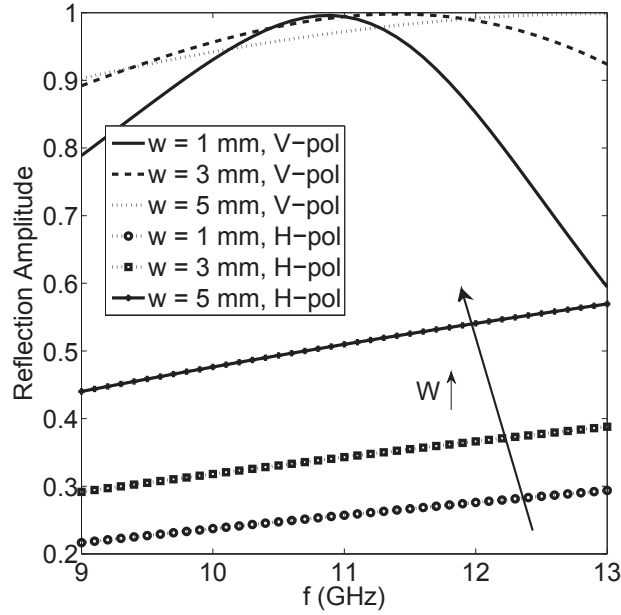
Figure 2.4. Reflection amplitude of the single-layer dipole array for various values of w with V-pol and H-pol; $P = 11$, $L = 10$ mm.

Unit Cell Periodicity (P)

Fig. 2.5 depicts the effect of changing P on the reflection amplitude of the double-layer dipole array. Controlling P changes the frequency range where the unit cell is partially reflective. A P value of 11 mm covers the $10 - 12$ GHz range. Based on array theory, it is recommended to have element spacing of less than $\lambda/2$ in order to avoid grating lobes. Same principle holds here since the dipole array elements are actually the secondary radiators of the RCA which are illuminated by the RCA feed system [2].
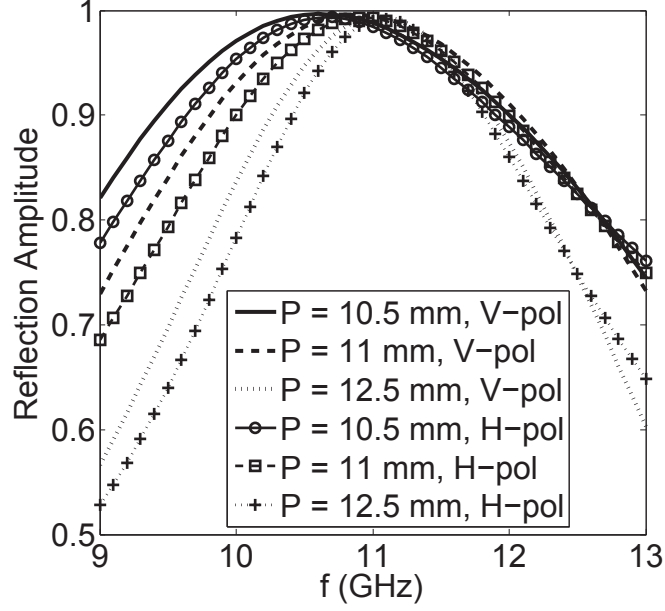
Figure 2.5. Reflection amplitude of the double-layer dipole infinite array for various values of P with V-pol and H-pol; $L = 10$, $g = 5$, $w = 1$ mm.

According to the above analysis, the following values are adopted: $P = 11$ mm, $L = 10$ mm, $w = 1$ mm. The distance between the two laminates (g), determines the separation of the resonant frequencies at each polarization. As an initial design, a g value of 5 mm is adopted. Fig. 2.6 shows the reflection amplitude and phase of infinite array of the designed double-layer PRS illuminated by normal TEM plane wave with vertical (V-pol) and horizontal (H-pol) polarizations. According to Fig. 2.6(a), if the resonant frequencies are selected within 10 and 12 GHz, the reflection amplitude remains higher than 0.9 at both vertical and horizontal polarizations.
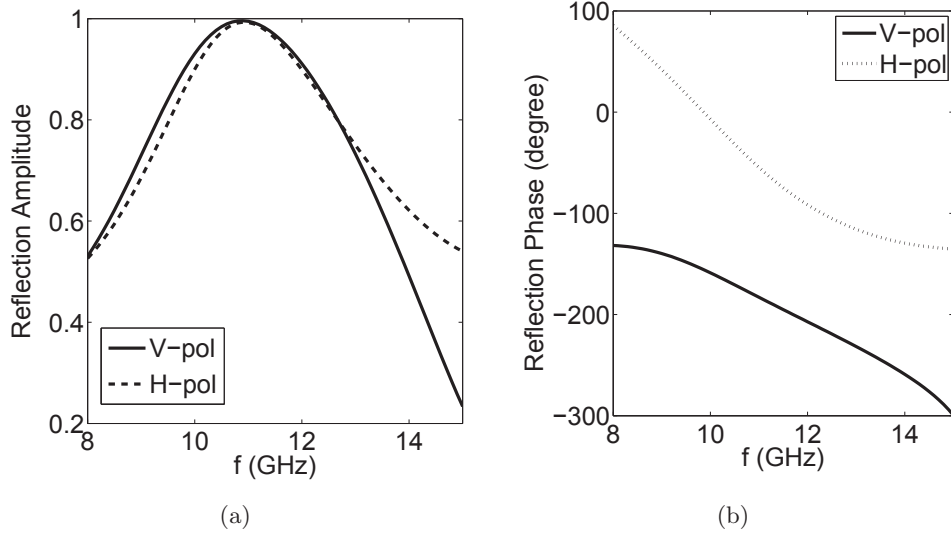
Figure 2.6. (a) Reflection amplitude, (b) reflection phase of the double-layer dipole array with V-pol and H-pol. The sizes of the dipole layers are the same: $P1 = P2 = 11$, $L = 10$, $g = 5$, $w = 1$ mm.

Using Eq. 3.18, the height of cavity is calculated. It should be emphasized that the reflection coefficient of the PRS should vary gradually with frequency around the operating frequency of the antenna in order to have a larger operating bandwidth. If the reflection coefficient phase varies rapidly with frequency, the antenna performance will be sensitive to manufacturing errors especially the cavity height (h). In order to obtain a desired frequency center for each band with prescribed separation of the bands (1.9 GHz in this example), appropriate values of N should be picked for each polarization. Fig. 2.7 depicts the height of the cavity versus frequency for both polarizations with the different combinations of N. In this Fig., h is considered from ground to the first layer of the double-layer PRS. Fig. 2.7(a) demonstrates that if the double-layer PRS is located at a height of 15.6 mm above a ground plane, the cavity resonates at 10.1 GHz with V-pol and at 12 GHz with H-pol. According to Fig. 2.7(b) and 2.7(c), for other N combinations, the cavity does not have the same height for V-pol and H-pol within the desired frequency range of $10 - 12$ GHz. Hence, a dual-band RCA is not realizable. Therefore, the design continues with N(V-pol) and N(H-pol) of 2.

24
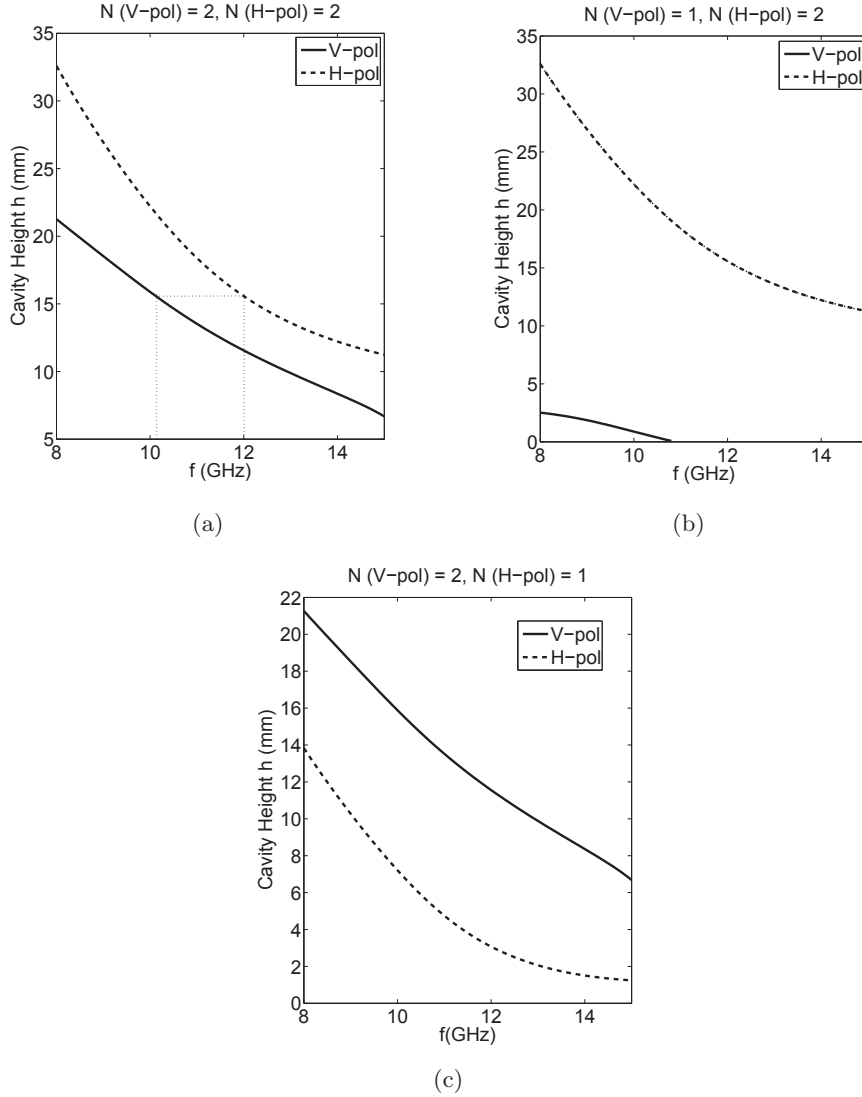
Figure 2.7. h versus frequency for V-pol and H-pol and for various combinations of the resonant mode number; (a) V-pol and H-pol have a common height at 15.6 mm. (b), (c) V-pol and H-pol do not have a common height. Thus a dual-band RCA is not realizable.

2.1.2 Transmission Line Model

The equivalent transmission line model provides a deeper understanding of RCA orthogonally-polarized dual-band operation. Initially, a single-layer infinite array of dipoles is simulated at both resonant frequencies with both polarizations of the incident wave i.e. parallel ($\parallel$) and perpendicular ($\perp$) to dipole axis. Fig. 2.8 demonstrates the transmission line model of a single-layer PRS excited by a transverse electromagnetic (TEM) plane wave with electric field vector parallel ($E_\parallel$) or perpendicular ($E_\perp$) to dipole axis. The PRS impedance is calculated from reflection

coefficient (Fig. 2.6) using :

$$Z' = \eta_0 \frac{1 + \Gamma}{1 - \Gamma} \tag{2.1}$$

where η_0 is the free space impedance (377 Ω) and Z' is the parallel combination of Z_{PRS} and η_0. Therefore, the single-layer PRS impedance is extracted as:

$$Z_{PRS} = \frac{\eta_0 Z'}{\eta_0 - Z'} \tag{2.2}$$

Table 2.1 summarizes single-layer PRS impedance for parallel($E_{inc_\parallel}$) and perpendicular ($E_{inc_\perp}$) polarization of incident waves at 10.1 and 12 GHz respectively. When the polarization of incident wave is perpendicular to dipole axis, the single-layer PRS impedance can be approximated by an equivalent resistance ($R_\perp$) of 234 Ω and capacitance of 0.024 pF. The $R_\perp$ value adopted here is the average of real part of $Z_\perp$ at the two resonant frequencies. The reflection coefficient amplitude at both resonant frequencies is around 0.26 which implies partial transparency for this incident wave. However, when the polarization of incident wave is parallel to dipole axis, the single-layer PRS array is approximated as an equivalent resistance ($R_\parallel$) which is much smaller than $R_\perp$, in series with a capacitance ($C_\parallel$) and an inductor ($L_\parallel$). These values are calculated as:

$$L_\parallel = \frac{\omega_1 X_\parallel^{(1)} - \omega_2 X_\parallel^{(2)}}{\omega_1^2 - \omega_2^2} \tag{2.3}$$

$$C_\parallel = \frac{\omega_1^2 - \omega_2^2}{(\omega_1 \omega_2)(\omega_1 X_\parallel^{(1)} - \omega_2 X_\parallel^{(2)})} \tag{2.4}$$

where ω_1 and ω_2 are the lower and upper resonant angular frequencies ($2\pi \times 10.1$ and $2\pi \times 12$ GHz) respectively and $X_\parallel^{(1)}$ and $X_\parallel^{(2)}$ are the imaginary part of Z_{PRS} at ω_1 and ω_2 respectively. The value of $C_\parallel$ and $L_\parallel$ are 0.032 pF and 6.9 nH respectively.

The double-layer dipole PRS model is based on the single-layer model. Fig. 2.9(a) shows that the front array is partially reflective and the back array is partially transparent at 10.1 GHz with vertically polarized (V-pol) incident wave. However, the situation is different at 12 GHz with horizontal polarization (H-pol) , where the front array is partially transparent while the back array is partially reflective (Fig. 2.9(b)). Hence, the transmission line model is derived for the operation of RCA at V-pol (Fig. 2.10(a)) and H-pol (Fig. 2.10(b)). In the model, the short circuit represents the ground plane which is at a distance of h ($h = l + t$) from the lower dipole array. The voltage source (V_s) is the voltage generated by the RCA feed system and R_s

26

represents the conductor losses of the microstrip patch antenna originating from metal finite conductivity (σ) and the laminate dielectric loss ($\tan \delta$). The network model includes 4 pieces of ideal transmission lines. The microstrip patch antenna laminate is modeled by a transmission line of same thickness (t) and characteristic impedance of $\frac{\eta_0}{\sqrt{\varepsilon_r}}$. The line with characteristic impedance η_0 and length g, models the air gap between the dipole arrays. The transmission line of length l and characteristic impedance η_0, models the cavity space that is formed between the RCA feed and the lower dipole array. The circuit is terminated in an infinite transmission line with characteristic impedance of η_0 that models the free space above the RCA. This transmission line can be replaced by a lumped resistance of value η_0. The equivalent lumped elements are summarized in Table 2.2. The lumped elements are the same for both frequencies except $R_{\parallel}$ which represents the dipole array and PRS dielectric laminate loss and depends on frequency (Fig. 2.11).
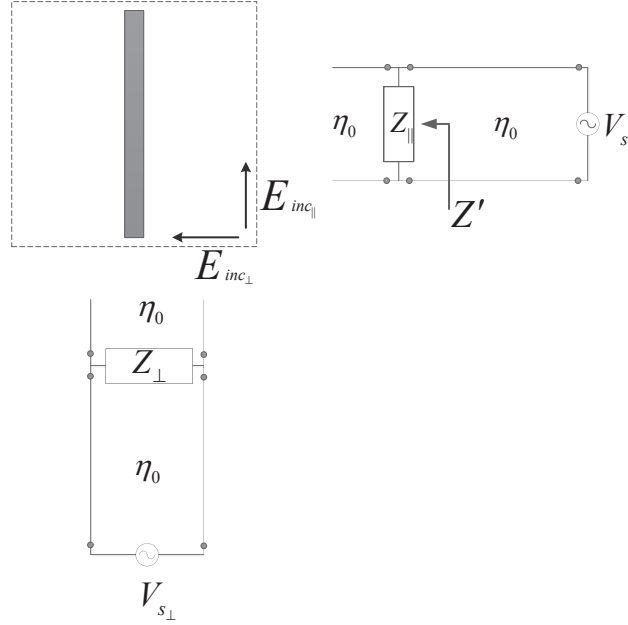
Figure 2.8. Transmission line model of the single-layer dipole array illuminated by a TEM wave normal to the surface with polarization parallel or perpendicular to the dipole axis.

$|\Gamma_\perp| \cong 0.26$ $|\Gamma_\parallel| \cong 0.9$

V-pol

E_{inc}

H-pol

k

(a)

$|\Gamma_\parallel| \cong 0.9$ $|\Gamma_\perp| \cong 0.26$

V-pol

E_{inc}

k

H-pol

(b)
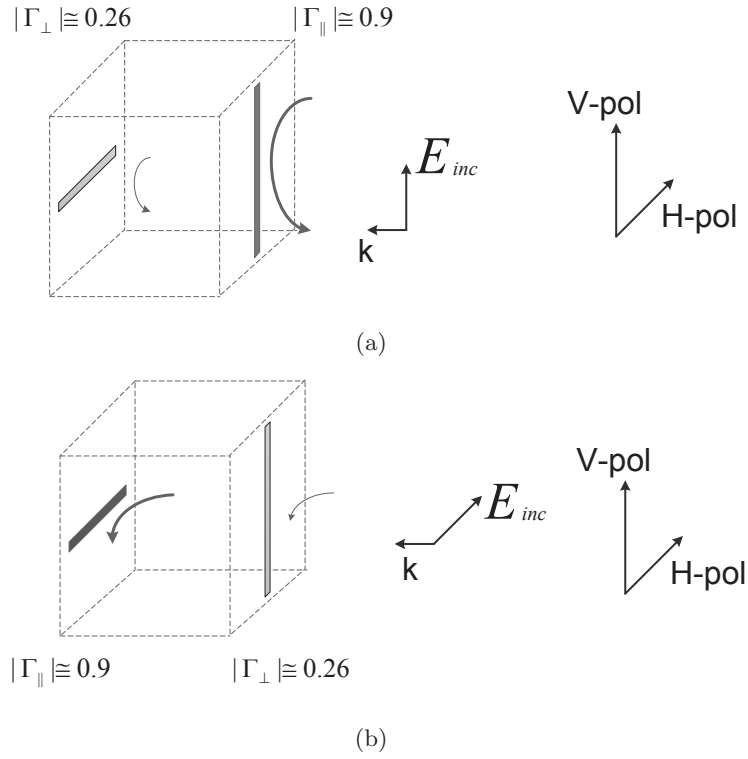
Figure 2.9. (a) When the incident wave is vertically polarized, the front array is partially reflective (dark) and the back array is partially transparent (bright gray). (b) When the incident wave is horizontally polarized, the front array is partially transparent and the back array is partially reflective.

f (GHz)	$Z_\parallel$ (Ω)	$Z_\perp$ (Ω)
10.1	$2.5 - j59.2$	$242.2 - j662.6$
12	$5.7 + j102.2$	$225.8 - j536.3$

Table 2.1. Equivalent impedance of the single-layer dipole array illuminated by a TEM wave normal to the surface.

$R_\perp$	$C_\perp$	$R_\parallel^{(1)}$	$R_\parallel^{(2)}$	$C_\parallel$	$L_\parallel$
234 (Ω)	0.024 (pF)	2.5 (Ω)	5.7 (Ω)	0.032 (pF)	6.9 (nH)

Table 2.2. Equivalent lump elements of the single-layer dipole array for the two polarizations of the incident wave.

(a)

(b)
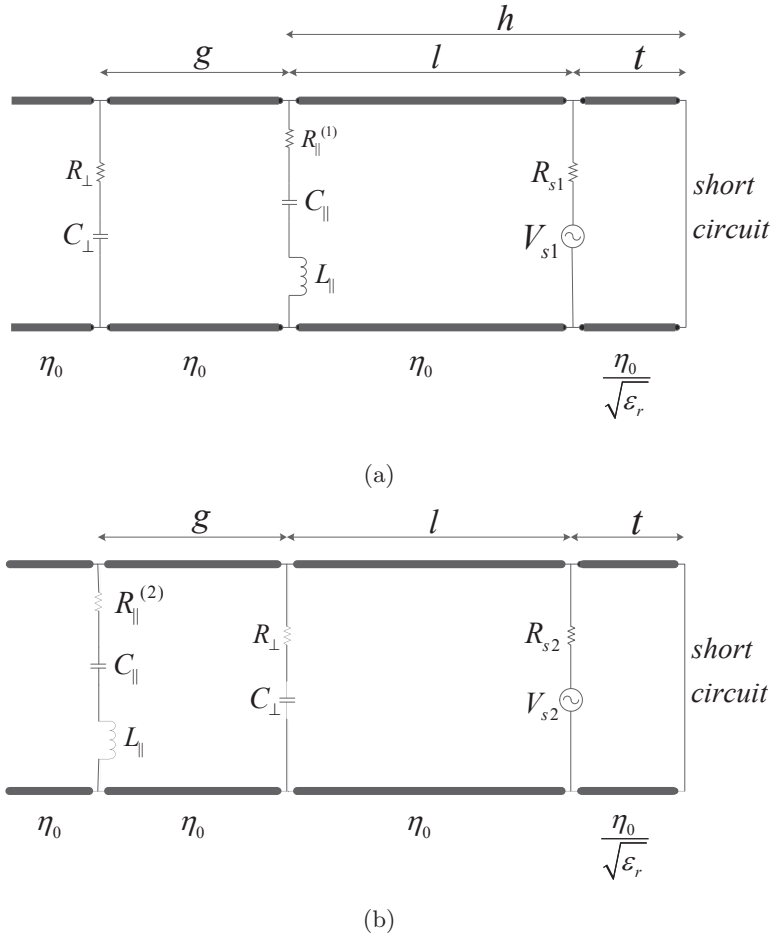
Figure 2.10. Equivalent transmission line model of the dual-band dual-polarized RCA (a) for the lower band (f = 10.1 GHz) with V-pol (b) for the upper band (f = 12 GHz) with H-pol. The length of the transmission lines is marked on the top and the characteristic impedance is marked in the bottom of the line.
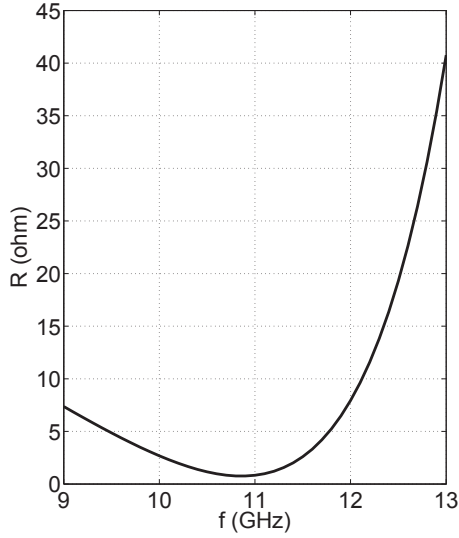
Figure 2.11. Equivalent resistance of the single-layer dipole array illuminated by a plane wave normal to the surface polarized parallel to the dipole axis.

2.1.3 Design Algorithm

A procedure is offered here in the form of a flow-chart to design an RCA with a double-layer printed-dipole-array PRS (Fig. 2.12). All the dimensions of the RCA are designed and accordingly optimized in different stages. RCA design flow-chart is divided into two parts: unit cell design and feed system design. The inputs of this algorithm are: the lower band resonant frequency f_1, the upper band resonant frequency f_2, and the properties of the commercial dielectric laminate: thickness (t), relative dielectric constant (ε_r), and dielectric loss tangent $(\tan \delta)$. In this flow-chart, index 1 and 2 refer to the lower and upper band design parameters respectively. Also, Γ, $|\Gamma|$ and φ represent the complex reflection coefficient, the reflection coefficient amplitude and the reflection coefficient phase of the infinite array illuminated by TEM plane wave normal to the surface.

The first part of the flow-chart designs the unit cell. An initial value is selected for P $(P < \frac{\lambda_2}{2})$. In the first loop, P, L, and w are tuned to get the partial reflective response over the lower operating band $(|\Gamma| > 0.8)$ for single-layer dipole unit cell. Then, an initial value is selected for g $(g \cong \lambda/6)$, in order to start simulating and optimizing the double-layer dipole unit cell. The reflection coefficient phase and amplitude at vertical and horizontal polarizations are used to draw h (Fig. 2.1.4), versus frequency for each polarization. In the second loop, different combinations

of the resonant mode numbers (N_1 and N_2) for the two polarizations are selected to find the appropriate common resonant height (h) for the two polarizations. In this part, it is recommended to adopt the h value of more than $\lambda_1/4$. Otherwise, the loading effect of the PRS on the RCA feed system (dual-band dual-polarized microstrip patch antenna), makes it difficult to tune the impedance bandwidth of the patch (frequencies where RCAs feed reflection coefficients is below -10 dB) to align with the frequencies of the PRS directivity enhancement. In the third loop, g is varied to get the desired separation between the resonant frequencies.

The dual-layer dipole PRS leverages the arbitrary separation between the two resonant frequencies which is adjusted by the gap between the layers (g). In RCA1, the band separation is 1.9 GHz. To demonstrate the flexibility of design, two other RCA's are designed with the separation between resonance frequencies of 0.7 GHz (RCA2) and 8.9 GHz (RCA3). RCA2 unit cell sizes are the same as the main design (RCA1) except $g = 10$ mm. But in RCA3, the dipoles of lower and upper layer are of different sizes. The unit cell parameters of RCA3 are as follows: in the lower layer $P1 = 5.5$, $P2 = 11$, $L = 6$, and $w = 0.5$ mm and in the upper layer $P1 = P2 = 11$, $L = 10$, and $w = 1$ mm with $g = 3$ mm. Fig. 2.13 shows the cavity height graph versus frequency for RCA2 and 3. Table 2.3 summarizes the design parameters and radiation performance of RCA1, 2 and 3 such as their maximum Directivity (D) and first Side Lobe Level (SLL).

After finding g and h, the RCA feed system is designed separately. The loading effect of PRS on the feed system, usually reduces the feed system resonant frequencies. Hence, the feed system is suggested to be initially designed to operate about 2% above the desired frequency band at each polarization.
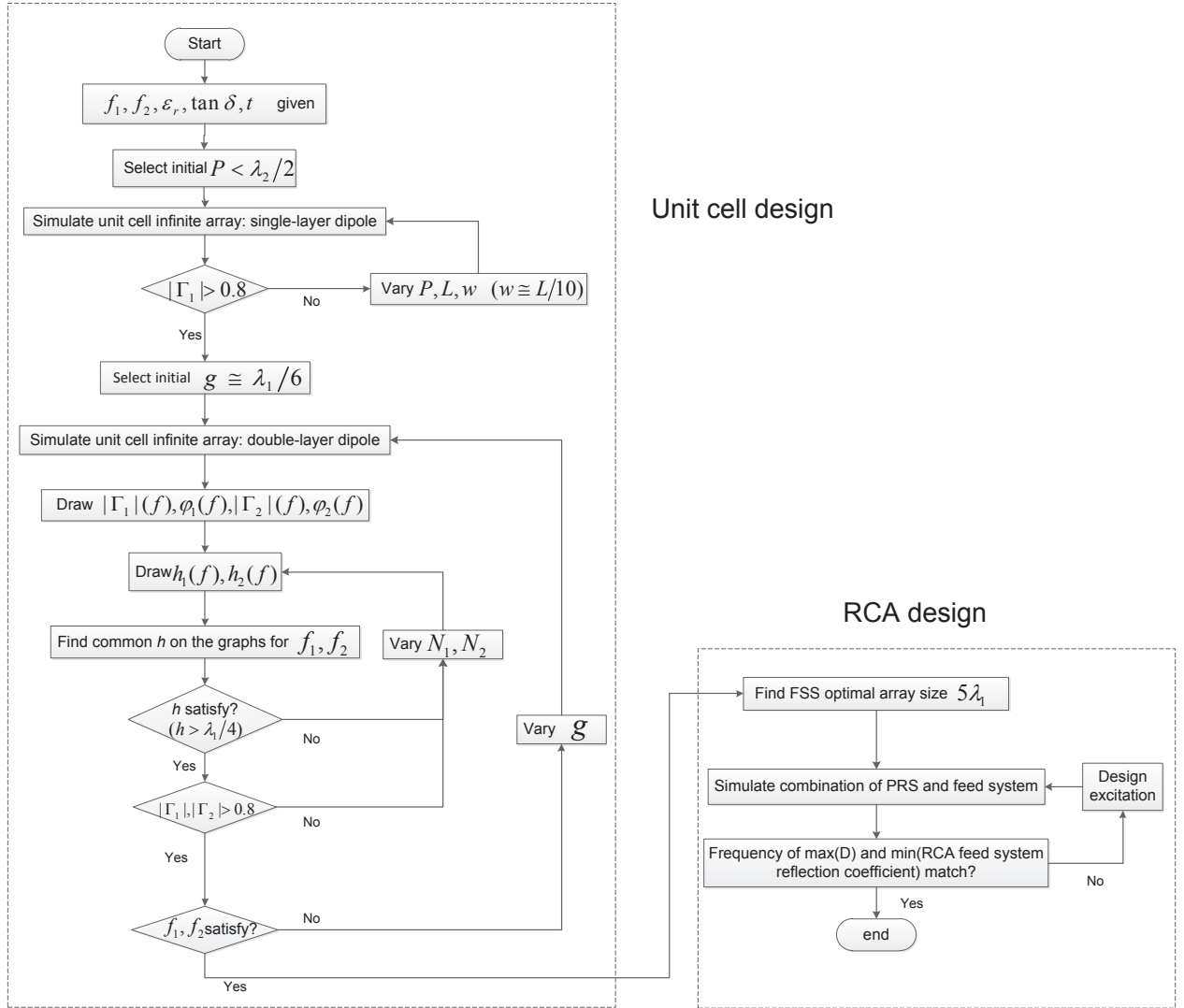
Figure 2.12. Design flow-chart for high-gain RCA with dual-layer dipole PRS.

RCA	g (mm)	h (mm)	pol	N	f (GHz)	D (dBi)	SLL (dB)
1	5	15.6	V	2	10.1	21	17.5
			H	2	12	19	15.3
2	10	15.8	V	2	10	22.5	19.5
			H	2	10.7	15.9	7.8
3	3	7.1	V	2	20	17.9	12.5
			H	2	11.1	17	11.3

Table 2.3. Comparison of RCA1, 2 and 3 with different values of g
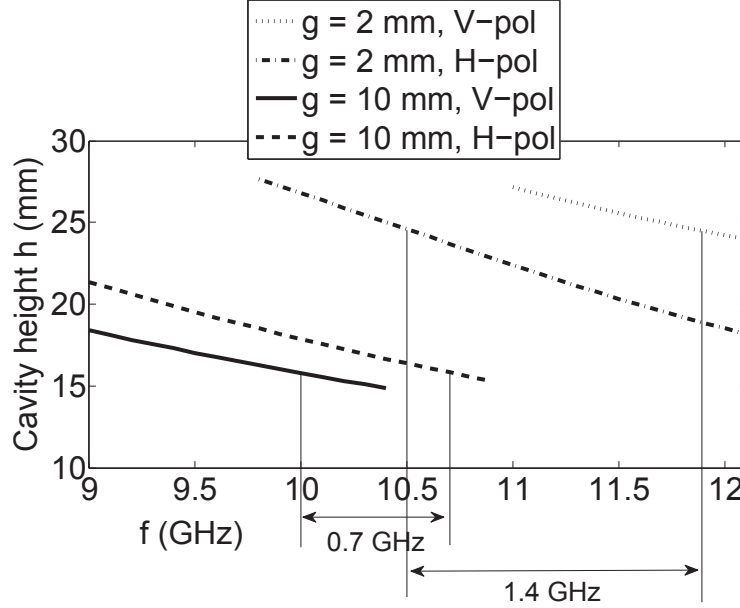
Figure 2.13. Cavity height for various values of g. Changing g results in change of resonant frequency separation.

2.1.4   RCA Simulation and Measurement

Feed system

A dual feed microstrip patch antenna plays the role of RCA1 feed system to generate two bands of orthogonal polarization (Fig. 2.14). The microstrip transmission lines are connected to two coaxial SMA connectors. The microstrip patch antenna provides a gain of 6 and 6.27 dB at the lower and the upper bands with V-pol and H-pol respectively. The simulated and measured S-parameters of the patch antenna for both ports are demonstrated in Fig. 2.15. An excellent agreement between the simulation and measurement is obtained. The isolation between the two ports is shown in Fig. 2.16. It is demonstrated that better than -22 dB of isolation is obtained at both bands.
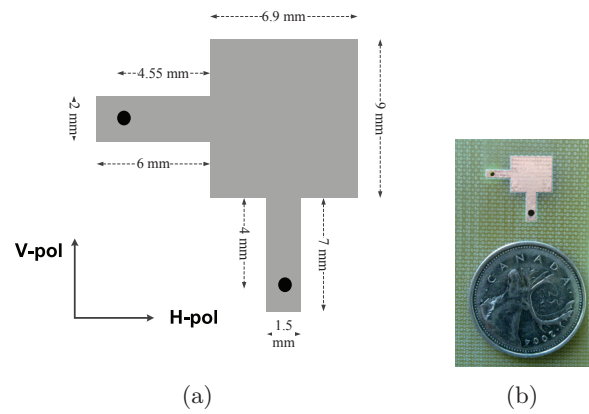
Figure 2.14. Dual-band microstrip patch antenna fed by two SMA connectors; (a) sizes (b) fabricated prototype.
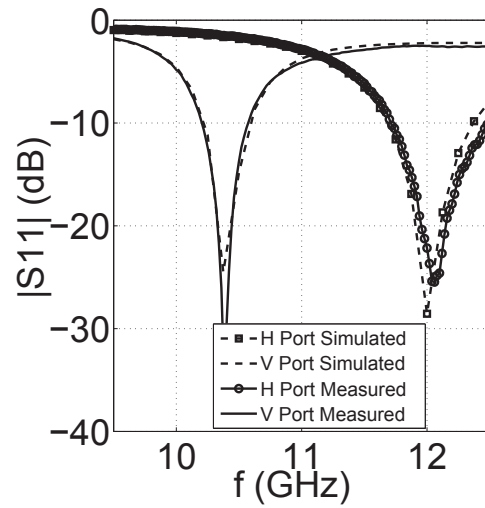
Figure 2.15. Reflection coefficient amplitude for the two ports of the dual-band dual-polarized microstrip patch antenna.
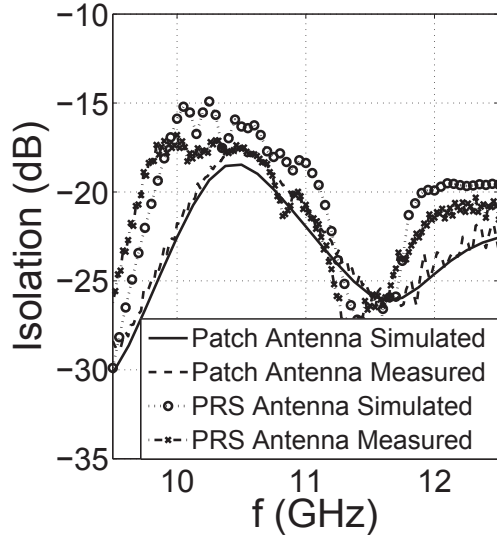
Figure 2.16. Simulated and measured port isolation of the individual microstrip patch antenna and RCA1.

RCA

The double-layer PRS is mounted over the feed system to form RCA1 as shown in Fig. 2.1(b). The size of the PRS is 154×154 mm. Fig. 2.17 shows the assembled and exploded views of the fabricated RCA. The RCA simulated and measured reflection coefficient corresponding to vertical and horizontal ports are shown in Fig. 2.18. A very good agreement is obtained between simulation and measurements. As expected, the loading effect of PRS on the microstrip patch antenna reduces the expected RCA resonant frequencies. Fig. 2.16 demonstrates the isolation between the two ports of RCA1 which is better than 17.5 dB. So, the transmission and reception bands could be assumed fairly isolated. Fig. 2.19 shows the radiation patterns of the antenna (E and H plane) at 10 GHz which is corresponding to the V-pol. The measured gain is as high as 19.6 dBi with the cross-polarization better than -27 dB. The first side-lobe level is better than 17 dB. Fig. 2.20 shows the E and H plane radiation patterns of the antenna at 11.6 GHz with H-pol. The measured gain is as high as 18 dBi with the cross-polarization better than -30 dB. The first side-lobe level is around 15 dB. The PRS has improved the gain of the microstrip patch antenna (RCA feed system) by 13.4 and 11.7 dB at the lower and the upper band respectively. The lower and the upper band have measured $3dB$ gain bandwidths of 3 and 2.56 % respectively (Fig. 2.21).

Comparing unit cell simulation results (PRS1) with the final RCA1 measure-

ment, it is observed that the maximum gain is obtained at 0.3 and 0.1 GHz below the desired frequency at the upper and the lower bands respectively. That is attributed to the assembly error and slight bow that was observed on the dielectric laminate. Besides, the RCA design process starts with PRS simulation which is excited by a normal TEM plane wave. But in the RCA, the PRS is excited by the field generated by a microstrip patch antenna.
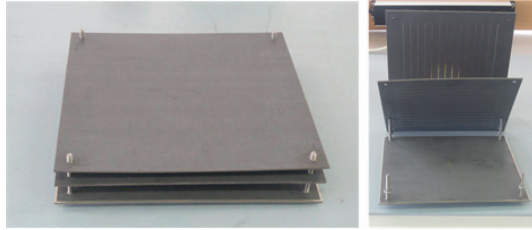
Figure 2.17. Assembled RCA and its exploded view.
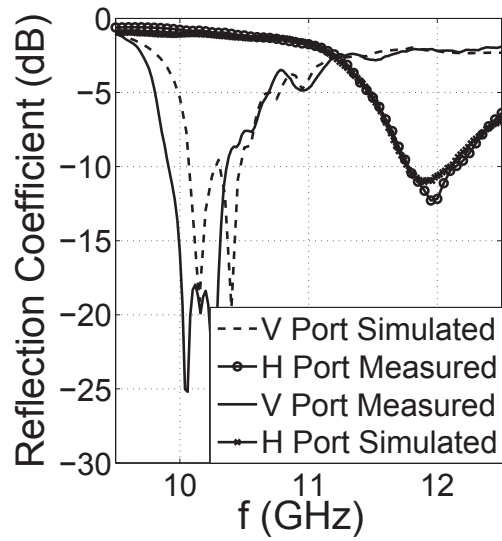
Figure 2.18. Simulated and measured reflection coefficient amplitude of RCA1 for the two ports.
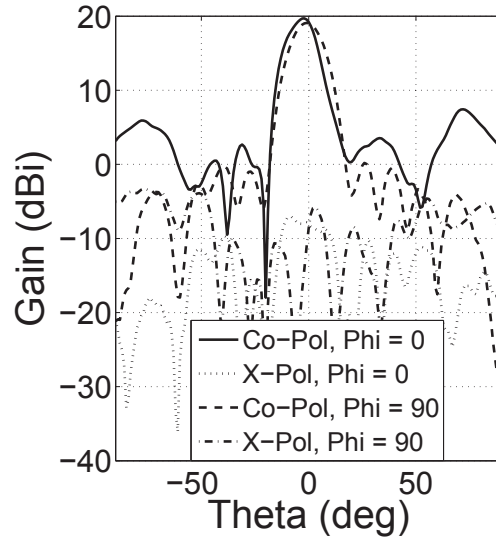
Figure 2.19. Measured co-polar and cross-polar gain of RCA1 for the lower band at 10 GHz with V-pol.
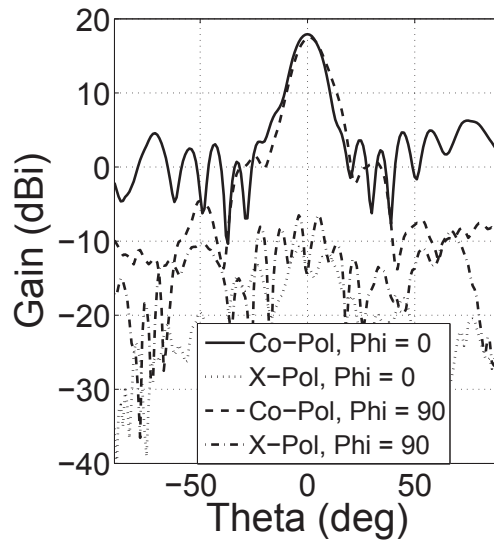
Figure 2.20. Measured co-polar and cross-polar gain of RCA1 for the upper band at 11.6 GHz with H-pol.
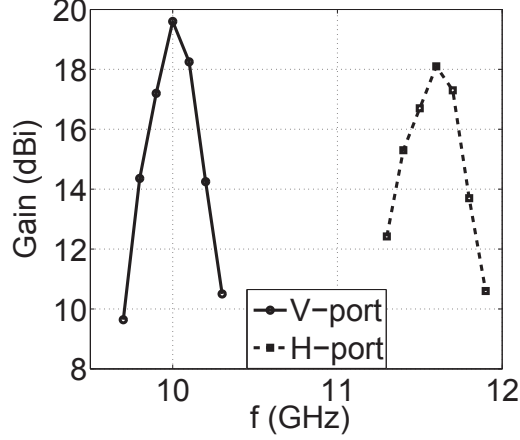
Figure 2.21. Measured gain of RCA1 vs. frequency.

2.2 Slotted Patch PRS

In this section, a dual-broadside-beam RCA is designed, fabricated and measured based on the slotted patch PRS. Also, single-beam-steering is demonstrated using Full Phase-Gradient method.

2.2.1 PRS Unit Cell Design

The proposed PRS unit cell is a single-sided printed slotted square patch shown in Fig. 2.22. The advantage of this unit cell is the supporting of two bands at orthogonal polarizations and also the capability of arbitrary and independent control of the bands. The PRS is printed on a TLX-8 laminate with thickness of 1.52 mm, relative dielectric constant (ϵ_r) of 2.55 and dielectric loss tangent ($\tan \delta$) of 0.0019. First, the effects of patch and slot size on the reflection of a plane wave normally incident upon PRS is studied and then the unit cell parameters are found for the arbitrary operation at F1(V-pol) = 10.3 and F2(H-pol) = 11.3 GHz. In order to inspect the effect of unit cell periodicity (P) and patch length (L), a patch without slot is simulated.
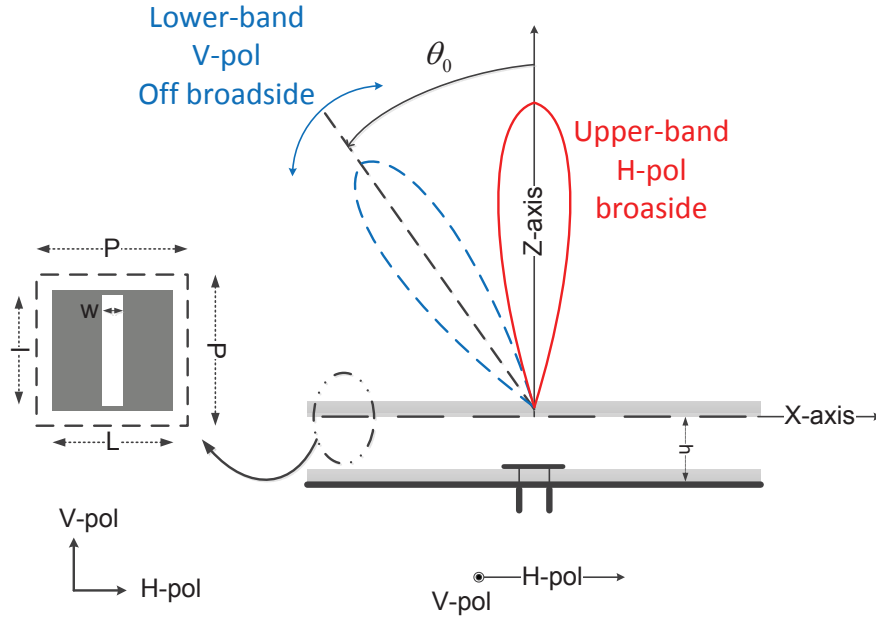
Figure 2.22. Top view of the unit cell of single-layer slotted-patch array; Side view of the RCA excited by the double probe-fed microstrip patch antenna.

Unit Cell Periodicity (P)

Fig. 2.23 shows the effect of changing P on the reflection amplitude of the patch array at H-pol. The resonant frequency should be selected in the range where the reflection amplitude is close to unity which implies that the surface is partially reflective at this polarization. Decreasing P, increases the reflection coefficient amplitude. With a P value of 11 mm, the patch array is partially reflective at 11.3 GHz.

Patch Length (L)

Fig. 2.23 shows the effect of changing L, on the reflection amplitude of the patch (without slot) array. Increasing L, increases the partial reflection. Thus, L values closer to P are more desired since higher reflection amplitude is obtained.

Slot Length (l)

The slot creates the resonant frequency at vertical polarization (V-pol) which is perpendicular to slot axis. Fig. 2.24 shows that increasing l, decreases the slot resonant frequency at V-pol. The slot resonant frequency is defined here as the frequency of PRS total reflection.

Slot Width (w)

To increase RCA gain band-width, the PRS reflection phase should vary gradually with frequency [63]. Otherwise, the gain response will be sensitive to manufacturing errors especially in cavity height (h). Fig. 2.25 shows that increasing w, increases H-pol reflection phase slope (the polarization parallel to slot axis) and consequently decreases H-pol bandwidth. Hence, it is necessary to select w values which are much smaller than L.
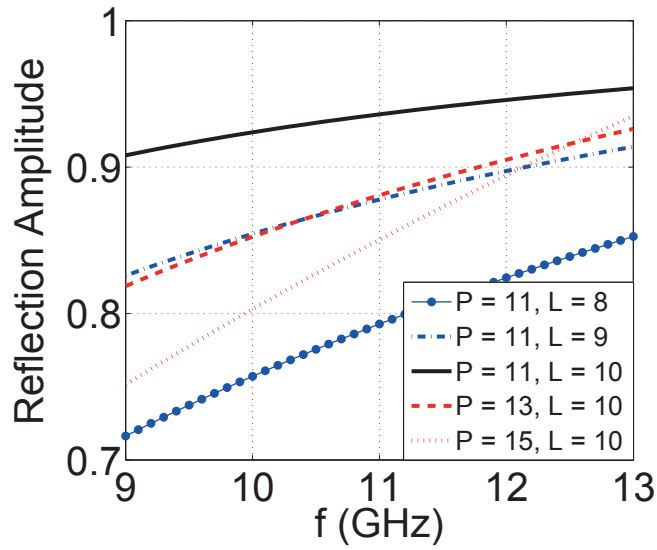
Figure 2.23. Reflection amplitude of the patch (without slot) infinite array for various values of P with H-pol; L = 10 mm.
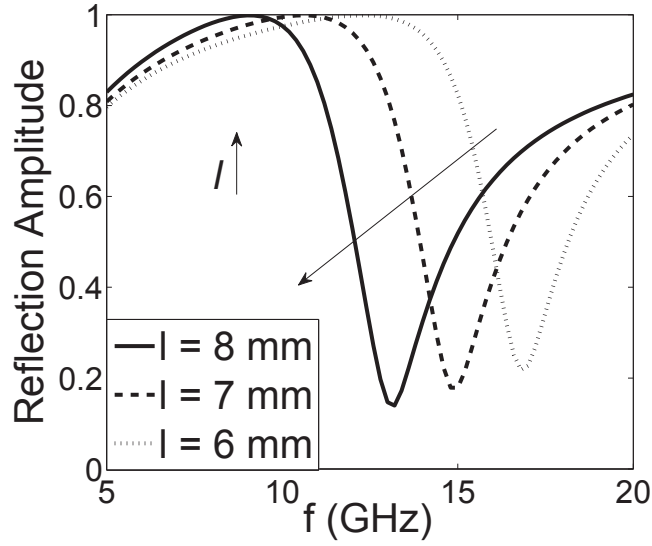
Figure 2.24. Reflection amplitude of the slotted-patch infinite array for various values of l at V-pol, for P = 11, L = 10, w = 1 mm.
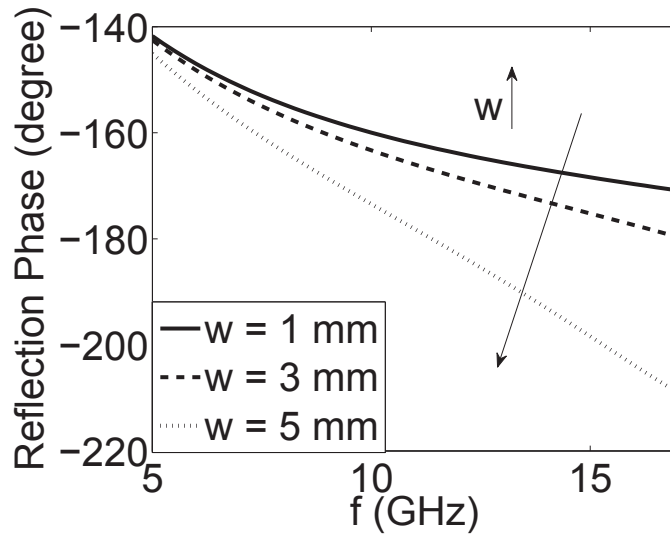
Figure 2.25. Reflection phase of the slotted-patch array for various values of w with H-pol for P = 11, L = 10, l = 8 mm.

The RCA high gain is due to the partial reflection (reflection amplitude higher than 0.7) of its top surface [17]. Based on the above analysis, the square patch sizes are set to $P = 11$ mm and $L = 10$ mm for F2(H-pol) = 11.3 GHz and the slot sizes are set to $l = 8$ mm, and $w = 1$ mm for F1(V-pol) = 10.3 GHz. The unit cell reflection at both polarizations is depicted in Fig. 2.26(a) and 2.26(b).
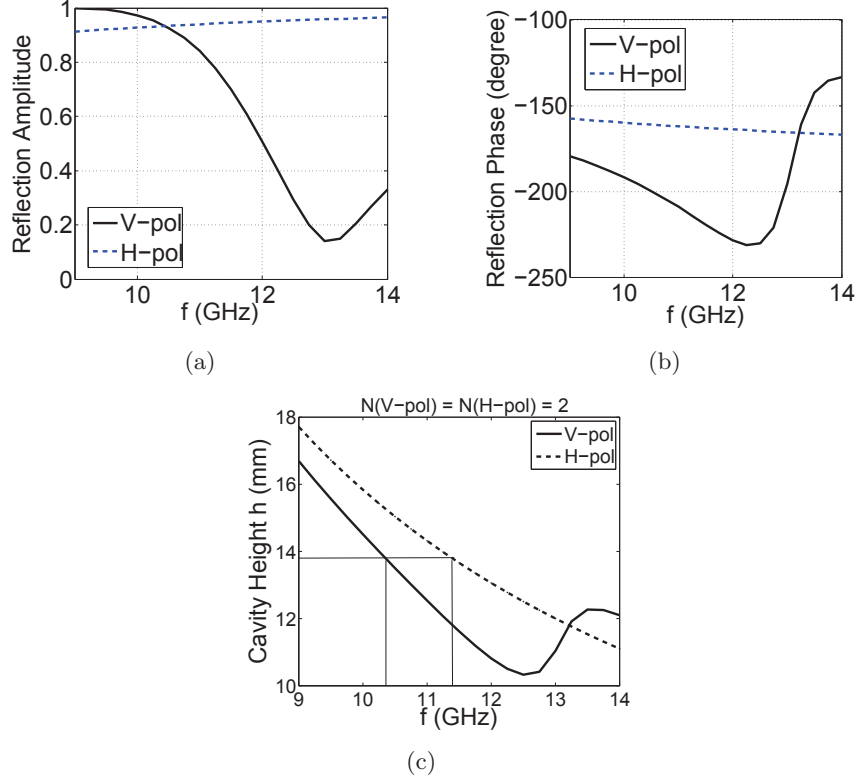
Figure 2.26. (a) Reflection Phase; (b) amplitude of slotted patch unit cell. (c) Adjustment of cavity height.

2.2.2 RCA Design

From (Eq. 3.18), in order to obtain a desired frequency center for each band with prescribed band separation (1 GHz here), one needs to select the right N for each polarization. For $h = 13.8$ mm, the cavity resonates at F1(V-pol) = 10.35 GHz and F2(H-pol) = 11.3 GHz for N(V-pol) = N(H-pol) = 2 (Fig. 2.26(c)). But for other N combinations, the cavity does not have the same height for V-pol and H-pol with the desired frequency range and hence, a dual-band RCA is not realizable.

2.2.3 Transmission Line Model

The equivalent transmission line model of RCA is investigated in this Chapter to gain a deeper insight into the operation of the proposed PRS structure. Initially, an infinite array of patches with and without slot is simulated at both operating frequency/polarizations. The PRS impedance is calculated from Eq. 2.1 and 2.2 and summarized in Table 2.4. The structure of patch without the slot is symmetric and relatively wide-band. Therefore, it has the same impedance at both polarizations

f (GHz)	pol	$Z_{slottedpatch}$ (Ω)	Z_{patch} (Ω)
10.35	V	$5.7 + j102.2$	$2.46 - j59.3$
11.39	H	$2.43 - j59.9$	$2.43 - j59.4$

Table 2.4. Equivalent impedance of the single-layer slotted-patch array illuminated by a TEM wave normal to the surface.

and frequencies. It is observed that the slot is transparent at the polarization parallel to its axis (H-pol). When the polarization of incident wave is parallel to slot axis, the PRS impedance can be approximated by an equivalent resistance ($R_{\parallel}$) of 2.46 Ω in series with a capacitance (C_{patch}) of 0.23 pF. However, when the polarization of the incident wave is perpendicular to slot axis, the PRS array is equivalent to a resistance ($R_{\perp}$) of 5.7 Ω in series with an inductor (L_{slot}) of 1.5 nH.

Hence, the following transmission line model is derived for the operation of RCA at V-pol and H-pol (Fig. 2.27). For modeling V-pol and H-pol operation, the switch should be in the left and right position respectively. In this Fig., the short circuit represents the ground plane which is at a distance of h ($h = d + t$) from the PRS. t is the thickness of the laminate used for the realization of microstrip antenna as the feed system. The voltage source (V_s) is the voltage generated by the RCA feed system and R_s represents the conductor losses of the microstrip patch antenna originating from metal finite conductivity (σ) and the laminate dielectric loss ($\tan \delta$). The network model includes 3 pieces of ideal transmission lines. The microstrip patch antenna laminate is modeled by a transmission line of same length (t) and characteristic impedance $\frac{\eta_0}{\sqrt{\varepsilon_r}}$. The transmission line of length d and characteristic impedance η_0, models the cavity space that is formed between the RCA feed and the PRS. The circuit is terminated in an infinite transmission line with characteristic impedance of η_0 that models the free space above the RCA. This transmission line can be replaced by a lumped resistor of same value. The equivalent lumped element values are summarized in Table 2.5.

R_{patch}	C_{patch}	R_{slot}	L_{slot}
2.45 (Ω)	0.23 (pF)	5.7 (Ω)	1.5(nH)

Table 2.5. The equivalent lump elements of the single-layer slotted-patch array for the two polarizations of the incident wave.
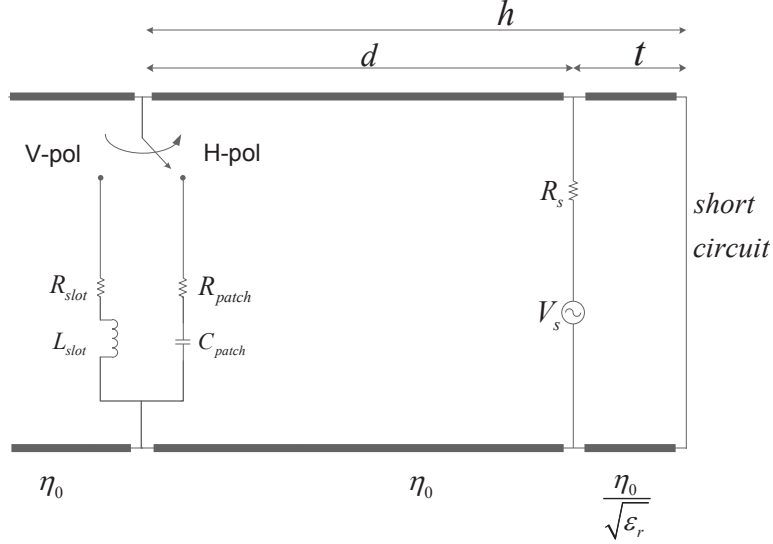
Figure 2.27. Equivalent transmission line model of the dual-band dual-polarized RCA at V-pol with f = 10.35 GHz and at H-pol with f = 11.39 GHz. The length of the transmission lines is marked on the top and the characteristic impedance is marked at the bottom of the line.

2.2.4   Design Algorithm

A design algorithm is presented here in this chapter, in the form of a flow-chart (Fig. 2.28) to design an RCA with a slotted-patch PRS to support dual bands of orthogonal polarization. The flow-chart finds unit cell sizes and cavity height and then optimizes them. The flow-chart is divided into two parts: unit cell and the feed system. The inputs of this algorithm are: the lower and upper band resonant frequency (index 1 points to the lower band and index 2 points to the upper band), the properties of the commercial dielectric laminates (thickness t, relative dielectric constant ε_r, and dielectric loss tangent ($\tan \delta$)). In the chart, Γ, $|\Gamma|$ and ϕ represent the reflection coefficient, the reflection coefficient amplitude and the reflection coefficient phase of the infinite array illuminated by TEM plane wave normal to the surface.
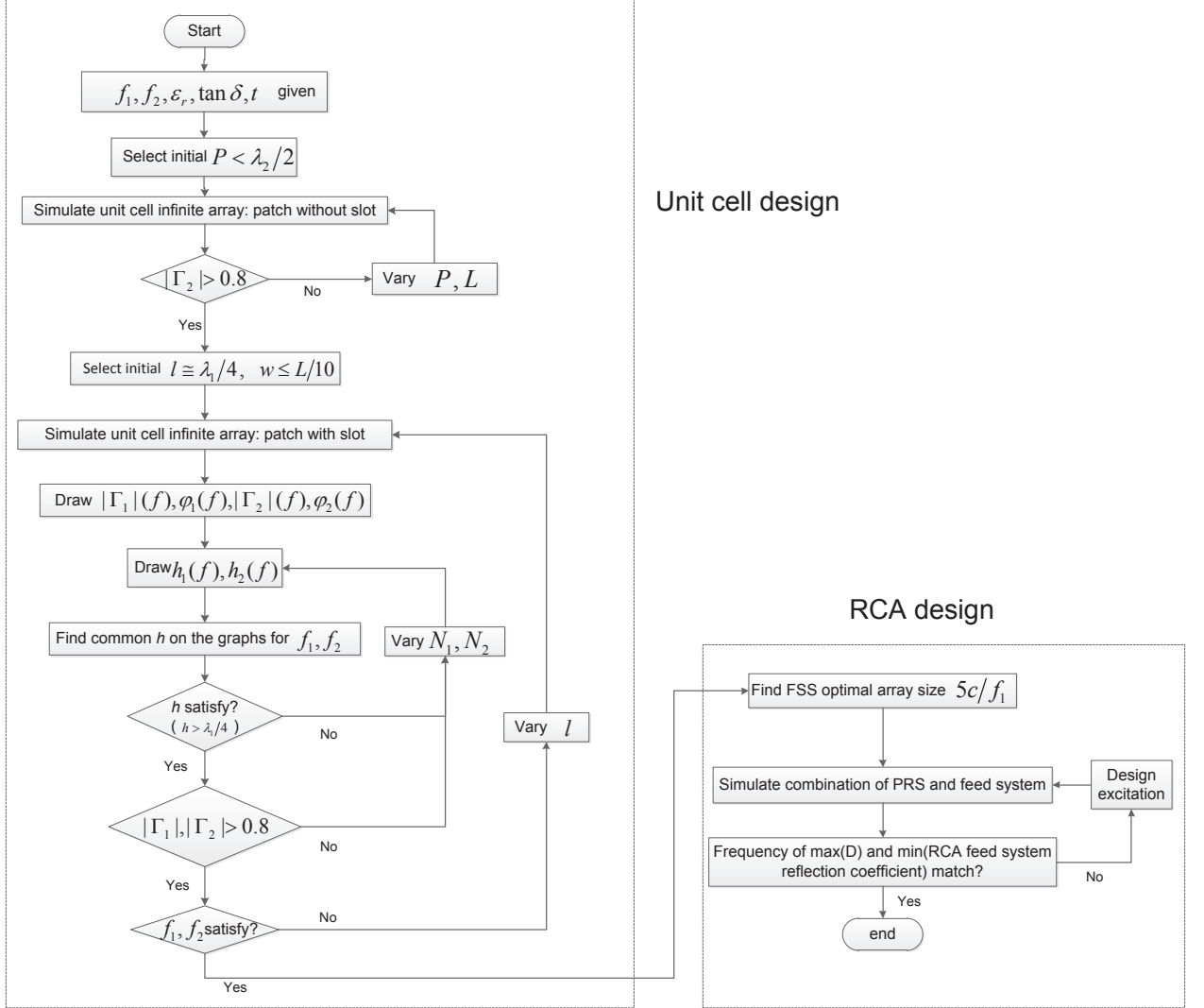
Figure 2.28. Design flow-chart for RCA with slotted-patch PRS.

In the algorithm, an initial value is selected for P ($P < \frac{\lambda_2}{2}$). In a loop, P and L are tuned to get the partial reflective response over the upper operating band ($|\Gamma_2| > 0.8$) for a patch unit cell without slot. Then, an initial value is selected for l ($l \cong \frac{\lambda_1}{4}$) and w ($w < \frac{L}{10}$) in order to start simulation and optimization of the slotted-patch cell. The reflection coefficient phase and amplitude response at vertical and horizontal polarizations are used to draw h versus frequency for each polarization. Then, different combinations of the resonant mode numbers (N_1 and N_2) for the two polarizations are evaluated to find the appropriate common resonant height for the two polarizations. It is recommended to use $h > \frac{\lambda_1}{4}$. Otherwise, the loading effect of the PRS on the feed system, makes it difficult to tune the impedance bandwidth

45

of the patch to be aligned with the frequencies of the PRS directivity enhancement. If the same height for the two bands are found, the algorithm proceeds to RCA Design part, Otherwise, by changing l, a common height is sought for the desired frequency bands.

The algorithm for feed system design is the same as explained in Figure 2.12.

2.2.5 RCA Implementation

Following the unit cell design, a dual-broadside-beam RCA is designed, fabricated and measured. In order to have broadside beams, uniform PRS is used. In this design, the total PRS size is $5\lambda \times 5\lambda$ at the lower band. Increasing the size beyond 5λ does not cause considerable gain improvement [24]. The first step is to design a feed system for the proposed RCA.

RCA feed

A microstrip patch antenna plays the role of RCA feed system to generate orthogonally-polarized dual-band radiation. The patch is fed by two microstrip transmission lines. The lines are connected to two coaxial SMA connectors at the back of the ground plane. The microstrip patch antenna provides a gain of about 5 dBi at both bands. Both ports are matched and the port isolation is better than 15 dB.

RCA

The fabricated RCA and the simulated and measured S-parameters are shown in Fig. 2.29 and 2.30 respectively. Fig. 2.31(a) shows the lower-band main-plane radiation pattern of the antenna at 10.25 GHz which is corresponding to the V-port. The measured gain is 18.06 dBi with cross-polarization of 26 dB. Fig. 2.31(b) also shows the upper-band main-plane radiation pattern of the antenna at 11.05 GHz with H-port. The measured gain is 19.41 dBi with the cross-polarization better than 31 dB. The PRS has significantly improved the gain of RCA feed system. The antenna co-polar and cross-polar gain against frequency is demonstrated in Fig. 2.31(c). The 3dB gain bandwidth is about 2.9 and 2.7 % at the lower and upper bands (Fig. 2.31(d)). Comparing unit cell simulation results with those of RCA measurement, it is observed that the maximum gain is obtained at 0.25 and 0.05 GHz below the initial design frequency of the upper and the lower bands respectively. This is attributed to the assembly error and slight bow that was observed on the

PRS dielectric laminate. Besides, the RCA design process starts with PRS unit cell simulation which is excited by a normally incident plane wave. But in the RCA, the PRS is illuminated by a leaky wave [5].

(a)　　　　　　　　　　(b)　　　　　　　　　　(c)
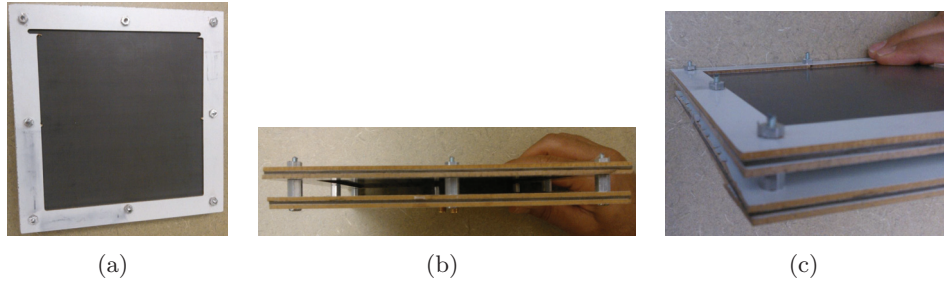
Figure 2.29. (a) Top, (b) side, (c) perspective view of the fabricated RCA.
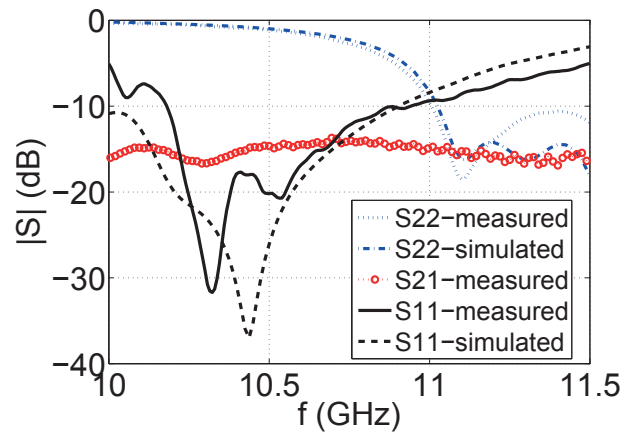
Figure 2.30. Simulated and measured S-parameters of the RCA for the two ports.

(a)

(b)

(c)

(d)
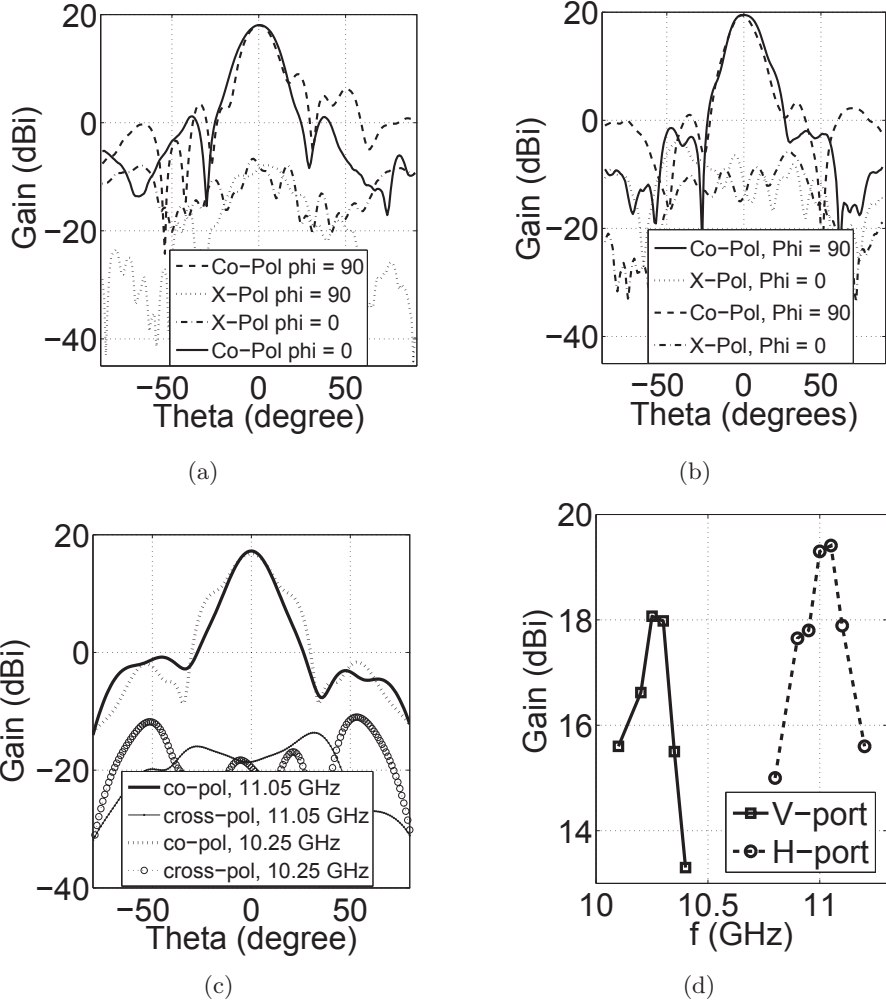
Figure 2.31. (a) Main plane measured co-polar and cross-polar gain of RCA for lower band at 10.25 GHz with V-pol and (b) upper band at 11.05 GHz with H-pol; (c) Main plane simulated co-polar and cross-polar gain of RCA for the lower band at 10.25 GHz with V-pol and the upper band at 11.05 GHz with H-pol; (d) Measured gain versus frequency.

2.2.6 Full Phase-Gradient PRS

Full Phase-Gradient PRS is used to generate an asymmetric single beam off broadside. In this method, a progressive phase shift is applied between adjacent unit cells across all PRS cells [33, 34]. This method is applied to the proposed PRS to demonstrate its beam steering potential. The cavity feed is in the middle of PRS (Fig. 2.22). Two PRS states are designed with progressive phase distribution along V-pol (y-axis) by varying slot length while the phase distribution along H-pol (x-axis) is uniform. It is demonstrated that by producing the phase distribution, the F1/V-pol beam steers while F2/H-pol beam remains at broadside. Both configura-

48

tions have 12 rows along y-axis and 12 columns along x-axis as shown in Fig. 2.32. The cells in each row are the same. The slot length distribution across PRS is summarized in Table 2.6 for both states. All other RCA parameters are the same as Section 2.1.4. Since the reflection amplitude of top surface is low for $l > 8.5$ mm, the length of slots is not extended beyond 8.5 mm. In state 1, l varies over 12 rows between $8.5 - 6.85$ mm which leads to $\theta = 17°$ at 10.6 GHz as shown in Fig. 2.33. This results in linear phase gradient across top layer. In state 2, l varies over 12 rows between $8.5 - 0$ mm which leads to $\theta = 29°$. For both RCAs, H-pol beam is in broadside at 11.05 GHz. Since the slot effective length can be controlled by switch array across the slot [13], the above structures show the potential of the proposed RCA to be used as the platform of a reconfigurable antenna.
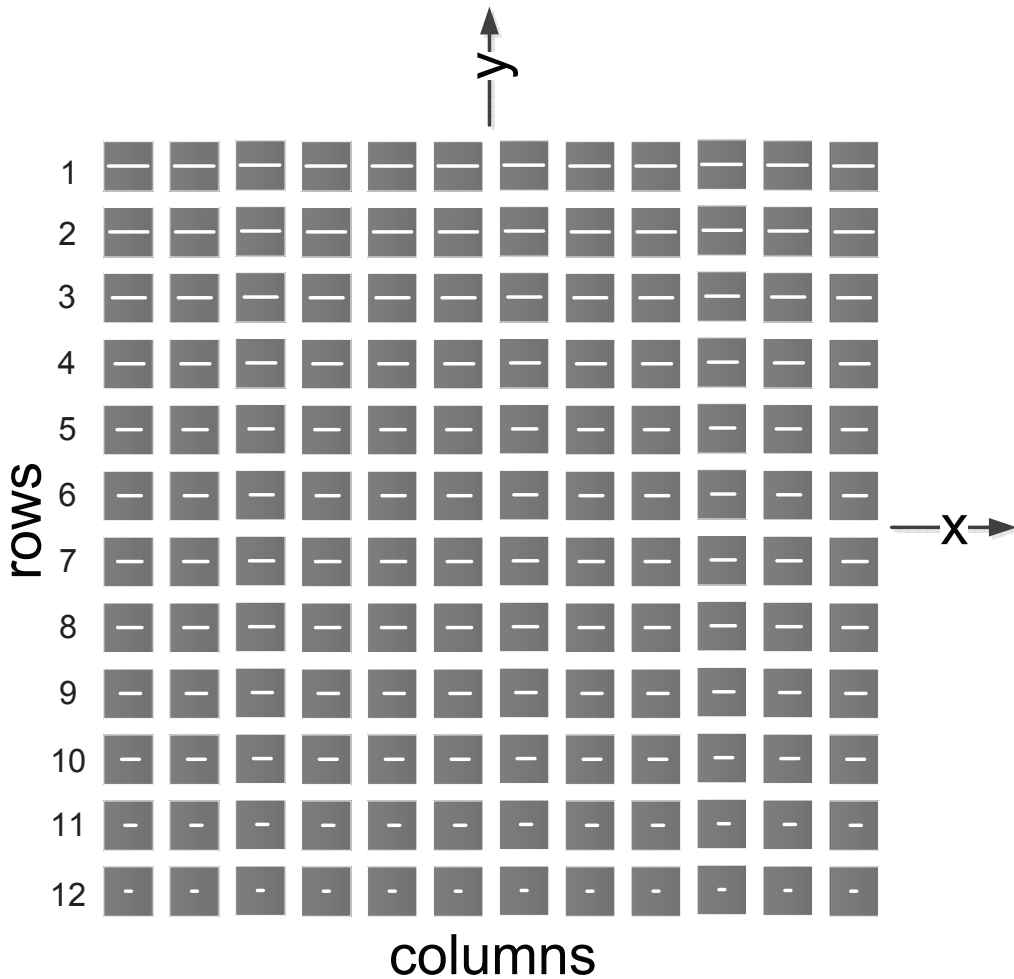
Figure 2.32. Schematic of the PRS with variation of slot length along y-axis.

row	1	2	3	4	5	6	7	8	9	10	11	12
state1	8.5	8.35	8.2	8.05	7.9	7.75	7.6	7.45	7.3	7.15	7	6.85
state2	8.5	7.73	6.95	6.19	5.42	4.65	3.88	3.11	2.34	1.57	0.8	0

Table 2.6. Distribution of slot length versus row number across PRS.
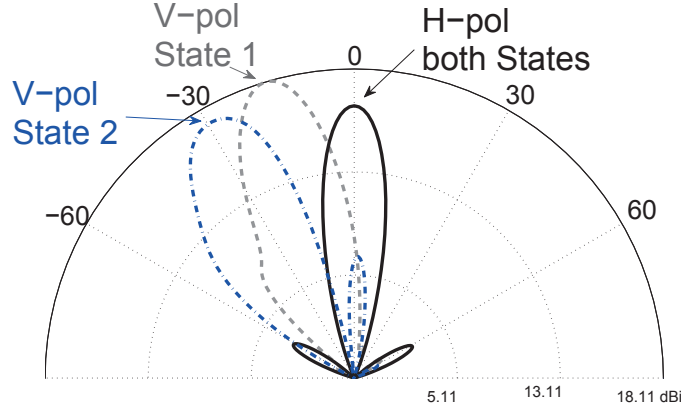
Figure 2.33. Normalized simulated antenna directivity pattern of RCA at State 1 and 2.

2.2.7 Independent and Arbitrary Control of the Resonant Frequencies

For most of the RCAs in the literature, it is not possible to control the bands independently or arbitrarily. For instance, for the RCAs employing artificial magnetic conductor instead of the regular perfect electric conductor (Fig. 1.10), since both resonant frequencies depend on the reflection phase from both ground plane and the PRS, changing any parameter in PRS or ground plane unit cells affects both resonant frequencies. Thus, they can not be chosen independently. Another structure is presented in [24] which uses double-sided PRS configuration (Fig. 1.10). Each side contains a periodic structure producing one of the resonant frequencies. The design is limited to the fact that the periodic structure associated with each resonant frequency has to be transparent to the other frequency, which makes both bands tightly dependent. One of the major advantages of the PRS unit cell proposed here, is the ability to independently and arbitrarily control each of the two RCA bands. This shows the potential of the proposed PRS for a variety of applications with various frequency band requirements. Independent fine control of the bands as well as implementing arbitrary separation between them is explained in this section.

Independent Fine-Control of the Bands

The frequency bands of the proposed structure can be independently fine-controlled using slot length for V-pol by uniformly changing the slot length across the PRS while H-pol band is fixed. Fig. 2.34(a) shows the simulation results indicating that by changing l uniformly in all the cells between $6-8$ mm, F1(V-pol) shifts between $10.35-11.1$ GHz and F2(H-pol) remains constant at 11.39 GHz. For these simulations, the unit cell sizes are $P = 11$ mm, $L = 10$ mm, $w = 1$ mm, and $h = 13.8$ mm and N(V-pol) = N(H-pol) = 2. This shows the potential of incorporating tuning elements such as MEMS or solid-state switches and varactors across the slot to control the slot effective length and control V-pol resonance [13].

Implementing Arbitrary Separation between the Bands

To have arbitrarily large separation in between the operating frequency bands, the height of cavity can be adjusted to higher N(resonant mode) values. In previous Section, $l = 8$ mm, $w = 1$ mm, and N(V-pol) = N(H-pol) = 2, led to resonant frequency separation of 0.8 GHz. Two other prototypes are designed to show larger frequency separations with higher values of N. Different combinations of N(V-pol) = 2, N(H-pol) = 3 in the first prototype and N(V-pol) = 4, N(H-pol)= 3 in the second prototype, lead to band separation of 5.75 GHz and 3.95 GHz respectively as shown in Fig. 2.34(b). For these two prototypes, $l = 7$ mm, $w = 0.2$ mm, $P = 11$ mm, and $L = 10$ mm are considered. The antenna characteristics including the unit cell parameters, h, directivity (D) and first side-lobe level (SLL) are summarized in Table 2.7. It shows that for different frequency separations, we could have nearly equal directivity with slight change in the side-lobe level.

RCA	(l,w) (mm)	h (mm)	Pol	N	F (GHz)	D (dBi)	SLL (dB)
Section. 2.2.5	(8,1)	13.8	V	2	10.3	20	14
			H	2	11.3	19	15
First Prototype	(7,0.2)	24.7	V	2	6.5	20.3	23.9
			H	3	12.25	20	10
Second Prototype	(7,0.2)	37.2	H	3	8.3	20.3	16.6
			V	4	12.25	19.7	10.3

Table 2.7. Simulation results of prototypes designed with different values of N.
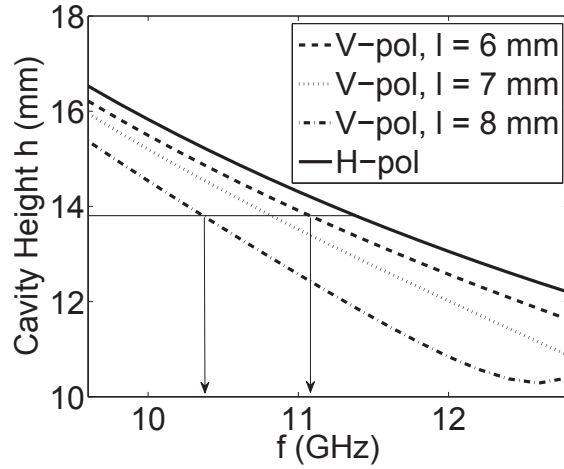
(a)
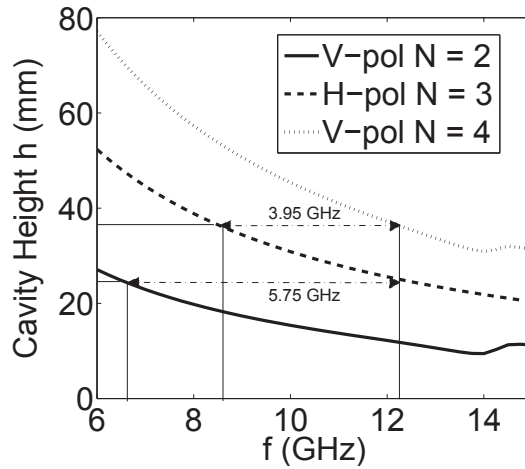
(b)

Figure 2.34. (a) Independent fine-control of the two polarizations. (b) Arbitrary separation between bands.

2.3 Comparison with Previous Work

This section compares the two designs proposed in this chapter with several dual-band RCAs in literature including the works authored by Hajj [31], Pirhadi [27], Kelly [25], Lee [24], Ge [28], and Kanso [22]. Table 2.35 shows their PRS unit cells and indicates the number of design parameters for each periodic structure ($M1$, $M2$), total number of design parameters ($M = M1 + M2$), number of supporting polarizations ($n1$) and bands ($n2$). For each design, it also explains if the bands are arbitrarily tuned. As can be observed, the proposed designs have the simplest structures and are the only ones with orthogonally-polarized dual bands.

2.4 Conclusion

This chapter demonstrated the RCA dual-band operation offering two different high-gain dual-broadside-beam RCA designs. A microstrip patch antenna was designed as the cavity feed for simultaneous reception and transmission in the upper and lower bands.

The first design had a PRS with two single-sided dipole arrays. Because of their unique shape, dipoles are not able to operate in dual bands and polarizations. This requires two single-sided dipole layers to cover for both bands. In order to make the PRS structure simpler and tunable, a single slotted patch PRS was offered. Slotted patches can house the tuning elements across their slot.

For both designs, it was shown that the two resonant frequencies are arbitrarily and independently controlled. Hence, these structure have the potential to be used in different commercial bands. Also, in order to make the design procedure easier, a design flow-chart with several examples were also provided.

An equivalent transmission line models simply explain the operation of complicated electromagnetic structures. Hence, for both PRS structures, a transmission line model was extracted at each polarization.

Next, the beam-steering capacity of slotted-patch PRS was verified. In order to realize RCA with beams off-broadside, PRS with non-uniform-phase cells should be used. The variation in slot length causes the gradient in phase across PRS. This method was applied to slotted-patch PRS unit cell to realize an RCA with one horizontally-polarized broadside beam and one vertically-polarized beam steered up to 29° depending on the total phase variation across PRS.

author	periodic sructure 1	M1	periodic sructure 2	M2	M	n1	n2	Are the bands tuned arbitrarily?
Hajj		3		4	7	1	2	No. Each resonant frequency is affected by the reflection phase from both periodic structures.
Pirhadi		3		6	9	1	2	No. The ground plane is an artificial magnetic conductor. The cavity resonates just at odd mode numbers. Thus, the bands are 3 GHz apart.
Kelly		3		3	6	1	2	Yes. The two periodic structures are at different height above the ground plane. The difference in their height controls the band separation.
Lee		3		2	5	1	2	No. The two bands are the odd mode number resonant frequencies of the cavity transmission response. The resonant frequencies are at least 3 GHz apart.
Ge		3	NA	NA	3	1	2	No. The two resonant frequencies are formed around the slot resonance. They can't be arbitrarily far or close.
Kanso		5		5	10	1	2	Yes. The two periodic structures are at different height above the ground plane. The difference in their height controls the band separation.
dual layer dipole		3		3	6	2	2	Yes. Dipoles of each layer control each resonance.
slotted patch		4	NA	NA	4	2	2	Yes. The patch dimensions and the slot dimensions control the two resonant frequencies independently.
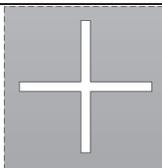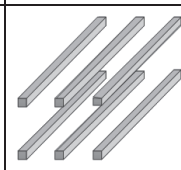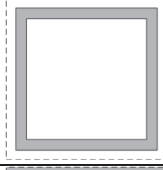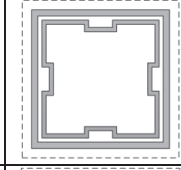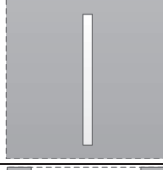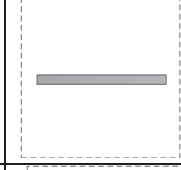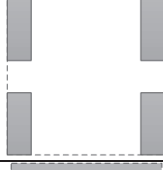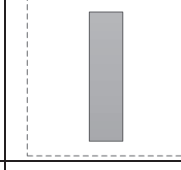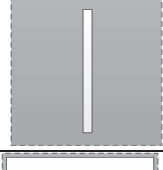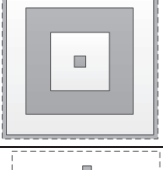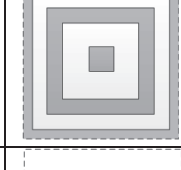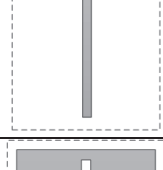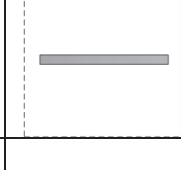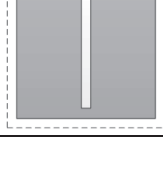
Figure 2.35. Comparison of the designs proposed in this chapter with dual-band RCAs in literature. Number of design parameters for each periodic structure: $M1$ and $M2$, total number of design parameters: $M = M1 + M2$, number of supporting polarizations: $n1$, bands: $n2$

Chapter 3

MEMS-tunable Resonant Cavity Antenna

This chapter investigates the tunability and beam forming of RCAs [64]. As a step-by-step procedure toward realization of antennas as templates for multi-functional apertures, tunability and beam forming are added to the dual-band slotted-patch PRS presented in previous chapter.

Generally, leaky wave antennas are known to generate 3 types of beams depending on their feeding technique, guiding structure and frequency of operation: broadside beam, azimuthally symmetric conical beam, and asymmetric off broadside single beam [5,9,65]. There are few studies on generation of asymmetric off broadside single beams in center fed RCAs which are the focus of this thesis [33, 36]. Traditionally, Full-Phase-Gradient (FPG) PRS structure is used to generate such a beam by RCA. In a FPG-PRS, a progressive phase shift is applied between adjacent PRS unit cells across the whole PRS. This chapter presents a novel Half-Phase-Gradient (HPG) PRS for this purpose [64]. In a HPG-PRS, the phase gradient is applied to only a half of PRS cells. The HPG method is fully compared to the traditional FPG method. The HPG method offers the advantages of faster real time tracking and enhanced scan profile compared to FPG-PRS.

Non-uniform leaky wave antennas structures have widely been used for manipulation of radiation [66]. However, little effort has been put into understanding the radiation phenomena of such structures. This chapter also presents a novel simple radiation model for gaining insight into the radiation phenomena of leaky wave antennas with non-uniform aperture. Assuming the PRS as a phased array, this model uses the analysis of unit cells to calculate the radiation pattern. In order to verify the model, it is applied to a highly nonuniform beam-scanning HPG-PRS

to calculate its radiation pattern and compared to its measurement results. It is demonstrated that the model is able to predict the main lobe profile and the antenna scan angle with an accuracy of 5°. Compared to previous leaky-wave models in state of the art, this model has no limitation on level of aperture non-uniformity, unit cell type, leaky wave antenna type, feeding technique, periodicity of aperture or even the radiated beam shape. Most of the models in literature focus on a specific type of non-uniformity, aperture periodicity which is much smaller than wavelength and the broadside beams [65, 67, 68].

Next, using the HPG structures, a multi beam switching orthogonally polarized independent dual-band center-fed RCA is designed. This antenna has a vertically-polarized broadside beam and a horizontally-polarized beam which is switched among all possible beam-forms of leaky-wave antennas depending on PRS configuration: a broadside beam, a symmetric conical beam, a frequency-scanned asymmetric single beam and also an asymmetric single beam which is steered at fixed frequency. This prototype is a step forward to realization of multi-functional apertures.

Dynamic control of the radiated beam requires tunable PRS unit cells. Finally, this chapter elaborates the design, fabrication and measurement of an in-house developed hybrid integrated MEMS-tunable PRS unit cell with 4 digital phase states. The dies of capacitive frozen MEMS switches are wirebonded across the slot of the PRS patch in order to tune the PRS phase and also manipulate the leaky wave propagation. This unit cell is the building unit for the above mentioned multi beam switching RCA. There is limited work on tunable leaky wave antennas. The only MEMS-tunable PRS in literature is developed in [38] with 2 digital phase states for realization of a uniform PRS with broadside beam and variable beamwidth.

3.1   Radiation Model

In order to understand the radiation phenomena in RCA, a model has to be investigated. In order to find this model, a PRS is assumed as an array of radiating elements. With this simple assumption in mind, the novel HPG-PRS structure is derived. Generally, array factor technique is used to find the radiation pattern of an array. Hence as the next step, the array factor of a linear array is extracted. Finally, this technique is applied to a general RCA with arbitrary unit cell shape, periodicity and distribution in order to calculate its radiation pattern.

3.1.1 Half Phase-Gradient Partially Reflective Surface

Fig. 3.1 depicts an RCA excited by a line source in the center of PRS half-way between the PRS and the solid ground plane. The PRS is composed of $2N \times 2M$ (along x and $y-axis$) unit cells of periodicity $P \times P$ which are the same along $x-axis$ and different along $y-axis$. The source stretches over $x-axis$ between $x = \pm NP$. The source launches a leaky wave inside the cavity. The electromagnetic energy carried out by the wave leaks out of cavity through the PRS since the reflection amplitude of PRS is close to but not equal to one [5, 16]. In this study, each PRS unit cell is assumed as an element of an array fed by the wave propagating inside the cavity. The radiating phase of each PRS cell (ψ_t) is the sum of the feed system phase delayed at the location of each cell (ψ) and the phase shift caused by the cell itself (ψ_{cell}):

$$\psi_t = \psi + \psi_{\text{cell}} \tag{3.1}$$

and

$$\psi = -k_y|y| = -\beta_y|y| \tag{3.2}$$

where k_y is the y-component of wave propagation vector in $y - z$ plane, β_y is the phase constant and y is the y-component of cell position. In this initial model, the wave attenuation due to leakage is ignored ($\beta \ll \alpha$). Generally, an RCA with a feed at the center generates a symmetric conical or broadside beam. But in here, it is desired to have a scanned non-conical asymmetric single beam in $y - z$ plane. In order to rotate the beam to a desired angle θ, a progressive phase shift has to be implemented along $y-axis$ [2]. The desired ψ_t along $y-axis$ should approximately be a linear function of position as

$$\psi_t = -\beta_y y + \psi_0 \tag{3.3}$$

where ψ_0 is an arbitrary constant. Thus, ψ_{cell} distribution is calculated as:

$$\psi_{cell} = \begin{cases} \psi_0 & y > 0 \\ -2\beta_y y + \psi_0 & y < 0 \end{cases} . \tag{3.4}$$

Hence, the cell phase has to be constant on one half of PRS and cancel the feed system phase delay in the other half of the PRS. This allows the inherent leaky-wave phase progress to be used and therefore the phase gradient could be applied only to half of the PRS surface. This is of significance when actual tuning elements are to be added to the PRS. Besides, this structure is a single-beam scanning antenna
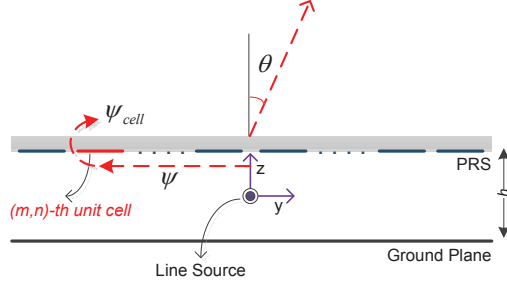
Figure 3.1. Phased array model of a LWA.
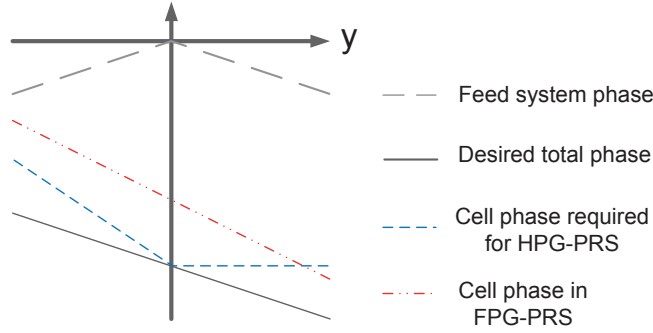
Figure 3.2. Phase distributions on LWA aperture.

since θ depends on β_y which is frequency-dependent. All of phase functions are demonstrated in Fig. 3.2 and compared with FPG-PRS.

3.1.2 Radiation of a Linear Array

In this Section, the radiation of a linear array is calculated [2]. Assume an array of $2M$ similar radiating elements distributed along y-axis with equal distances of P (Fig. 3.3). In $y - z$ plane, the array total radiated far-field (E_{total}) is calculated as:

$$E_{total}(r, \theta) = E_{element}(r, \theta) \times AF(\theta) \tag{3.5}$$

where $E_{element}$ is the radiated far-field electric field of a single element and AF is the array factor. The AF depends on the arrangement of elements in array configuration. For the above-mentioned array, if the m-th element is excited by current $I_m.exp(j\psi_m)$, then the AF is calculated as:

$$
\begin{aligned}
AF =& I_{-M}.\exp(j(\psi_{-M} + k_0.(-M + 0.5).P.\sin(\theta))) \\
&+ I_{-M+1}.\exp(j(\psi_{-M+1} + k_0.(-M + 1 + 0.5).P.\sin(\theta))) + \ldots \\
&+ I_M.\exp(j(\psi_M + k_0.(M - 0.5).P.\sin(\theta))) \tag{3.6}
\end{aligned}
$$
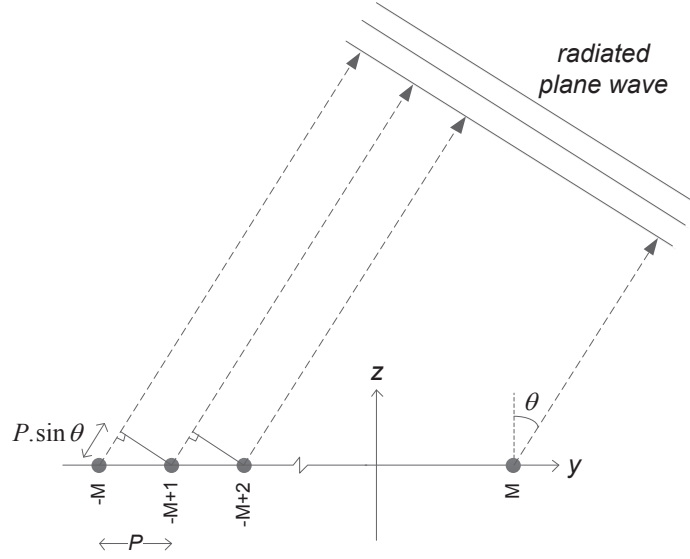
Figure 3.3. Linear array of similar elements which are excited by different currents.

The origin of coordinates is considered as the center of phase for radiation of the plane wave toward angle θ. The normalized array factor (AF_n) can be calculated as:

$$
\begin{aligned}
AF_n = {} & \sum_{m=-M}^{-1} i_m . \exp(j(\psi_m + k_0(|m| - 0.5)P\sin(\theta))) \\
& + \sum_{m=1}^{M} i_m . \exp(j(\psi_m - k_0(|m| - 0.5)P\sin(\theta)))
\end{aligned} \tag{3.7}
$$

where k_0 is the free space wave propagation constant and i_m is the element current amplitude normalized to the maximum current amplitude.

3.1.3 Radiation of a Non-Uniform PRS

RCAs with non-uniform PRS are widely used for beam forming. In this Section, the radiation of an RCA with arbitrary non-uniform PRS is calculated using the phased array theory and impedance parameter of multi-port microwave networks. Assuming the RCA demonstrated in Fig. 3.1, PRS cell in row m is fed underneath by the normalized current

$$
I(m) = \exp(-j\psi(m)) \ . \tag{3.8}
$$

In case of uniform PRS cells:

$$\psi(m) = k_y|y| = (m - 0.5)k_yP$$

$$= (m - 0.5)(\beta_y + j\alpha_y)P \qquad (3.9)$$

where α_yP is the cell attenuation and β_yP is equal to phase shift across the unit cell which are both obtained from the cell dispersion curve through eigen-mode analysis with Periodic Boundary Condition (PBC) around the cell and Absorbing Boundary Condition (ABC) on top of the cell (Fig. 3.4(a)). The term $m - 0.5$ is used instead of m, assuming the cell radiation center is in the middle of the cell [17]. Eq. 3.9 does not apply to non-uniform PRS, where each cell has its own dispersion. However, approximately

$$\psi(m) = \sum_{i=1}^{m-1} \phi(i) + \frac{\phi(m)}{2} \qquad (3.10)$$

where $\phi(i)$ is the phase shift across unit cells which are situated between the source and the cells in row m. In Eq. 3.10, the term $\phi(m)/2$ is used instead of $\phi(m)$ assuming the cell radiation center is in the middle of the cell [17]. Considering the unit cell as a two-port network where port-1 is inside the cavity and port-2 is outside (Fig. 3.5(a)), using the impedance parameters:

$$[Z] = \begin{bmatrix} Z_{11} & Z_{12} \\ Z_{21} & Z_{22} \end{bmatrix} \qquad (3.11)$$

the voltage induced on port-2 of the cells in row m is described as:

$$V_2(m) = Z_{21}(m).I_1(m) +$$

$$Z_{22}(m).I_2(m) \qquad (3.12)$$

and since the cell is only excited on port-1 (Fig. 3.5(a)):

$$V_2 = Z_{21}.I_1 \quad . \qquad (3.13)$$

The normalized PRS Array Factor (AF) for radiation in y-z plane is calculated:

$$AF = \sum_{m=-M}^{M} \sum_{n=-N}^{N} V_2(m).$$

$$\exp(-jk_0mP\sin(\theta)) \qquad (3.14)$$

and hence

$$AF(f, \theta) = \sum_{m=-M}^{M} \sum_{n=-N}^{N} Z_{21}(m).$$

$$\exp(-j(\psi(m) + k_0mP\sin(\theta))) \quad . \qquad (3.15)$$

Although this method is applied here to a non-uniform RCA, it can be used for any type of leaky-wave antenna.

For the case of a cavity excited by a microstrip patch antenna, Eq. 3.8 should be modified. Although the patch antenna excites a spherical wave, an outward traveling cylindrical wavefront propagates inside the cavity which is described by cylindrical Hankel function [69]. The dominant mode of this cavity is $TM00$ since it propagates energy effectively at smaller radii than any other mode [70]. The field components of this mode are

$$E_z = \frac{k^2}{j\omega\varepsilon}.H_0^{(2)}(k_\rho\rho) \tag{3.16}$$

$$H_\varphi = k.H_1^{(2)}(k_\rho\rho) \ . \tag{3.17}$$

Since the current induced on the cell is equal to the tangential magnetic field, $H_1^{(2)}$ is used for calculation of the array factor. With a cylindrical wave feeding the PRS, the cells in a row are not going to have the same excitation and a 2-dimensional AF should be considered. However, for simplicity, only for calculation of the pattern in $y-z$ plane, 1-dimensional AF is used.
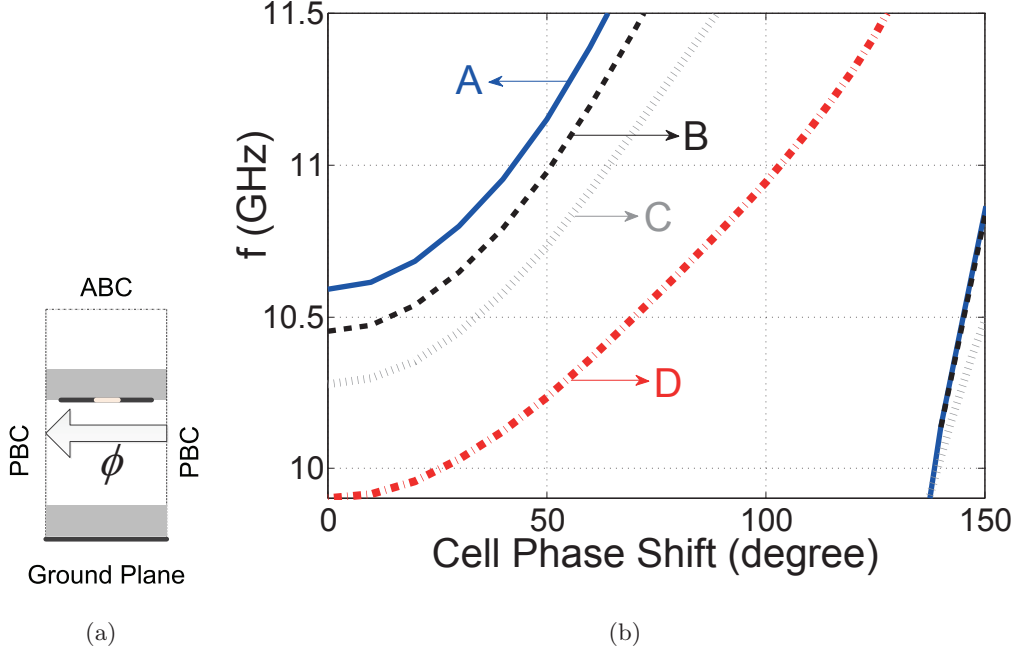
Figure 3.4. (a) Side-view of RCA unit cell used to find the dispersion diagram and the cell phase-shift including PRS and the cavity underneath; (b) Dispersion diagram of the RCA unit cell for different slot lengths.
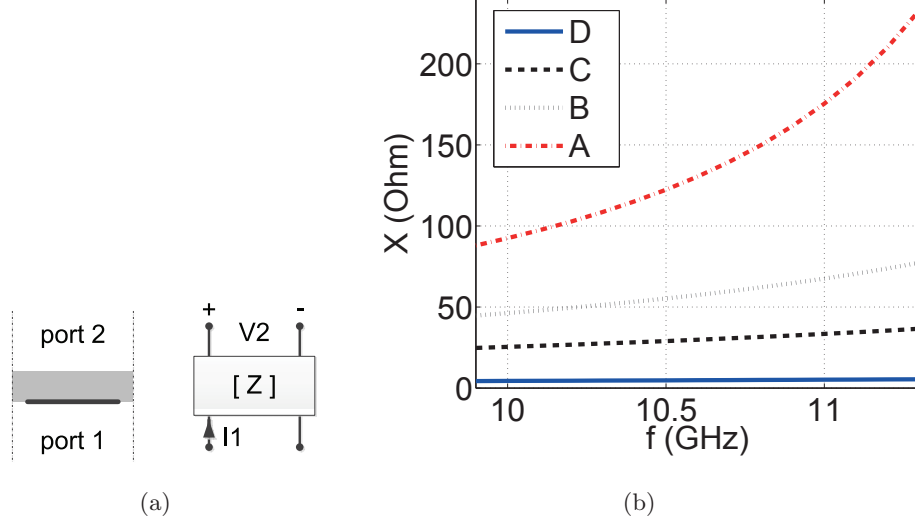
Figure 3.5. (a) Equivalent 2port network model of the PRS unit cell; Side view of unit cell; (b) Imaginary part of Z21 of the slotted patch unit cell versus frequency for different slot lengths.

3.2   Implementation of the HPG-PRS

In this section, the HPG method is applied to the slotted-patch PRS unit cell to realize beam steering with frequency and also at fixed frequency. Then, the radiation model is used to calculate the pattern of a HPG-PRS. The comprehensive comparison of HPG and FPG-PRS is also presented.

3.2.1   Half Phase-Gradient PRS for Beam Scanning with Frequency

Fig. 3.6 shows the PRS unit cell that is used. This square slotted-patch PRS unit cell has the benefit of supporting independent orthogonally-polarized dual bands with only a single layer of metallization [62, 71]. The cell reflection is controlled by L at Veryical Polarization (V-pol) and by (l, w) at Horizontal Polarization (H-pol) independently if $w \ll L$. Before inspecting the operation of HPG-PRS with the mentioned unit cell, an RCA is designed with a uniform PRS. The RCA design begins by simulating the reflection of the PRS unit cell with periodic boundary condition. In the desired bands of operation, a high reflection amplitude ensures a high radiation efficiency and the reflection phase determines the cavity height (h). Reference [71] includes all the graphs that show the effect of cell parameters on its reflection. Ray tracing method is the simplest way to calculate the height of a

uniform RCA with broadside radiation [17]. According to this method,

$$h = \frac{c}{4f}(2N - 1 + (\frac{\angle\Gamma}{180°}))$$ (3.18)

where c is the speed of light, f is the resonant frequency, N is an integer number, and $\angle\Gamma$ is the PRS reflection phase in degrees. Eq. 3.18 is once written for V-pol with f_V, N_V, and $\angle\Gamma_V$ and once for H-pol with f_H, N_H, and $\angle\Gamma_H$. In order to realize a dual-band RCA, both equations should lead to the same h.

A PRS unit cell with sizes of P (periodicity) = 11 mm, L (patch length) = 10 mm, w (slot width) = 1 mm, and l (slot length) = 8.5 mm is simulated by Ansys HFSS to get its reflection at both polarizations. With $N_V = N_H = 2$ and $h = 14.52$ mm, the cavity resonates at $f_H = 9.6$ GHz and at $f_V = 11.14$ GHz.

The HPG-PRS is realized by variation in the slot length (l). Since the operating bands are independent and have orthogonal polarization, this variation only affects H-pol. Fig. 3.7(a) and 3.7(b) depicts the normalized H-pol unit cell reflection phase ($\angle\Gamma$) and amplitude versus slot length (l) for three different frequencies around the resonances of uniform RCA. Fig. 3.7(b) shows that l should be smaller than 8.5 mm to ensure high reflection amplitude [64].
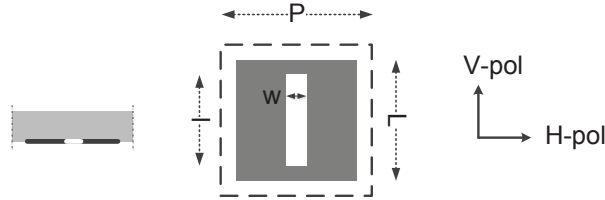
Figure 3.6. Side view and top view of the PRS unit cell
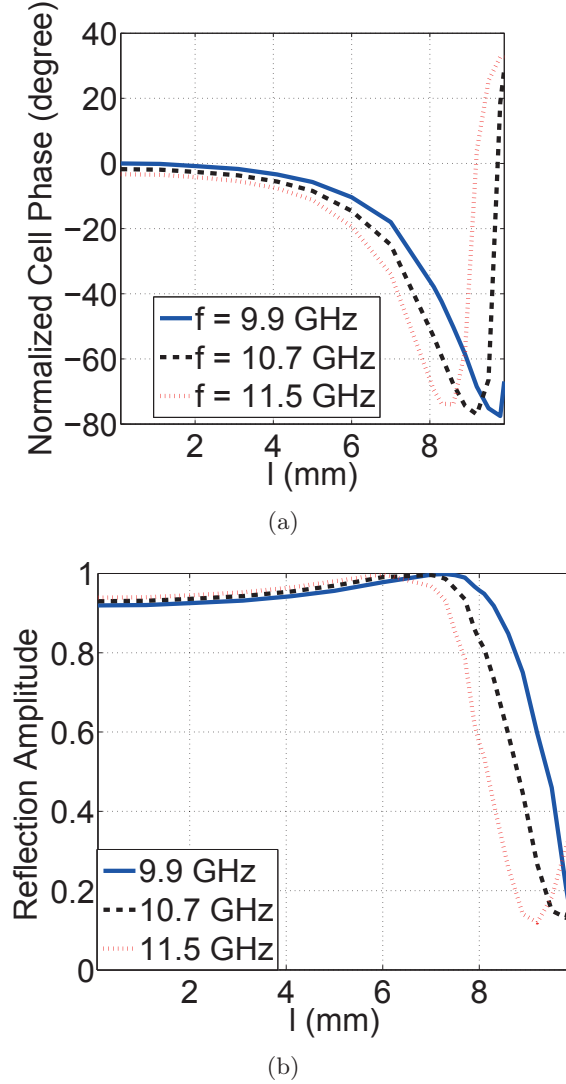
Figure 3.7. (a) Reflection phase, (b) reflection amplitude of PRS unit cell at H-pol versus effective slot length for different frequencies.

The first HPG-PRS is shown in Fig. 3.8. HG-1 includes 12×12 cells ($5\lambda \times 5\lambda$ (lower-band)) which are the same along the x-axis (columns) and different along the y-axis (rows). HG-1 PRS has four slot lengths: $l = 8.5$ (cell A), 7.5 (B), 6.5 (C) and 4 mm (D).

Since these slot lengths will be synthesized by RF-MEMS switches (Section 3.3.1), only four slot lengths with enough phase difference are picked.

In HG-1, cell A is used for the uniform Half of PRS, while two rows of cells B, C, and D are used in the gradient half of PRS. In the gradient half, as $|y|$ increases, the reflection phase increases. In order to investigate the beam-forming of RCA with HG-1 PRS, its radiation pattern is first calculated by the radiation model developed
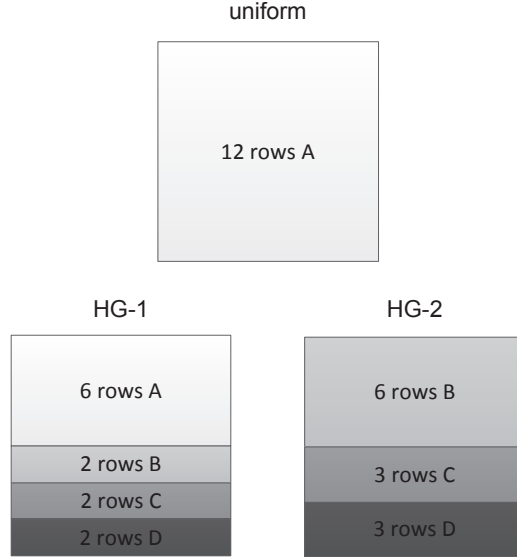
Figure 3.8. Slot length distribution in uniform, HG-1 and HG-2 PRS configurations

in Section 3.1.3. Then, it is fabricated and measured. Finally, the patterns by model and measurement are compared.

Calculated Radiation Pattern for HG-1 PRS

In order to apply Eq. 3.15 to HG-1 PRS, the PRS cell impedance and the RCA cell dispersion should be found. The eigen-frequency analysis of the RCA unit cell and the 2-port network analysis of the PRS unit cell are done using CST Microwave Studio and Ansys HFSS. Fig. 3.4(b) depicts frequency versus ϕ for cells $A - D$. The minimum simulated eigen-mode quality factor for cells A, B, C, and D in this frequency range is 1173, 858, 847, and 850 respectively. Since the quality factor is proportional to $\frac{\beta_y}{\alpha_y}$, α_y is ignored for the structure under study. Fig. 3.5(b) depicts the imaginary part of unit cell Z_{21} versus frequency for different slot lengths which is purely inductive since the real part of Z_{21} is ignorable. Very little change is observed in the impedance of cells C and D compared to A.

The calculated scan angle for the whole frequency range and pattern for two of the frequencies, is demonstrated in Fig. 3.9, 3.10(a), and 3.10(b). As the frequency changes from 9.9 to 11.3 GHz, the H-pol single beam scan angle changes from 8 to 54°.
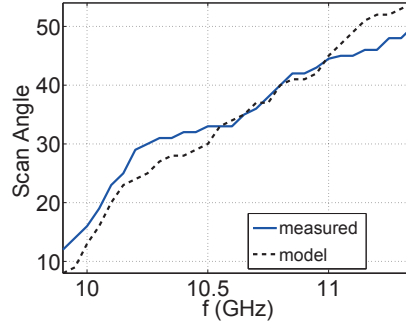
Figure 3.9. Comparison of scan angle obtained by measurement and a phased array model for HG-1 PRS.

(a)   (b)
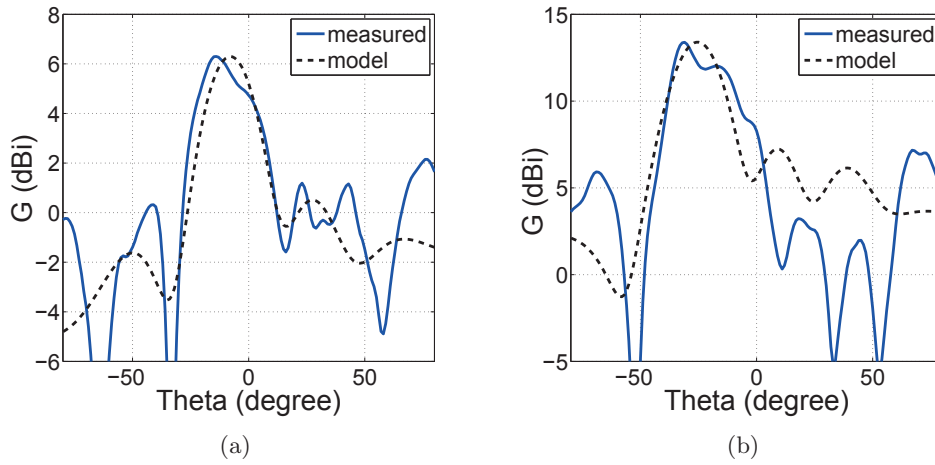
Figure 3.10. Comparison of pattern obtained by measurement and a phased array model with H-pol at (a) 9.95 and (b) 10.35 GHz. Phased array model is elaborated in the last Section.

Fabrication and Measurement of RCA with HG-1 PRS

An orthogonally-polarized dual-band microstrip patch antenna is designed as the RCA feed. It is printed on the above-mentioned laminate and uses the RCA bottom surface as the ground plane. The microstrip patch is fed by two microstrip transmission lines connected to SMA connectors independently for each band/polarization (Fig. 3.11(a)). The fabricated PRS and RCA top and side view are depicted in Fig. 3.11(b), 3.11(c), and 3.11(d) respectively. The measured and simulated RCA S-parameters are shown in Fig. 3.12. The measured and simulated RCA S-parameters are in good agreement. The measured gain and scan-angle versus frequency are shown in Fig. 3.13 and 3.9 respectively. As the frequency changes from 9.9 to 11.3 GHz, the H-pol single beam scan angle changes from 12 to 50°. The antenna pat-

66

terns in the upper half-space for 9.95 and 10.35 GHz are shown in Fig. 3.10(a) and 3.10(b) respectively.

Comparing the results from model and measurement, shows that the model predicts the scan angle and also the main-lobe beam-width with an accuracy of 5°. This verifies the accuracy of the radiation model developed in Section 3.1.3. The main sources of error in this model are the mutual coupling of adjacent PRS unit cells which is ignored and also using unit-cell dispersion in an array of unlike elements.
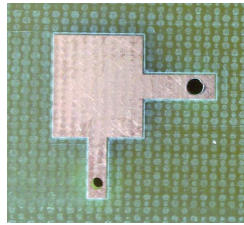
(a)
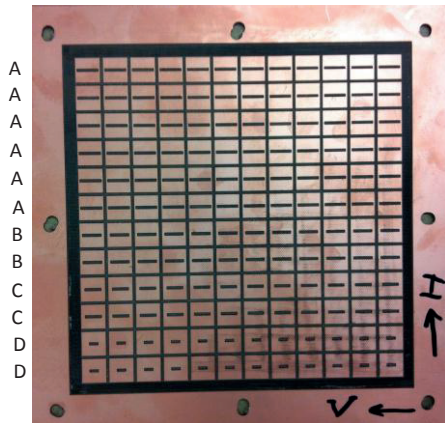
(b)
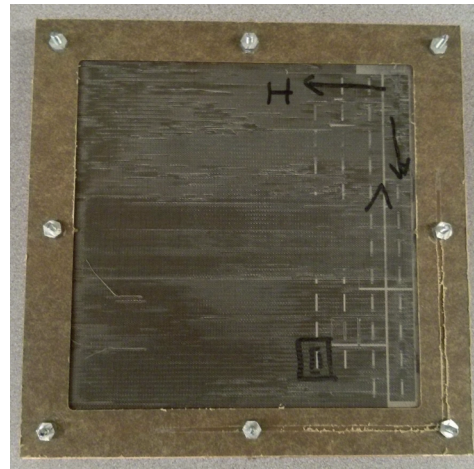
(c)

(d)

Figure 3.11. (a) Orthogonally-polarized dual-band microstrip patch antenna that feeds the RCA. (b) Fabricated HG-1 PRS. (c) Top view of RCA (d) Side view of RCA.
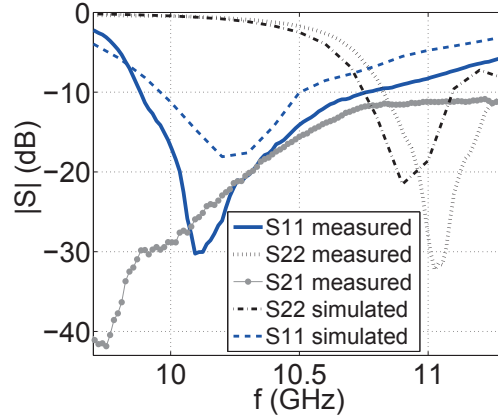
Figure 3.12. Simulated and measured S-parameters of HG-1 antenna.
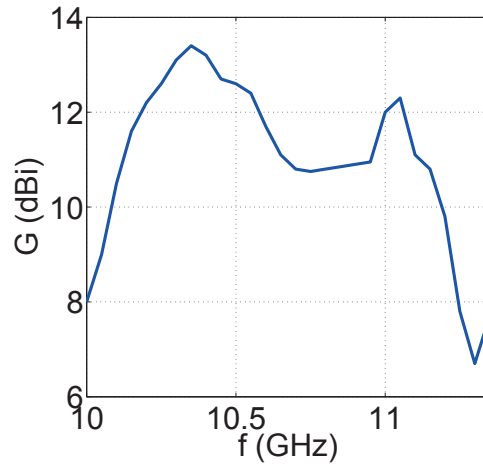
Figure 3.13. Measured H-pol gain versus frequency.

3.2.2 HPG-PRS for Beam Steering at Fixed Frequency

In this Section, the special features of the PRS unit cell and the HPG concept are utilized together to make a beam steering antenna at two fixed frequencies. By controlling the effective slot length across the PRS using tuning elements, the H-pol pattern can be controlled at a fixed frequency. HG-2 with a different slot length distribution is used here as the alternate HPG-PRS configuration (Fig. 3.8). At 10 GHz, changing the configuration from HG-1 to HG-2, changes the scan angle from 16° to −53° with 6-dB lower directivity. This directivity loss is because of the fact that the new scan angle is 69° off the initial scan angle and both far from broadside. Generally, the directivity of radiation drops as scan angle increases [2]. This also leads to emergence of a high side-lobe at 60°. Also at 10.4 GHz, changing

the configuration from HG-1 to HG-2, changes the single beam at 32° to 23° with similar directivity. All the normalized switched radiation patterns are depicted in Fig. 3.14(a) and Fig. 3.14(b). Since the two operating bands of this specific RCA are independent and have orthogonal polarization, the V-pol beam points to broadside with 14 dBi gain at 11.14 GHz for all PRS H-pol configurations.

The dynamic control of effective slot length can be done using switches across the slot.
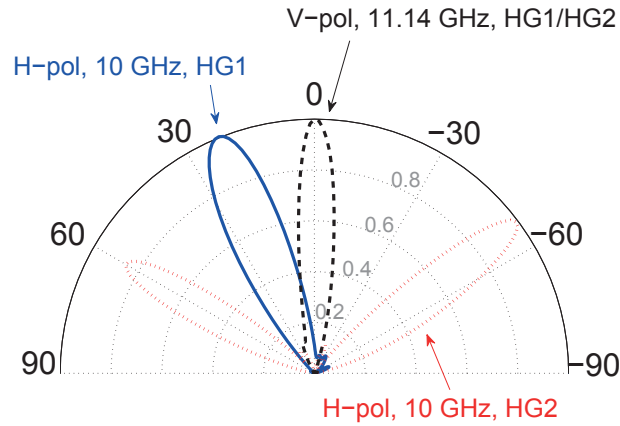
(a)
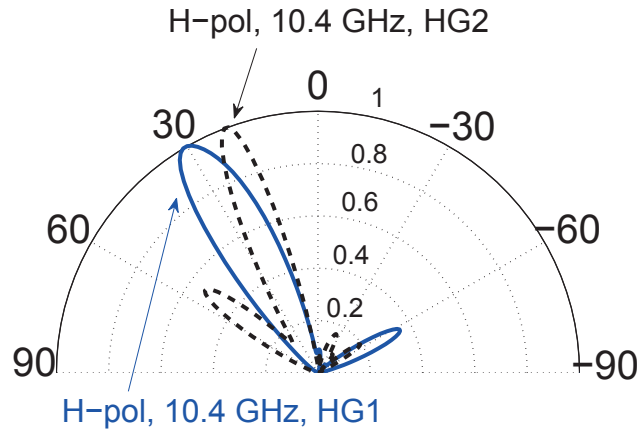
(b)

Figure 3.14. Switching of radiation pattern when switching between HG-1 and HG-2 (a) at 10 GHz with H-pol and 11.15 GHz with V-pol (b) at 10.4 GHz with H-pol.

3.2.3 Comparison of HPG and FPG-PRS in Frequency Scanning

The advantages of HPG-PRS over FPG-PRS are revealed especially when trying to implement a beam-switching RCA using phase-tunable PRS unit cells. If a single beam is required to be steered in only one half-space off broadside, the tuning elements are required to be installed in only half of PRS cells. This is not only a decrease in cost; the fabrication is going to be much simpler and the operation and controlling of the tuning elements is going to be less complicated.

However, if both half-spaces are desired to be scanned, the tuning elements are installed in all unit cells. In a fully-tunable PRS, the HPG configuration provides an improved scan profile and faster real-time tracking compared to FPG configuration. These advantages facilitate lower-cost implementation of reconfigurable apertures. The advantages are discussed as follows.

Improved Scan Profile

Fig. 3.15 shows the inherent phase progress of leaky wave propagation inside the cavity. This graph is symmetric around the center since the source is at the PRS center. For a uniform PRS, this symmetric phase leads to a symmetric radiation which is either broadside or conical. However, producing an asymmetric single beam requires an asymmetric phase distribution of a non-uniform PRS such as a FPG- or HPG-PRS which adds up to the inherent leaky-wave progressive phase. For a FPG-PRS, the available PRS unit cell phase shift is distributed over all PRS cells while in a HPG-PRS, the phase shift is distributed over half of PRS area. For the specific slotted patch unit cell, the total phase shift is about $60°$ (Fig. 3.7(a)). A HPG-PRS utilizes the leaky-wave progressive phase in one half and the unit cell phase shift in the other half (Fig. 3.15). Ignoring the leaky-wave progressive phase in FPG-PRS results in wasting half of the tunable phase range available by the unit cell. Hence, the most important benefit of using HPG-PRS is a more efficient utilization of available tunable phase of PRS unit cell since any shape of PRS cell integrated with tuning elements can provide a limited phase range. A specific tunable PRS unit cell can provide a higher scan range (maximum scan angle) in HPG configuration compared to FPG configuration.
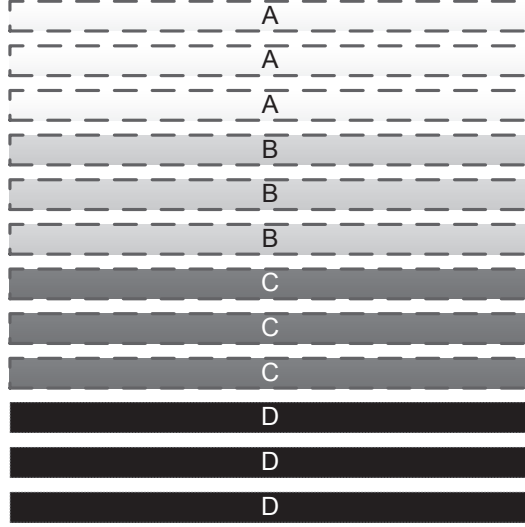
Figure 3.16. FG-2 PRS.
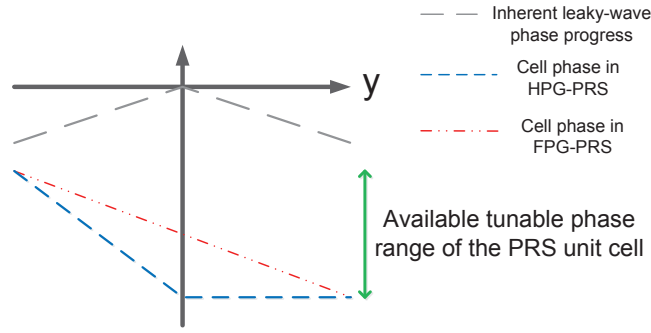
Figure 3.15. Phase functions versus position on PRS

In order to have a quantitative one-to-one comparison, the frequency scanning properties of two different configurations of FPG-PRS are also examined. In FG-1 PRS, the slot length changes gradually between 8.5 mm and zero across 12 rows. The slot length variations result in linear distribution of phase across PRS. As frequency changes from 9.8 to 10.6 GHz, the scan angle changes between 14 to 28°. However, for a FPG-PRS with discrete phase states the scan properties are worse. Fig. 3.16 depicts FG-2 PRS comprising the above-mentioned cells A, B, C, and D. The FG-1 phase gradient is weak and can not oppose the inherent phase progress of the leaky wave inside the cavity. Hence, it does not provide a continuous and uniform scan profile. The scan angle and gain of FG-1 and FG-2 PRS are shown in Fig. 3.17(a) and 3.17(b) respectively. Present HPG design also outperforms the FPG structure proposed by Ourir [33–36] with maximum scan angle of 29°.

71
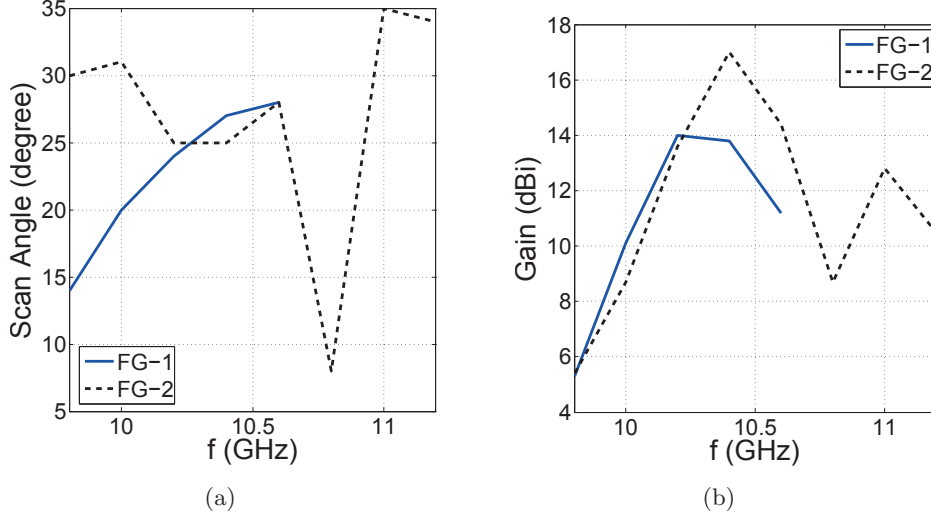
Figure 3.17. (a) Scan profile of FG-1 and FG-2 PRS. (b) Gain of FG-1 and FG-2 PRS.

Faster Real-Time Tracking

Fast tracking is a critical parameter of scanning antennas. To track a target by this beam-scanning antenna, the network of DC bias lines should be connected to a Digital to Analog Converter (DAC) and then to a micro-controller or a Digital Signal Processor (DSP). The micro-controller or DSP uses different signal processing algorithms such as zero-knowledge beam-forming algorithm for tracking of the received signal [72].

In a HPG-PRS, uniform phase distribution in one half, increases the algorithm computational efficiency and makes the tracking much faster by decreasing algorithm convergence time [73].

3.3 A MEMS-tunable Beam-Shaping RCA

RCA beam-switching requires tunable PRS unit cells. The tuning of the slotted patch unit cell is realized by changing the equivalent slot length using switches across the slot. This section first investigates the realization of the tunable unit cell using in-house developed MEMS switches. Then, this unit cell is used to reconfigure the PRS and implement a beam-shaping RCA. This RCA uses different HPG structures to synthesize all beam-shapes that could be generated by leaky-wave antennas.

Table 3.1. Different states of PRS unit cell

state	switch state	equivalent l
A	000-000	8.5 mm
B	100-001	7.5 mm
C	110-011	6.5 mm
D	111-111	4 mm
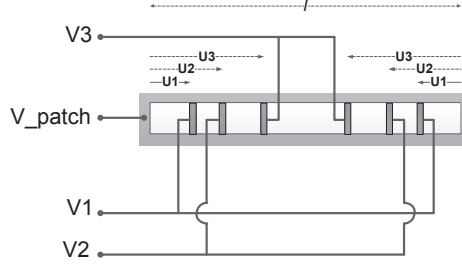
Figure 3.18. Switches installed across the slot.

3.3.1 MEMS-tunable PRS Unit Cell

A reconfigurable RCA requires tuning of unit cells on PRS. The tuning of the slotted patch unit cell is realized by changing the equivalent slot length using switches across the slot. Six shorting strips represent switches in ON-state in order make the equivalent slot length of the cells $A - D$. The switches are located at $U1 = 0.3$ mm, $U2 = 0.6$ mm and $U3 = 1.5$ mm along a 8.5 mm slot (Fig. 3.18). The slot length is limited to 8.5 mm in order to ensure partial reflection. Among many different switch configurations, only four are used here. The cell state, switch configuration and their equivalent slot length is listed in Table 3.1. Then, the shorting strips are replaced by RF-MEMS switches in frozen-state.

Measurement Setup

In order to inspect the reflection and transmission of an infinite array of unit cells, the commercial electromagnetic simulators provide a periodic boundary condition around the unit cell and illuminate the unit cell with the incident wave of the desired mode-number. However, this is not practical to fabricate and measure an infinite array to verify the simulations.

WaveGuide (WG) simulator is a technique for inspection of an infinite array of unit cells [74,75]. In this technique, a single unit cell is fabricated and fixed inside a metal waveguide. The waveguide is excited with its dominant mode which is $TE10$ for the rectangular guides. $TE10$ mode can be resolved to two TEM plane waves
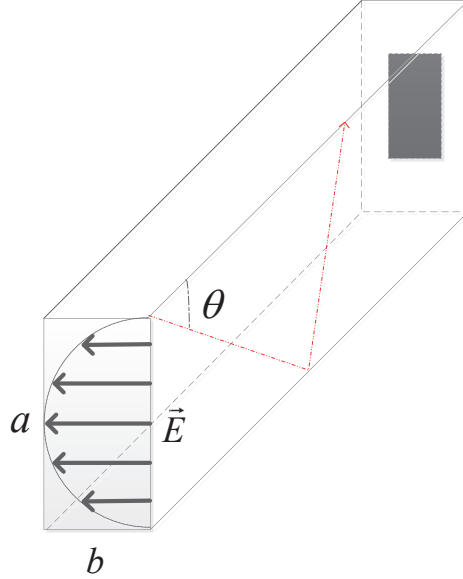
Figure 3.19. WG setup used to measure the reflection of an infinite array of cells.

incident upon the cell with the angle

$$\sin(\Theta) = \frac{\pi}{ka} \tag{3.19}$$

where a is the length of WG cross-section and k is the propagation constant in free space (Fig. 3.19). The selection of the commercial waveguide is according to the frequency range and the unit cell sizes. The periodicity of PRS unit cell is 11×11 mm with patch size of 10×10 mm. The standard X-band WG (WR90) covers our operating frequency range. But WR90 inner size is 22.86×10.16 mm. With a perfect fabrication, dicing process and alignment inside the waveguide cross section, the patch top and bottom edges will be 80 μm away from waveguide walls. This is of high risk since the patch edges might touch the WG walls and distort results. Hence, a wider WG frame is designed to be placed between VNA WR90 ports and house the cell (Fig. 3.20). All sizes of the frame are the same as WR90 except the inner width which is 11 instead of 10.16 mm (Fig. 3.21(a) and 3.21(b)). The thickness of frame is 3.18 mm. A 10×10 mm patch with a 8.5×1 mm slot is fabricated by electroplating 3.5 um of Gold (G) on a 0.525 mm thick Quartz wafer of $\varepsilon_r = 3.78$ and $\tan \delta = 0.0004$.
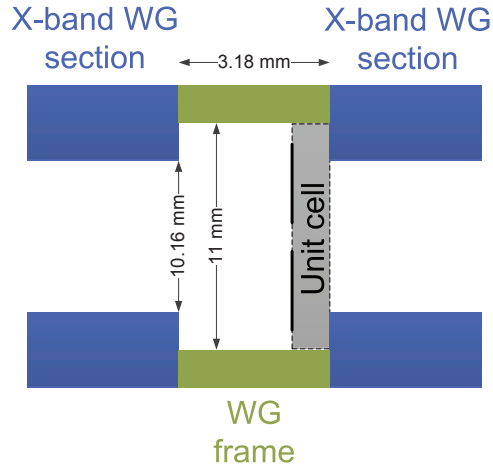
Figure 3.20. Schematic side view of the measurement WG setup.

Figure 3.21. (a) Measurement setup including two WR90 waveguides and the frame housing the unit cell; (b) Frame with a unit cell fixed inside.

Fabrication Process

The MEMS devices are fabricated separately (Fig. 3.22(a)) and then hybrid-integrated to the patch by wirebonding (Fig. 3.22(b)). The RF-MEMS capacitive switches are designed and fabricated at University of Alberta Nanofab cleanroom facility using 6 masks and layers on Quartz wafer (Fig. 3.22(c)). Layer 1 is a 100 nm thick and 10 μm wide reactively sputtered Tantalum Nitride (TaN) layer forming DC bias lines of resistivity 7.2×10^4 Ω/Sq. A magnetron sputtered 10/100/10 nm TiW/Gold/TiW forms switch bottom plates at layer 2. TiW is a 20/80% alloy of Titanium and Tungsten used as the adhesion between Gold and other layers. Layer 3 is a 150 nm Plasma Enhanced Chemical Vapor Deposition (PECVD) Silicon Nitride which insulates switch top and bottom plates. Layer 4 and 5 are the dual photoresist sacrificial layers made of LOR 5B and HPR 504. Then, a 30/250 nm TiW/Gold layer is magnetron-sputtered as the seed for electroplating of a thick Gold layer.

75

The magnetron sputtering happens at base pressures of as low as several 10^{-6} Torr. However, resists may outgas at these low pressures and destroy the sputtering process. Hence, prior to Layer 6, the wafers are post-baked for 120 seconds at 100° C. The TiW/Gold layer is used as the seed for electroplating 950 nm of Gold under 75 mA in a Techni-Gold 25 E S non-cyanide solution of pH 7.23. Prior to dicing, the wafer is coated by a protective HPR 504 photoresist layer and then baked for 2 minutes at 115° C. The switches are diced and then released in a combination of dry and wet steps. The dry step is done by Reactive Ion Etching (RIE) under Oxygen-sripping recipe. The wet step includes soaking in Actone, MF319 and Isopropyl Alcohol for 30, 5, and 5 minutes respectively. MF319 is the commercial developing solution for LOR 5B. There is a high risk of stiction of MEMS cantilever to bottom electrode after samples are transferred out of Alcohol dish. Hence, the samples are finally dried in a Critical Point Drier by Carbon Dioxide to avoid stiction.

Characterization

The operation of MEMS switches are tested by DC/RF probe station. For this purpose, some switches are designed with Co-Planar Waveguide (CPW) port. As depicted in Fig. 3.22(d), the RF probe sits on the CPW port on the left and the DC probe sits on the DC pad at the right to actuate the switch. The two ground lines of the CPW are connected to the switch top plate and the signal line is connected to the bottom plate. The switch pull-in voltage is 72 V and the ON-state insertion loss is 0.6 dB.

Integration

To control all MEMS switches in a cell, four separate DC bias lines are required. Since the MEMS switches have separate DC and RF pads, and the RF pads (top and bottom plates of capacitive MEMS switch) are all connected to the patch, one line is needed to control the DC voltage of patch and three other lines should control the switches. Due to complexity of implementing the bias lines and routing them out of the WG setup, frozen state MEMS switches are used. To facilitate bonding, the switch ports are connected to circular pads of 70 μm diamater (Fig. 3.22(a)). Since the overall area of a single switch with its pads is about 300 μm $\times$ 500 μm, the switches are prepared in bigger dies for easy handling by tweezers. Hence, the switches are prepared in 2 $\times$ 1 arrays of 500 μm $\times$ 1500 μm (Fig. 3.22(b)).

76

Before wire-bonding, the MEMS dies should be glued to the unit cell using KMPR photoresist and baked for 5 minutes at 100° C.

The MEMS switches have successfully tuned the reflection of PRS unit cell (Fig. 3.23(a) and Fig. 3.23(b)). Although the reflection phase is tuned, the reflection amplitude remains higher than 0.63 which ensures partial reflection. The simulated and measured cell phase and amplitude are in good agreement. The assembly error causes the measured reflection amplitude to be lower than simulation.

(a)

(b)

(c)

(d)
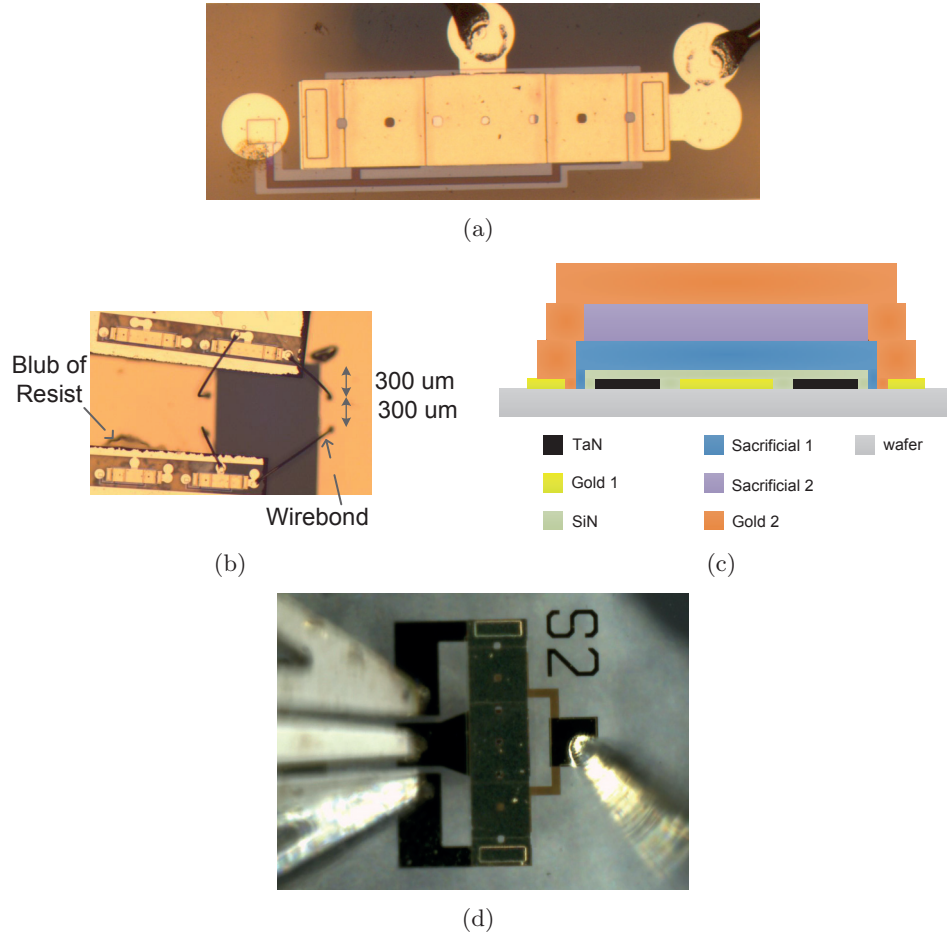
Figure 3.22. (a) Capacitive MEMS switch; (b) MEMS switches wire-bonded across the slot; (c) Cross section of layer structure of MEMS switches; (d) Stand-alone MEMS switch with coplanar waveguide port under RF probe station: RF port is on the left side and the DC probe is on the DC pad on the right side.
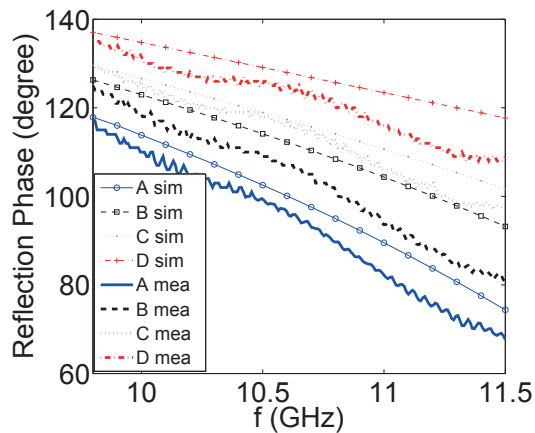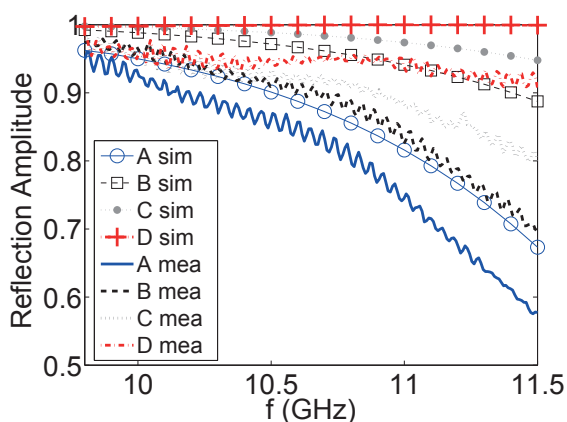
Figure 3.23. Comparison of measured and simulated reflection (a) phase (b) magnitude of the PRS unit cell with capacitive MEMS switches.

3.3.2 A Beam-Shaping RCA

In order to realize an antenna which can switch its beam among different beam-shapes, a tunable PRS unit cell needs to be used. Tuning elements such as MEMS or solid-state switches or varactors can be integrated in PRS cell to control its reflection phase [37, 38]. However, MEMS technology outperforms solid-state in terms of DC power consumption, nonlinear effects such as intermodulation distortion, and loss. Although a lot of effort has been put into realizing reconfigurable aperture antennas such as reflectarrays [32], reconfigurable RCAs have received less attention. The only reported MEMS-tunable PRS unit cell is reported in [38] for implementing a beam-width-reconfigurable broadside-beam RCA. For the unit cell used in present work, the MEMS switches can be installed across the slot to control the cell reflection only in one of the bands (Fig. 3.18). Using six symmetric switches across the slot can

Table 3.2. Different beams generated by the reconfigurable PRS

PRS configuration	H-pol beam
uniform (all switches OFF)	9.6 GHz, broadside
	10 GHz, conical 19°
HG-1	9.9-11.3 GHz, asymmetric single 12 to 50°
HG-2	10 GHz, asymmetric single −53°
	10.4 GHz, asymmetric single 23°

tune the cell reflection among the required states: cell A, B, C, and D. A network of DC bias lines control the tuning elements to adjust the phase distribution over the PRS and form the desired beam.

Integrating all PRS cells with MEMS switches results in an orthogonally-polarized independently-controlled dual-band RCA with one broadside beam and one beam which is switched among all possible beam shapes for leaky wave antennas: broadside beam, conical beam, asymmetric single beam scanned with frequency and asymmetric single beam steered at fixed frequency. Table 3.2 summarizes different H-pol beams produced by this RCA. This antenna is a step toward realization of multi-functional apertures.

3.4 Conclusion

This chapter demonstrated the beam shaping capabilities of RCA as a platform for future multi-functional aperture antennas. A MEMS-tunable RCA was designed, fabricated and measured with an upper band vertically polarized broadside beam and a lower band horizontally polarized beam which is switched among all possible beam shapes of leaky wave antennas, i.e., broadside, symmetric conical, and also an asymmetric single beam which is either frequency-scanned or steered at fixed frequency.

Traditionally, a Full Phase-Gradient (FPG) Partially Reflective Surface (PRS) has been used in an RCA for generating off broadside beams. A FPG-PRS is a non-uniform aperture where a continuous phase gradient is applied between adjacent cells in the whole PRS. In this chapter, the novel configuration of Half Phase-Gradient (HPG) PRS was offered where the phase gradient is applied between adjacent cells in half of PRS in order to utilize the inherent leaky wave phase progress inside the antenna. The advantages of HPG-PRS over FPG-PRS such as faster real-time tracking and enhanced scan profile were discussed in detail.

Furthermore, a novel model was extracted for calculating the radiation of such RCAs with non-uniform aperture and verified by comparison with measurements. This model could be applied to any leaky wave antenna with arbitrary unit cell shape and periodicity. Finally, the tunable PRS unit cell required for the beam shaping RCA was realized using hybrid-integrated MEMS switches.

Chapter 4

MEMS-tunable Reflective Cell

Tunable reflectarrays provide a high-performance antenna platform for emerging applications such as cognitive and software-defined radio, LTE-A [76] and mobile satellite connectivity [45–47,77]. These applications require low-cost antennas with steerable beams at different bands and polarizations for diversity/multiplexing purposes. In cognitive radio, these antennas facilitate communication in one band while sensing the space or the remaining spectrum in the other band.

A reflectarray panel includes an array of patches printed on a dielectric laminate backed by a ground plane, and fed by a horn antenna [78]. Reflectarray beam steering is facilitated by manipulation of reflected phase across the panel. Previously, slotted patches have been studied as the reflective cell where the patch size is constant and the slot size varies over the reflectarray panel to realize the required reflected phase [15]. The slot loading can be implemented either on the patch [48] or on the ground plane [58]. The tuning-elements can be integrated into the slot to dynamically control the reflection phase and allow beam-steering [55–57].

Before designing a tunable reflectarray, the technology, the type of tuning element, and the integration method needs to be picked. MEMS and solid-state are two common technologies for realizing tuning elements. However, MEMS is preferred since solid-state tuning suffers from reduced gain due to diode loss, non-linear effects, and also difficulties in high frequency design due to package parasitics [49–52]. For MEMS tuning, switches and varactors have been used for digital [13, 54] and continuous control respectively [53]. In present design, switches are picked since varactors suffer from mechanical instability and un-repeatable reflected phase characteristics. The MEMS switches can be either monolithic or hybrid integrated with cells. However, hybrid technique requires wirebonds which should be modeled as ex-

Table 4.1. Comparison of the proposed design with other digitally MEMS tuned reflective cells in literature.

Design	integration	laminates	metal layers	phase states
Bayraktar	monolithic	2	3	2
Carrasco	hybrid	3	3	4
Proposed design	monolithic	1	1	4

tra parasitic elements in the design. Besides, wirebonding and handling tiny MEMS dies adds a substantial amount of work for implementing large arrays. Hence, monolithic MEMS switches are adopted here.

In most of the reported MEMS-tunable cells, either frozen-state MEMS are used which do not require bias network [79–81] or commercially available MEMS is utilized [13]. Only few designs embody tunable cells with biased and operating in-house-developed MEMS switches [82, 83]. Current state of literature suggests no tunable single-layer cell for generating two independently-controlled beams of different frequency with orthogonal-linear polarization. This chapter presents the design and analysis of an operational MEMS-tunable single-layer reflective unit cell with DC bias network for Ku-band two-way satellite connectivity along with the in-house-developed monolithic fabrication process. This cell provides 4 phase states with overall phase swing of 200° and 180° and average reflection amplitude of −0.79 and −0.69 dB in the lower and the upper bands respectively. This low-loss single-layer structure is much simpler than the designs by Bayraktar [82] and Carrasco [83] which provide 2 and 4 phase states respectively. Table 4.1 compares present design with these two works. The 4 phase states of the proposed is a good compromise between bias network simplicity and beam pointing accuracy [84].

4.1 Antenna Design

This section is a step-by-step procedure to find the optimum cell and array structure. First, different design issues are addressed. Then the cell is designed and an architecture is proposed for the reflectarray antenna panel based on application requirements.

4.1.1 Design Issues

The tuning range and return loss performance are the basic criteria to assess a reflective cell. There are several factors that can affect and deteriorate the cell

performance.

Slot Position

Having the slots in the ground plane allows the undesired leakage of power to the back of reflectarray panel. Such structures usually require more than one layer of metallization. To keep the structure simple, the slotted patch configuration is adopted.

Bias Lines

For slotted patch reflective cells, the tuning elements and the biasing lines have to be implemented on the top face. The bias lines on the radiating aperture are exposed to the incident wave and can affect the reflection depending on their conductivity and layout. Hence, these lines should be made out of a highly resistive material such as doped Poly-Silicon [32, 38] or Graphite paint [60] which are transparent to the wave but conduct the DC voltage with an extremely low current. Conductive lines can completely disrupt the reflection phase and severely decrease the reflection amplitude. In design of the monolithic fabrication process, a highly resistive material which is compatible with other layers should be picked for bias lines.

4.1.2 Unit Cell Design

The proposed reflective unit cell consists of a rectangular patch loaded with cross slots (Fig. 4.1). The unit cell parameters are optimized to P (periodicity) $= 9.525$ mm, $L1$ (patch length) $= 5.5$ mm, $L2$ (patch width) $= 4.5$ mm, $l1$ (first slot length) $= 5.4$ mm, $l2$ (second slot length) $= 4.4$ mm, $w1$ (first slot width) $= 0.2$ mm, $w2$ (second slot width) $= 0.2$ mm in order to have operating frequency of 12 GHz and 14 GHz required for Ku-band satellite communication. The cell is fabricated over Quartz wafer with relative dielectric constant (ε_r) of 3.81, $\tan \delta$ of 0.0004 and thickness of 1.1 mm. In order to achieve the required phase swing at each band and polarization, the effective length of each slot has to be controlled independently. Six symmetric switches across each slot control the slot effective length at both linear polarizations (Fig. 4.2). The position of switches are optimized to $U11 = 1$ mm, $U12 = 1.4$ mm, $U13 = 1.7$ mm, $U21 = 1$ mm, $U22 = 1.5$ mm, and $U23 = 1.8$ mm for maximizing the available phase swing in each polarization. The blue and black switches control H-pol and V-pol respectively. Table 4.2 summarizes these switch
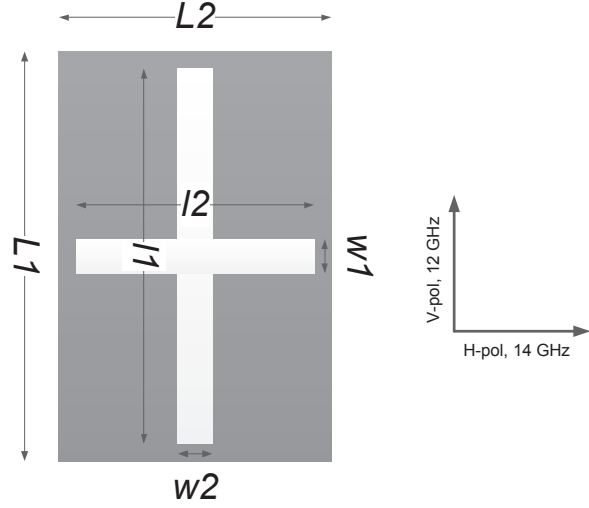
Figure 4.1. Double slotted patch and the design parameters.
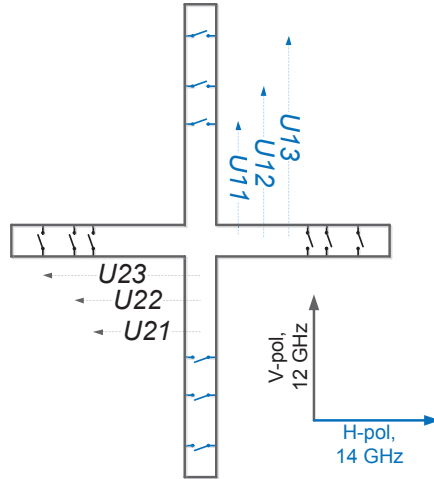
Figure 4.2. Configuration of the switches across the slots.

configurations and their corresponding slot lengths.

4.1.3 Platform Architecture

Fig. 4.3 depicts a platform architecture for the antennas serving above-mentioned applications. The reflectarray panel is composed of tunable orthogonally-polarized independent dual-band unit cells. Two horn antennas illuminate the panel at the lower band with vertical polarization $(f_1, V - pol)$ and at the upper band with horizontal polarization $(f_2, H - pol)$ respectively. Depending on distribution of phase across the panel, the reflectarray steers its beams toward (θ_1, ϕ_1) and (θ_2, ϕ_2) [85].

Table 4.2. Different states of switches used in reflective cell.

switch state	equivalent $l1$	equivalent $l2$
000-000	5.4 mm	4.4 mm
100-001	3.6 mm	3.4 mm
110-011	3 mm	2.8 mm
111-111	2 mm	2 mm

$$(f_2, H-pol, \theta_2, \varphi_2)$$

$$(f_1, V-pol, \theta_1, \varphi_1)$$
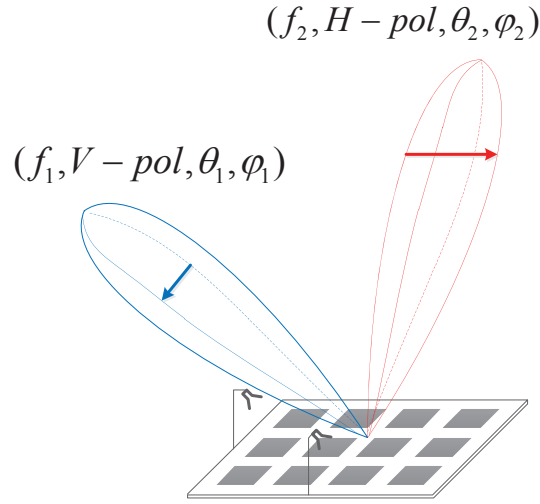
Figure 4.3. A reflectarray with dual independent beams.

4.2 Unit Cell Dynamic Tuning

The design procedure of the MEMS-tunable reflective cell is as follows: First, the custom monolithic fabrication process is presented and the stand-alone MEMS switch is characterized. Then, the simulation models are verified against the measurement results of the reflective unit cells with Metal Insulator Metal (MIM) capacitors. The MIM capacitors play the role of MEMS switches frozen in ON/OFF states. Finally, the tuning of cells with operating RF-MEMS switches are tested inside a custom waveguide setup.

4.2.1 Fabrication Process

The monolithic fabrication process of the MEMS-tunable reflective cell is developed in University of Alberta Nanofab facility with 5 masks and 6 layers. Layer 1 is a 80 nm thick and 10 μm wide reactively sputtered Tantalum Nitride (TaN) layer forming DC bias lines of resistivity 1.6×10^5 Ω/Sq. A magnetron sputtered 10/150/10 nm Cr/Gold/TiW forms switch bottom plates at layer 2. TiW is a 20/80% alloy of Titanium and Tungsten used as the adhesion between the Quartz wafer and Gold

layer. Chromium (Cr) also acts as the adhesion between the Gold layer and the Nitride layer on top. Layer 3 is a 400 nm plasma enhanced chemical vapor deposition Silicon Nitride which insulates switch top and bottom plates. Layer 4 and 5 are the dual-resist sacrificial layers made of LOR5B and HPR504 which are patterned by same mask. Then, a 30/100 nm Cr/Gold layer is magnetron-sputtered as the seed for electroplating of a 1.4 um Gold layer. The cells are diced and then released in a combination of dry and wet steps. Finally, the samples are dried in a Critical Point Drier (CPD) by Carbon Dioxide to avoid stiction of the switch top free beam to the Silicon Nitride layer.

This process facilitates bridging of bias lines over each other using top Gold layer which is vital for realization of large reflectarray panels with full DC bias control network.

4.2.2 Characterization of MEMS Switches

The cross section of a released capacitive MEMS switch is depicted in Fig. 4.4(a). Since MEMS switches integrated with the antenna can not be characterized, stand-alone switches with coplanar waveguide ports are fabricated and tested (Fig. 4.4(b)). The switch pull-down voltage is 80 V and its $|S21|$ is depicted at Fig. 4.4(c). The switch isolation is 16.7 and 15.4 dB at 12 and 14 GHz respectively. Also, the insertion loss is 0.5 and 0.39 dB at 12 and 14 GHz respectively.
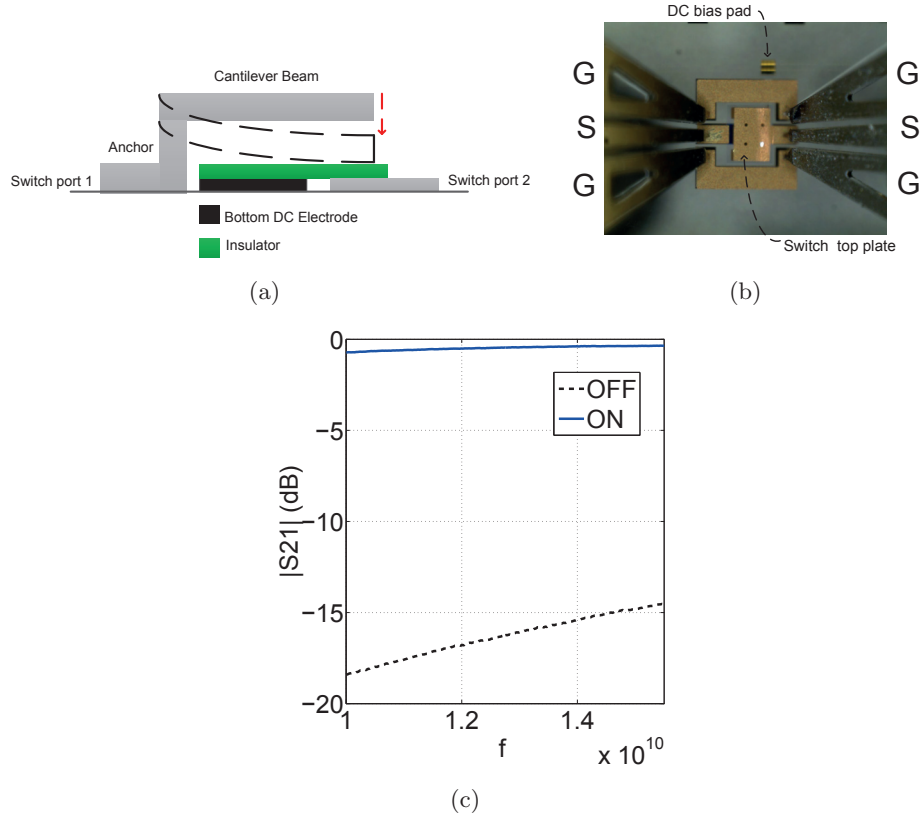
Figure 4.4. (a) Cross-section of a capacitive MEMS switch. (b) Standalone MEMS switch with coplanar waveguide port. (b) $|S21|$ of the MEMS switch in ON/OFF state.

4.2.3 Unit Cell Integrated with MIM Capacitor

After release and CPD steps, the beams of some of MEMS switches may curl up or down depending on their internal residual stress. This leads to an unexpected beam profile and unknown equivalent switch capacitance. Hence, several unit cells are fabricated with frozen MEMS switches, in order to be able to compare simulated and measured results. A frozen MEMS switch is a Metal Insulator Metal (MIM) capacitor composed of 3 layers including the bottom metal plate (Gold1) insulated by a Silicon Nitride layer from the fixed top plate (Gold2). The fabricated MIM capacitors across the slot in UP and DOWN states are depicted in Fig. 4.5(a) and 4.5(b) respectively. In simulation model, the MEMS switches are represented by a lump resistor and capacitor in series (Fig. 4.5(c)). The extracted lump element values are summarized in Table 4.3.

A WR75 waveguide setup is designed for measurement of unit cell reflection. The setup includes a metal base with a rectangular groove which can hold the unit cell (Fig. 4.6(a)). A WR75 waveguide with 4 separate DC pins are used for

illuminating the cell with dominant TE10 mode (Fig. 4.6(b), Fig. 4.6(c)). However, for the unit cells integrated with MIM capacitors, DC pins are not needed to be biased. Fig. 4.7(a) and 4.7(b) compare the simulated and measured reflection phase and amplitude from a unit cell illuminated by a V-pol incident wave with all frozen switches in either UP or DOWN state (MIM capacitors in either OFF or ON state). These two configurations of MIM capacitors are equivalent to 000-000 and 111-111 switch states which are described in Table 4.2. Fig. 4.8(a) and 4.8(b) compare the simulated and measured reflection phase and amplitude from a unit cell illuminated by a H-pol incident wave with all frozen switches in either UP or DOWN state. The simulated and measured results are in good agreement.
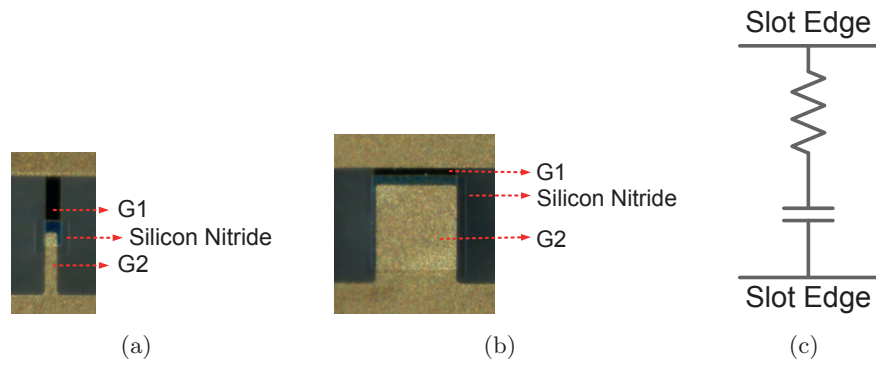
Figure 4.5. (a) Fabricated MIM capacitor across the slot in UP state. (b) Fabricated MIM capacitor across the slot in DOWN state. (c) Lump RC circuit across the slot used for simulation.

Table 4.3. Extracted equivalent lump elements for the MEMS switches used in the simulation model.

pol	r(On) Ω	C(On) pF	r(Off) Ω	C(Off) pF
V	0.7	3.2	2.5	0.11
H	0.7	3.7	4	0.12
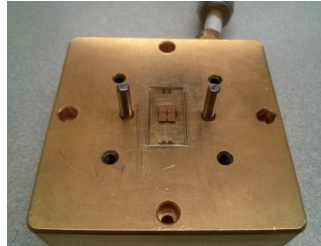
(a)

(b)
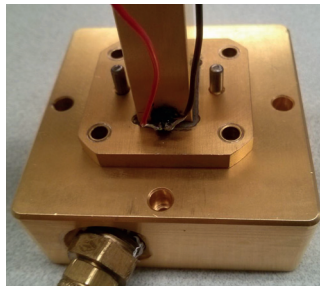
(c)
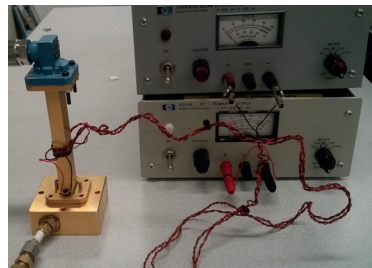
(d)

Figure 4.6. (a) The metal base with groove to house the unit cell. (b) WR75 waveguide with 4 DC bias pins. (c) The DC pins routed out of waveguide wall. (d) The setup with DC bias sources.
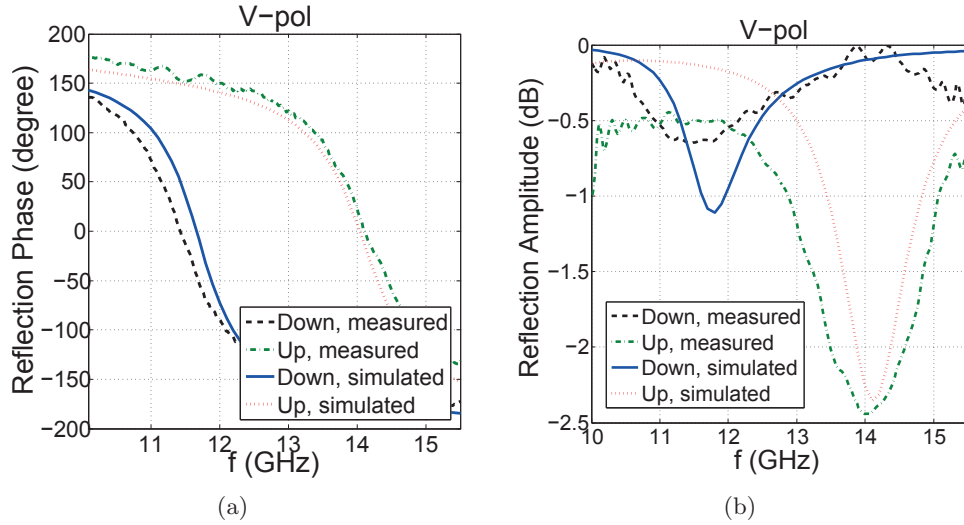
Figure 4.7. Comparison of simulated and measured reflection of unit cells with MIM capacitors illuminated at V-pol. (a) reflection phase; (b) reflection amplitude.
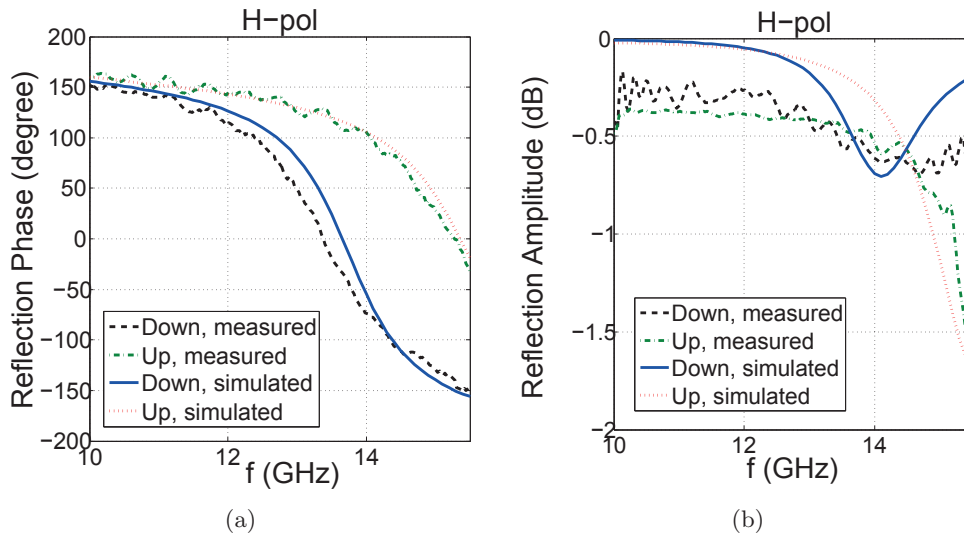
Figure 4.8. Comparison of simulated and measured reflection of unit cells with MIM capacitors illuminated at H-pol. (a) reflection phase; (b) reflection amplitude.

4.2.4 Unit Cell Integrated with MEMS Capacitive Switches

Fig. 4.9(a) demonstrates the unit cell with 4 DC pads around the edges of the cell in order to control the voltage of the patch and also the 3 pairs of switches independently. The fabricated patch is shown in Fig. 4.9(b). Fig. 4.9(c) depicts a single capacitive MEMS switch across the slot. In order to observe the bottom plate of switch and the DC actuation pad, the top plate of switch is pushed back in Fig. 4.9(d). To measure the tuning of unit cell reflection by MEMS switches, the WR75 waveguide

setup is used. To bias each MEMS switch individually, each DC pin sits on its DC pad and is connected to a separate DC source (Fig. 4.6(c),Fig. 4.6(d)). At each polarization of the incident wave, V-pol and H-pol switches are actuated and the reflection is measured.

(a) (b)

(c) (d)
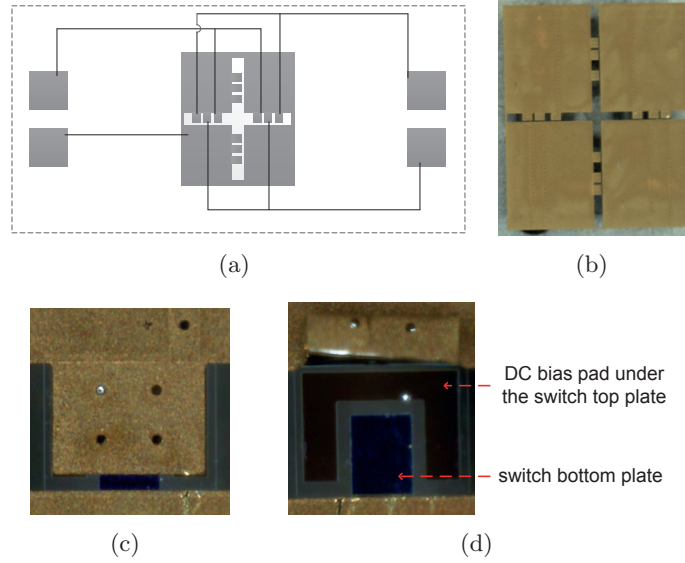
Figure 4.9. (a) The tunable patch with DC pads and bias lines. (b) The fabricated patch. (c) A MEMS switch across the slot. (d) A MEMS switch without top plate.

V-pol/lower-band

Fig. 4.10(a) demonstrates the reflection phase of the cell for different V-pol switch configurations. At the center frequency of 12 GHz, a total phase swing of 200° is achieved with 4 digital phase states. The reflection amplitude is higher than -1.25 dB for all states at the center frequency (Fig. 4.10(b)). In order to verify the independence of the operating band/polarizations, the V-pol reflection is inspected with different asymmetric configurations of H-pol switches. Fig. 4.11(a) shows that V-pol reflection phase changes less than 10° for any configuration of H-pol switches. Besides, Fig. 4.11(b) shows that V-pol reflection amplitude varies less than 0.5 dB for any configuration of H-pol switches.

91
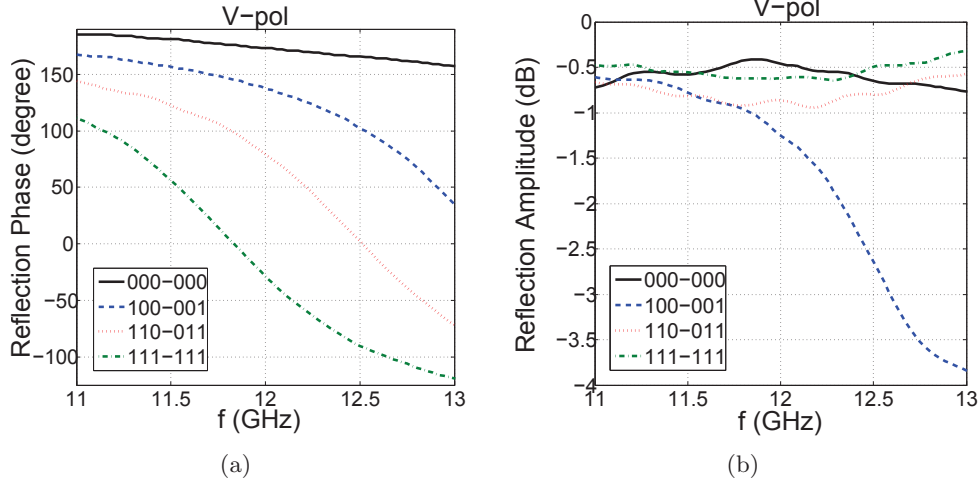
Figure 4.10. Tuning of unit cell illuminated at V-pol by V-pol switches. (a) reflection phase; (b) reflection amplitude.
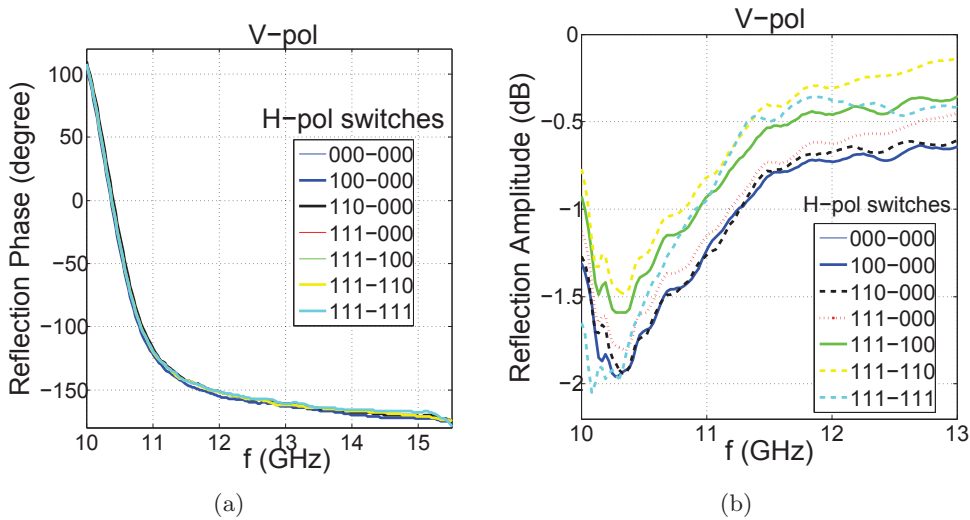
Figure 4.11. Unit cell illuminated at V-pol by H-pol switches. (a) reflection phase; (b) reflection amplitude.

H-pol/upper-band

Fig. 4.12(a) demonstrates the reflection phase of the unit cell for different switch configurations. At the center frequency of 14 GHz, a total phase swing of 180° is achieved with 4 digital phase states. The reflection amplitude is higher than −1.1 dB for all states at the center frequency (Fig. 4.12(b)). In order to verify the independence of the operating band/polarizations, the H-pol reflection is inspected with different asymmetric configurations of V-pol switches. Fig. 4.13(a) shows that H-pol reflection phase varies less than 5° for any configuration of V-pol switches.

Besides, Fig. 4.13(b) shows that H-pol reflection amplitude varies less than 0.4 dB for any configuration of V-pol switches.
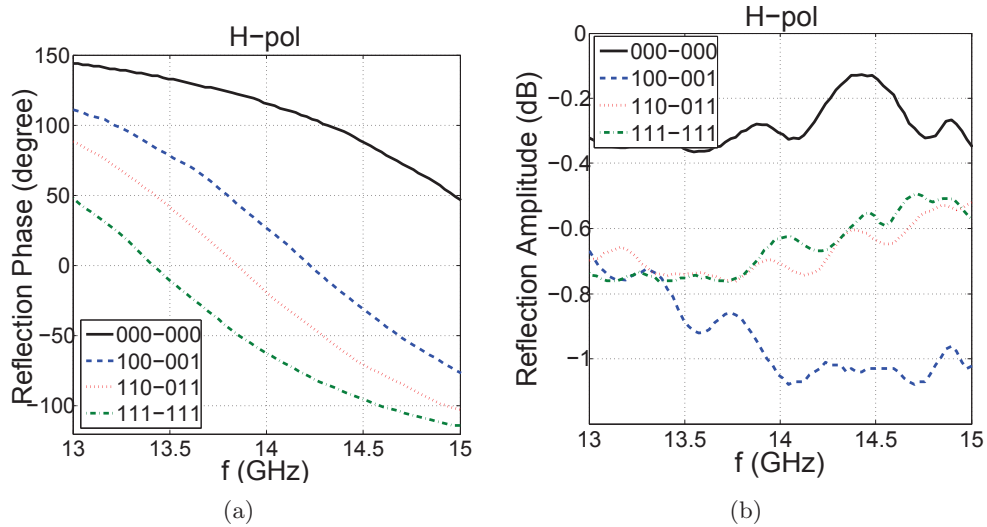
Figure 4.12. Tuning of unit cell illuminated at H-pol by H-pol switches. (a) reflection phase; (b) reflection amplitude.
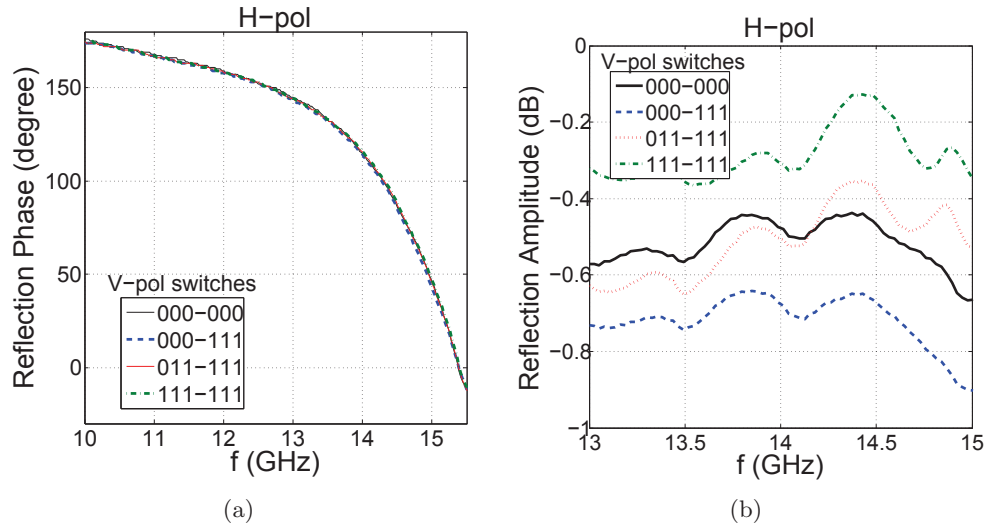
Figure 4.13. Unit cell illuminated at H-pol by V-pol switches. (a) reflection phase; (b) reflection amplitude.

4.3   Conclusion

This chapter demonstrated the potentials of tunable reflectarray as a low cost high performance platform for aperture antennas required in applications such as mobile two way satellite connectivity, software defined and cognitive radio, and next gener-

ation of mobile networks (5G). An orthogonally polarized dual band MEMS-tunable reflectarray cell was designed, fabricated and measured inside a waveguide setup. The unit cell was a cross-slotted patch with 6 capacitive MEMS switches across each slot in order to tune each band independently. A novel monolithic fabrication process was also developed. The waveguide setup included 4 separate DC bias pins which were routed out of waveguide walls and connected to DC sources in order to control the 6 operating capacitive MEMS switches independently. This single layer low loss unit cell provided 4 digital phase states in each band. These 4 phase states are a good compromise between bias network simplicity and beam pointing accuracy. This unit cell can be used as the building block for a reflectarray with two independent beams of orthogonal linear polarizations, different frequency and desired shape. The simulation model was verified by comparison with measurements.

Chapter 5

Future Works and Concluding Remarks

5.1 Concluding Remarks

The major contributions of present thesis are gathered together in this chapter. This thesis develops MEMS-tunable orthogonally polarized dual band aperture antennas - RCA and reflectarray - as platforms for future smart multi-functional aperture antennas. These antennas should be low-profile, low-cost and easily fabricated. Besides, they should be orthogonally-polarized independently-tunable dual-band and beam-steerable. Each chapter is a step forward to develop an antenna prototype which is fully compatible with the mentioned physical and technical requirements.

Chapter 2 describes the design procedure for a dual-band RCA based on ray tracing technique. This chapter includes two different high-gain dual-broadside-beam RCA designs; the first one has a dual-layer and the second one has a single-layer PRS. A microstrip patch antenna is also designed as the cavity feed for simultaneous reception and transmission in the upper and lower bands. This feed system is utilized in all chapters for feeding RCA.

In the first design, we offer a PRS with two single-sided dipole array layers. The polarization of each band is orthogonal to the other. Because of their unique shape, dipoles are not able to operate in dual bands and polarizations. This requires two single-sided dipole layers to cover for both bands. In order to make the RCA structure simpler, we have to think of a PRS unit cell which is dual-band in order to cover both bands with one single-sided PRS layer. Besides, the unit cell has to be able to house the tuning elements for tuning and beam steering.

Slotted patches can house the tuning elements across their slot. As the second

design, Chapter 2 offers a slotted square patch as the PRS unit cell. Although slotted patches are widely used as reflectarray cells, they are new as PRS cells. This unit cell supports two orthogonally-polarized bands where the square forms one resonant frequency and the slot forms the other.

For both designs, it was shown that the two resonant frequencies are arbitrarily and independently controlled. Hence, these structure have the potential to be used in different commercial bands. Also, in order to make the design procedure easier, a design flow-chart with several examples are also provided.

An equivalent transmission line models simply explain the operation of complicated electromagnetic structures. With this motivation in mind, for each polarization, the transmission line model is extracted. The model shows how the independence of the operating bands originates from orthogonality of their polarizations.

Next, the beam-steering capacity of slotted-patch PRS was verified. In order to realize RCA with beams off-broadside, PRS with non-uniform-phase cells should be used. The variation in slot length causes the gradient in phase across PRS. This method was applied to slotted-patch PRS unit cell to realize an RCA with one horizontally-polarized broadside beam and one vertically-polarized beam steered up to 29° depending on the total phase variation across PRS.

Chapter 3 used the slotted-patch PRS unit cell, focusing on RCA beam-shaping with two targets: realizing a tunable PRS unit cell and improving RCA beam-steering. For dynamic beam-steering, tuning elements should be installed in PRS unit cells.

RF-MEMS switches are hybrid-integrated with the slotted patch for tuning its phase. The RF-MEMS switches are fabricated based on a custom process, wire-bonded to the unit cell and then finally measured in a waveguide setup.

For RCA beam-steering, Chapter 2 applied the phase gradient across all PRS cells to implement a Full-Phase-Gradient (FPG) PRS. However, Chapter 3 inspects this radiation mechanism and proposes a novel method for beam-steering. Opposed to the FPG-PRS, the phase gradient is applied only to half of PRS cells. This method was used both for beam-scanning which occurs across frequency and also beam-steering which occurs at fixed frequency. The Half Phase-Gradient (HPG) PRS was compared in detail with traditional FPG-PRS and shown to offer an enhanced scan profile, faster tracking, and also lower DC power consumption which are critical for wireless, space and military applications.

In order to gain a deeper understanding of the radiation phenomena in RCA with non-uniform PRS such as FPG or HPG-PRS, a radiation model is required. The current literature lacks a model that can be applied to non-uniform PRS. Chapter 3 proposes a radiation model for calculation of the radiation pattern for non-uniform apertures. In this model, the PRS unit cells are considered as elements of an array which are excited from underneath by the leaky wave propagating inside the cavity. In order to calculate the PRS array factor, the radiating amplitude and phase of each PRS unit cell has to be found. The wave emanated from the source experiences a phase progress and also an amplitude attenuation inside the antenna structure and then leaks out to radiate. The radiating amplitude and phase of a PRS cell depends on its impedance parameters and the complex propagation constant of RCA unit cells situated between the source and the cell. To verify this model, it was applied to the novel half phase gradient structure and the calculated patterns are compared to the measurements. This model calculates the scan angle and the main-lobe beam-width within $5°$.

Finally, Chapter 3 explains the realization of a MEMS-tunable hybrid-integrated PRS unit cell which is required for implementing the phase-gradient PRS. Using this cell, a beam-shaping RCA is designed with an independent vertically-polarized broadside beam and a horizontally-polarized beam which is switched among all possible beam-forms of leaky-wave antenna depending on PRS configuration which is adjusted by MEMS switches and the operating frequency; i.e. a broadside beam, a symmetric conical beam, a frequency-scanned asymmetric single beam and also an asymmetric single beam which is steered at fixed frequency.

Chapter 4 studies the potentials of reflectarrays as orthogonally-polarized dual-band beam-steering antennas. First, a phase-tunable low-loss double-slotted patch reflective unit cell is designed and simulated for operation at 12 GHz with vertical polarization and 14 GHz with horizontal polarization for Ku-band mobile satellite communication. The phase tuning is facilitated using an array of switches across both slots in order to dynamically control the equivalent slot length. A monolithic custom fabrication process is developed for fabrication of the proposed reflectarray unit cell with MEMS switches. Then, these unit cells are measured inside a waveguide setup with DC bias pads to verify the phase tuning.

5.2 Future Work

This section discusses future work that can be conducted with reflectarray and RCA with the purpose of improved designs.

Monolithic-Integrated MEMS-tunable PRS unit cell

In chapter 3, a hybrid-integrated MEMS-tunable slotted patch PRS was fabricated and measured. Also, a monolithic fabrication process was developed in Chapter 4 for the reflective unit cells. Same monolithic fabrication process can be adopted to realize tunable PRS unit cells in order to avoid wirebonding.

Synthesis of Non-Uniform PRS for Beam-Scanning

In chapter 3, an equivalent model was proposed and verified for analysis of radiation phenomenon in non-uniform PRS based on array theory and impedance parameters. The proposed formulation is used to find the scan angle if the PRS phase distribution is known. This formulation can be used in reverse way for synthesizing the required PRS phase distribution to achieve the desired scan angle.

Tunable RCA Feed

Chapter 2 proposes a microstrip patch antenna which is fed by two microstrip lines for feeding the cavity at two orthogonally-polarized bands. For a beam-steering or tunable PRS where the PRS changes, the feed should also be modified in order to avoid gain drop. Hence, to have maximum gain possible, tuning elements should also be installed in the feed to control its operating frequency.

Wide-Band RCA Feed

Another method to compensate for the change in PRS is to use a feed system which is wide-band and covers the whole PRS operating range. Regular narrow-band microstrip patches can be substituted by stacked patches to increase feed bandwidth.

Applying the Radiation Model to Other Leaky-Wave Antennas

In order to prove the abilities of the radiation model extracted for non-uniform leaky-wave antennas, the extracted formulas can be applied to different structures

such as holographic, periodically-modulated, or tapered surfaces to calculate the radiation pattern and compare it with simulated and measured results.

Bibliography

[1] (2013, May) car image used in the figure. [Online]. Available: http://lerablog.org/business/automotive/car-safety-tips-for-the-summer-season/

[2] C. A. Balanis, *Antenna theory and design.* John Wiley & Sons, Inc, 1997.

[3] D. F. Sievenpiper, "Steerable leaky wave antenna capable of both forward and backward radiation," Jul. 4 2006, uS Patent 7,071,888.

[4] C. S. Lee and V. Nalbandian, "Wideband planar leaky-wave microstrip antenna," Dec. 21 1999, uS Patent 6,005,520.

[5] R. Collin, "Analytical solution for a leaky-wave antenna," *Antennas and Propagation, IRE Transactions on*, vol. 10, no. 5, pp. 561–565, 1962.

[6] T. Zhao, D. Jackson, J. Williams, H.-Y. Yang, and A. Oliner, "2-d periodic leaky-wave antennas-part i: metal patch design," *Antennas and Propagation, IEEE Transactions on*, vol. 53, no. 11, pp. 3505–3514, 2005.

[7] T. Zhao, D. Jackson, and J. Williams, "2-d periodic leaky-wave antennas-part ii: slot design," *Antennas and Propagation, IEEE Transactions on*, vol. 53, no. 11, pp. 3515–3524, 2005.

[8] M. Guglielmi and G. Boccalone, "A novel theory for dielectric-inset waveguide leaky-wave antennas," *Antennas and Propagation, IEEE Transactions on*, vol. 39, no. 4, pp. 497–504, 1991.

[9] S. K. Podilchak, A. P. Freundorfer, and Y. Antar, "Planar leaky-wave antenna designs offering conical-sector beam scanning and broadside radiation using surface-wave launchers," *Antennas and Wireless Propagation Letters, IEEE*, vol. 7, pp. 155–158, 2008.

[10] S. F. Mahmoud, S. K. Podilchak, Y. M. Antar, and A. P. Freundorfer, "Perturbation analysis of a planar periodic leaky-wave antenna fed by surface waves," *Antennas and Wireless Propagation Letters, IEEE*, vol. 10, pp. 174–178, 2011.

[11] A. Jacomb-Hood, A. Katz, G. J. Matyas, G. A. Silverman, W. J. SooHoo, and W. J. Taft, "Mems reflectarray antenna for satellite applications," Apr. 18 2006, uS Patent 7,030,824.

[12] F. A. Miranda and R. R. Romanofsky, "High resolution scanning reflectarray antenna," Jun. 27 2000, uS Patent 6,081,235.

[13] H. Rajagopalan, Y. Rahmat-Samii, and W. Imbriale, "Rf mems actuated reconfigurable reflectarray patch-slot element," *Antennas and Propagation, IEEE Transactions on*, vol. 56, no. 12, pp. 3689–3699, 2008.

[14] Y. C. Wei *et al.*, "Proximity-coupled microstrip reflectarray," *Antennas and Propagation, IEEE Transactions on*, vol. 52, no. 2, pp. 631–635, 2004.

[15] D. Cadoret, A. Laisné, R. Gillard, L. Le Coq, and H. Legay, "Design and measurement of new reflectarray antenna using microstrip patches loaded with slot," *Electronics Letters*, vol. 41, no. 11, pp. 623–624, 2005.

[16] D. Jackson and N. Alexopoulos, "Gain enhancement methods for printed circuit antennas," *Antennas and Propagation, IEEE Transactions on*, vol. 33, no. 9, pp. 976–987, 1985.

[17] G. Trentini, "Partially reflecting sheet arrays," *Antennas and Propagation, IRE Transactions on*, vol. 4, no. 4, pp. 666–671, 1956.

[18] C. Cheype, C. Serier, M. Thevenot, T. Monediere, A. Reineix, and B. Jecko, "An electromagnetic bandgap resonator antenna," *Antennas and Propagation, IEEE Transactions on*, vol. 50, no. 9, pp. 1285–1290, 2002.

[19] M. Thevenot, C. Cheype, A. Reineix, and B. Jecko, "Directive photonic-bandgap antennas," *Microwave Theory and Techniques, IEEE Transactions on*, vol. 47, no. 11, pp. 2115–2122, 1999.

[20] H. Boutayeb, K. Mahdjoubi, A.-C. Tarot, and T. A. Denidni, "Directivity of an antenna embedded inside a fabryperot cavity: Analysis and design," *Microwave and Optical Technology Letters*, vol. 48, no. 1, pp. 12–17, 2006. [Online]. Available: http://dx.doi.org/10.1002/mop.21249

[21] R. Gardelli, M. Albani, and F. Capolino, "Array thinning by using antennas in a fabry-perot cavity for gain enhancement," *Antennas and Propagation, IEEE Transactions on*, vol. 54, no. 7, pp. 1979–1990, 2006.

[22] A. Kanso, R. Chantalat, M. Thevenot, E. Arnaud, and T. Monediere, "Offset parabolic reflector antenna fed by ebg dual-band focal feed for space application," *Antennas and Wireless Propagation Letters, IEEE*, vol. 9, pp. 854–858, 2010.

[23] Z.-B. Weng, Y. Song, Y.-C. Jiao, and F.-S. Zhang, "A directive dual-band and dual-polarized antenna with zero index metamaterial," *Microwave and Optical Technology Letters*, vol. 50, no. 11, pp. 2902–2904, 2008. [Online]. Available: http://dx.doi.org/10.1002/mop.23855

[24] D. Lee, Y. Lee, J. Yeo, R. Mittra, and W. Park, "Design of novel thin frequency selective surface superstrates for dual-band directivity enhancement," *Microwaves, Antennas Propagation, IET*, vol. 1, no. 1, pp. 248–254, 2007.

[25] J. Kelly, G. Passalacqua, A. Feresidis, F. Capolino, M. Albani, and Y. Vardaxoglou, "Dual frequency leaky-wave antenna analysis and design," in *Antennas and Propagation, 2007. EuCAP 2007. The Second European Conference on*, 2007, pp. 1–5.

[26] H. Moghadas, M. Daneshmand, and P. Mousavi, "A dual-band high-gain resonant cavity antenna with orthogonal polarizations," *Antennas and Wireless Propagation Letters, IEEE*, vol. 10, pp. 1220–1223, 2011.

[27] A. Pirhadi, M. Hakkak, F. Keshmiri, and R. Baee, "Design of compact dual band high directive electromagnetic bandgap (ebg) resonator antenna using artificial magnetic conductor," *Antennas and Propagation, IEEE Transactions on*, vol. 55, no. 6, pp. 1682–1690, 2007.

[28] Y. Ge, K. P. Esselle, and T. S. Bird, "Experimental demonstration of a dual-band electromagnetic band-gap resonator antenna made out of a simple, single-layer frequency selective surface," *Microwave and Optical Technology Letters*, vol. 53, no. 8, pp. 1867–1869, 2011. [Online]. Available: http://dx.doi.org/10.1002/mop.26112

[29] E. Ugarte-Muoz, F. Herraiz-Martinez, J. Montero-de Paz, L. Garcia-Muoz, and D. Segovia-Vargas, "Planar superstrate made with meta-material particles for dual-polarized dual-frequency antennas and circularly polarized antennas," in *Antennas and Propagation Society International Symposium (APSURSI), 2010 IEEE*, 2010, pp. 1–4.

[30] B. Zeb, Y. Ge, and K. Esselle, "A new technique to design 1-d dual-band ebg resonator antennas," in *Antennas and Propagation (APSURSI), 2011 IEEE International Symposium on*, 2011, pp. 1804–1807.

[31] M. Hajj, M. S. Toubet, R. Chantalat, T. Monediere, and B. Jecko, "Bipolar dual-band mprs-fss sectoral antenna for base station applications," *Microwave and Optical Technology Letters*, vol. 53, no. 12, pp. 2907–2912, 2011. [Online]. Available: http://dx.doi.org/10.1002/mop.26431

[32] J. Perruisseau-Carrier, "Dual-polarized and polarization-flexible reflective cells with dynamic phase control," *Antennas and Propagation, IEEE Transactions on*, vol. 58, no. 5, pp. 1494–1502, 2010.

[33] A. Ourir, S. Burokur, and A. de Lustrac, "Phase-varying metamaterial for compact steerable directive antenna," *Electronics Letters*, vol. 43, no. 9, pp. 493–494, 2007.

[34] A. Ourir, A. de Lustrac, and J.-M. Lourtioz, "All-metamaterial-based subwavelength cavities (lambda /60) for ultrathin directive antennas," *Applied Physics Letters*, vol. 88, no. 8, pp. 084 103–084 103–3, 2006.

[35] A. Ourir, S. Burokur, and A. De Lustrac, "Steerable ultra-thin directive antenna from a metamaterial-based subwavelength cavity," in *Antenna Technology: Small and Smart Antennas Metamaterials and Applications, 2007. IWAT '07. International Workshop on*, 2007, pp. 19–22.

[36] A. Ourir, S. N. Burokur, R. Yahiaoui, and A. de Lustrac, "Directive metamaterial-based subwavelength resonant cavity antennas–applications for beam steering," *Comptes Rendus Physique*, vol. 10, no. 5, pp. 414–422, 2009.

[37] A. R. Weily, T. S. Bird, and Y. J. Guo, "A reconfigurable high-gain partially reflecting surface antenna," *Antennas and Propagation, IEEE Transactions on*, vol. 56, no. 11, pp. 3382–3390, 2008.

[38] T. Debogovic, J. Bartolic, and J. Perruisseau-Carrier, "Dual-polarized partially reflective surface antenna with mems-based beamwidth reconfiguration," *Antennas and Propagation, IEEE Transactions on*, vol. 62, no. 1, pp. 228–236, Jan 2014.

[39] F. Costa, A. Monorchio, and G. Manara, "Low-profile tunable and steerable fabry-perot antenna for software defined radio applications," in *Antennas and Propagation Society International Symposium (APSURSI), 2010 IEEE*. IEEE, 2010, pp. 1–4.

[40] A. Edalati and T. A. Denidni, "Reconfigurable beamwidth antenna based on active partially reflective surfaces," *Antennas and Wireless Propagation Letters, IEEE*, vol. 8, pp. 1087–1090, 2009.

[41] M. Zawadzki, S. Rengarajan, and R. E. Hodges, "The design of h-and v-pol waveguide slot array feeds for a scanned offset dual-polarized reflectarray," in *Antennas and Propagation Society International Symposium, 2005 IEEE*, vol. 2. IEEE, 2005, pp. 417–420.

[42] A. Abbosh, "Dual-band single layer microstrip reflectarray using multiresonance double cross elements," in *Microwave Conference, 2008. APMC 2008. Asia-Pacific*. IEEE, 2008, pp. 1–4.

[43] P. Pirinoli, P. Cong, M. Mussetta, and M. Orefice, "Concentric square ring elements for dual band reflectarray antenna," in *Antennas and Propagation, 2009. EuCAP 2009. 3rd European Conference on.* IEEE, 2009, pp. 1342–1344.

[44] P. Pirinoli, P. Cong, M. Mussetta, and M. Orefice, "Dual-band reflectarray antenna: Design and experimental validation," in *Electromagnetics in Advanced Applications, 2009. ICEAA'09. International Conference on.* IEEE, 2009, pp. 1024–1027.

[45] H. Moghadas, M. Daneshmand, P. Mousavi, M. R. Chaharmir, and J. Shaker, "Dual-band mems-tunable slotted-cross reflective unit cell with orthogonal polarization," in *Antennas and Propagation Society International Symposium (APSURSI), 2012 IEEE.* IEEE, 2012, pp. 1–2.

[46] D. Oloumi, H. Moghadas, and P. Mousavi, "Dual-band orthogonally-polarized slotted-lozenge reflective unit cell tuned by mems varactor," in *Antennas and Propagation Society International Symposium (APSURSI), 2012 IEEE.* IEEE, 2012, pp. 1–2.

[47] H. Moghadas, M. Daneshmand, P. Mousavi, M. R. Chaharmir, and J. Shaker, "Orthogonally-polarized dual-band mems-tunable double-slotted unit cell for reflectarray applications," in *Antennas and Propagation Society International Symposium (APSURSI), 2012 IEEE.* IEEE, 2012, pp. 1–2.

[48] M. Hajian, B. J. Kuijpers, and L. Ligthart, "Reflectarray design using capacitive loading on a slotted patch," in *Antennas and Propagation, 2006. EuCAP 2006. First European Conference on.* IEEE, 2006, pp. 1–7.

[49] D. F. Sievenpiper, J. H. Schaffner, H. J. Song, R. Y. Loo, and G. Tangonan, "Two-dimensional beam steering using an electrically tunable impedance surface," *Antennas and Propagation, IEEE Transactions on*, vol. 51, no. 10, pp. 2713–2722, 2003.

[50] S. V. Hum, M. Okoniewski, and R. J. Davies, "Realizing an electronically tunable reflectarray using varactor diode-tuned elements," *Microwave and Wireless Components Letters, IEEE*, vol. 15, no. 6, pp. 422–424, 2005.

[51] S. V. Hum, M. Okoniewski, and R. J. Davies, "Modeling and design of electronically tunable reflectarrays," *Antennas and Propagation, IEEE Transactions on*, vol. 55, no. 8, pp. 2200–2210, 2007.

[52] J. Perruisseau-Carrier, F. Bongard, R. Golubovic-Niciforovic, R. Torres-Sánchez, and J. R. Mosig, "Contributions to the modeling and design of reconfigurable reflecting cells embedding discrete control elements," *Microwave Theory and Techniques, IEEE Transactions on*, vol. 58, no. 6, pp. 1621–1628, 2010.

[53] S. V. Hum, G. McFeetors, and M. Okoniewski, "Integrated mems reflectarray elements," in *Antennas and Propagation, 2006. EuCAP 2006. First European Conference on.* IEEE, 2006, pp. 1–6.

[54] H. Salti, E. Fourn, R. Gillard, and H. Legay, "Minimization of mems breakdowns effects on the radiation of a mems based reconfigurable reflectarray," *Antennas and Propagation, IEEE Transactions on*, vol. 58, no. 7, pp. 2281–2287, 2010.

[55] J. Perruisseau-Carrier and A. Georgiadis, "Efficient optimization of the phase diagram in digitally-controlled reflective cells," in *Antennas and Propagation, 2009. EuCAP 2009. 3rd European Conference on.* IEEE, 2009, pp. 1230–1233.

[56] E. Perret, H. Aubert, and H. Legay, "Scale-changing technique for the electromagnetic modeling of mems-controlled planar phase shifters," *Microwave Theory and Techniques, IEEE Transactions on*, vol. 54, no. 9, pp. 3594–3601, 2006.

[57] B. Wu, A. Sutinjo, M. E. Potter, and M. Okoniewski, "Determining an appropriate number of bits for a digitally controlled reflectarray cell with mems switches," in *Antennas and Propagation Society International Symposium, 2008. AP-S 2008. IEEE.*   IEEE, 2008, pp. 1–4.

[58] M. Chaharmir, J. Shaker, M. Cuhaci, and A. Sebak, "Reflectarray with variable slots on ground plane," in *Microwaves, Antennas and Propagation, IEE Proceedings*, vol. 150, no. 6.   IET, 2003, pp. 436–439.

[59] G. M. Rebeiz, *RF MEMS: Theory, Design, and Technology*, 2003.

[60] H. Rajagopalan, J. Kovitz, and Y. Rahmat-Samii, "Frequency reconfigurable wideband e-shaped patch antenna: Design, optimization, and measurements," in *Antennas and Propagation Society International Symposium (APSURSI), 2012 IEEE.*   IEEE, 2012, pp. 1–2.

[61] H. Moghadas, P. Mousavi, M. Daneshmand, and R. Karumudi, "Dual-band dual-polarized high-gain resonant cavity antenna," in *Antennas and Propagation (APSURSI), 2011 IEEE International Symposium on*, 2011, pp. 2246–2249.

[62] H. Moghadas, M. Daneshmand, and P. Mousavi, "Dual-band high-gain resonant cavity antenna with orthogonal polarisation using slotted patch partially reflective superstrate," *Electronics letters*, vol. 48, no. 15, pp. 897–899, 2012.

[63] A. Feresidis and J. Vardaxoglou, "High gain planar antenna using optimised partially reflective surfaces," *Microwaves, Antennas and Propagation, IEE Proceedings*, vol. 148, no. 6, pp. 345–350, 2001.

[64] H. Moghadas, M. Daneshmand, and P. Mousavi, "Half-phase-gradient partially reflective surface for a reconfigurable dual-beam scanning cavity antenna," in *Antennas and Propagation Society International Symposium (APSURSI), 2012 IEEE*, 2012, pp. 1–2.

[65] T. Zhao, D. R. Jackson, J. T. Williams, and A. A. Oliner, "General formulas for 2-d leaky-wave antennas," *Antennas and Propagation, IEEE Transactions on*, vol. 53, no. 11, pp. 3525–3533, 2005.

[66] A. Sutinjo, M. Okoniewski, and R. H. Johnston, "A holographic antenna approach for surface wave control in microstrip antenna applications," *Antennas and Propagation, IEEE Transactions on*, vol. 58, no. 3, pp. 675–682, 2010.

[67] P. Burghignoli, G. Lovat, and D. R. Jackson, "Analysis and optimization of leaky-wave radiation at broadside from a class of 1-d periodic structures," *Antennas and Propagation, IEEE Transactions on*, vol. 54, no. 9, pp. 2593–2604, 2006.

[68] G. Lovat, P. Burghignoli, and D. R. Jackson, "Fundamental properties and optimization of broadside radiation from uniform leaky-wave antennas," *Antennas and Propagation, IEEE Transactions on*, vol. 54, no. 5, pp. 1442–1452, 2006.

[69] Y.-S. Lee, J.-K. Kim, and Y.-K. Cho, "Improved complex images of a magnetic dipole in a parallel-plate waveguide," in *Antennas and Propagation Society International Symposium, 1997. IEEE., 1997 Digest*, vol. 3.   IEEE, 1997, pp. 2088–2091.

[70] R. F. Harrington, *Time-Harmonic Electromagnetic Fields*. IEEE, 2001.

[71] H. Moghadas, M. Daneshmand, and P. Mousavi, "Single-layer partially reflective surface for an orthogonally-polarised dual-band high-gain resonant cavity antenna," *IET Microwaves, Antennas & Propagation*, vol. 7, no. 8, pp. 656–662, 2013.

[72] P. Mousavi, M. Fakharzadeh, S. H. Jamali, K. Narimani, M. Hossu, H. Boland-hemmat, G. Rafi, and S. Safavi-Naeini, "A low-cost ultra low profile phased array system for mobile satellite reception using zero-knowledge beamforming algorithm," *Antennas and Propagation, IEEE Transactions on*, vol. 56, no. 12, pp. 3667–3679, 2008.

[73] M. Fakharzadeh, S. Jamali, S. Safavi-Naeini, P. Mousavi, and K. Narimani, "Fast stochastic beamforming for mobile phased array antennas," in *Antennas and Propagation Society International Symposium, 2007 IEEE*. IEEE, 2007, pp. 1945–1948.

[74] D. Pozar and D. Schaubert, "Scan blindness in infinite phased arrays of printed dipoles," *Antennas and Propagation, IEEE Transactions on*, vol. 32, no. 6, pp. 602–610, 1984.

[75] P. Hannan and M. Balfour, "Simulation of a phased-array antenna in waveguide," *Antennas and Propagation, IEEE Transactions on*, vol. 13, no. 3, pp. 342–353, May 1965.

[76] J. Perruisseau-Carrier, "Versatile reconfiguration of radiation patterns, frequency and polarization: A discussion on the potential of controllable reflectarrays for software-defined and cognitive radio systems," in *RF Front-ends for Software Defined and Cognitive Radio Solutions (IMWS), 2010 IEEE International Microwave Workshop Series on*, 2010, pp. 1–4.

[77] H. Legay, Y. Cailloce, O. Vendier, G. Caille, J. Perruisseau-Carrier, M. Lathi, J. P. Polizzi, U. Oestermann, P. Pons, and N. Raveu, "Satellite antennas based on mems tunable reflectarrays," in *Antennas and Propagation, 2007. EuCAP 2007. The Second European Conference on*. IET, 2007, pp. 1–6.

[78] S. Hum and J. Perruisseau-Carrier, "Reconfigurable reflectarrays and array lenses for dynamic antenna beam control: A review," *Antennas and Propagation, IEEE Transactions on*, vol. 62, no. 1, pp. 183–198, 2014.

[79] J. Perruisseau-Carrier and A. K. Skrivervik, "Monolithic mems-based reflectarray cell digitally reconfigurable over a 360¡ formula¿¡ img src=," *Antennas and Wireless Propagation Letters, IEEE*, vol. 7, pp. 138–141, 2008.

[80] H. Legay, B. Pinte, M. Charrier, A. Ziaei, E. Girard, and R. Gillard, "A steerable reflectarray antenna with mems controls," in *Phased Array Systems and Technology, 2003. IEEE International Symposium on*. IEEE, 2003, pp. 494–499.

[81] C. Guclu, J. Perruisseau-Carrier, and O. Aydin Civi, "Proof of concept of a dual-band circularly-polarized rf mems beam-switching reflectarray," *Antennas and Propagation, IEEE Transactions on*, vol. 60, no. 11, pp. 5451–5455, Nov 2012.

[82] O. Bayraktar, O. A. Civi, and T. Akin, "Beam switching reflectarray monolithically integrated with rf mems switches," *Antennas and Propagation, IEEE Transactions on*, vol. 60, no. 2, pp. 854–862, 2012.

[83] E. Carrasco, M. Barba, B. Reig, C. Dieppedale, and J. A. Encinar, "Characterization of a reflectarray gathered element with electronic control using ohmic rf mems and patches aperture-coupled to a delay line," *Antennas and Propagation, IEEE Transactions on*, vol. 60, no. 9, pp. 4190–4201, Sept 2012.

[84] B. Wu, A. Sutinjo, M. E. Potter, and M. Okoniewski, "On the selection of the number of bits to control a dynamic digital mems reflectarray," *Antennas and Wireless Propagation Letters, IEEE*, vol. 7, pp. 183–186, 2008.

[85] D. F. Sievenpiper, J. H. Schaffner, H. J. Song, R. Y. Loo, and G. Tangonan, "Two-dimensional beam steering using an electrically tunable impedance surface," *Antennas and Propagation, IEEE Transactions on*, vol. 51, no. 10, pp. 2713–2722, 2003.

Appendix A

Fabrication Process

This appendix has two sections. In the first section, the major techniques and tools for fabrication in a cleanroom are explained. The second section presents a detailed instruction of the monolithic fabrication process used for the MEMS-tunable reflectarray unit cells which includes 5 masks which are designed by LEdit software and then printed in Chromium on $5'' \times 5''$ glass.

A.1 Major Techniques Used in Cleanrooms

The common techniques used in fabrication of MEMS devices are as follows.

A.1.1 Optical Lithography

Optical lithography is used to transfer specific patterns printed on glass masks to the photo-resist on the wafer. This technique is performed in an area which is protected from regular light to prevent the unwanted exposure of the photo-resist. Since the photo-resist does not stick well to bare wafer, the bare wafers are covered with a layer of HexaMethylDiSilazane (HMDS) inside HMDS oven before spinning the resist (Figure A.1). Then, the wafer is covered with a several micrometer layer of photo-resist using the spinner (Figure A.2(a) and A.2(b)). Immediately afterwards, the wafer is baked on a hotplate (Figure A.3) and let cool and rehydrate for a while. Then, it is put in direct contact with the photo-mask using a mask aligner and exposed to Ultra-Violet (UV) light for several seconds (Figure A.4(a) and A.4(b)). After the exposure, the photo-resist is developed in its specific developer solution at the wetdeck (Figure A.5). For a positive-tone resist, the developer removes the exposed areas. But for a negative-tone resist, this is vice-versa. Figure A.6 demonstrates the wafer cross-section and the steps taken for lithography. Usually several masks are used in fabrication of a MEMS device. After one layer finishes, the next layer mask has to be aligned with previous layer features. A set of alignment marks are used on the wafer for this purpose.

Figure A.1. YES HMDS oven.
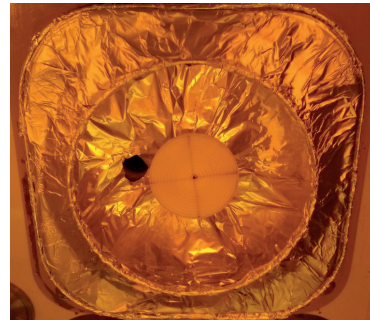
(a)   (b)

Figure A.2. (a) The spinner used for covering the wafer with a layer of resist. (b) The wafer chuck.

Alignment Marks

In order to make sure about the alignment of features belonging to different layers, two symmetric sets of alignment marks are devised on both sides of all masks. Figure A.7 shows all masks on top of each other drawn in LEdit software and the optimum position for placement of alignment marks. Fig. A.8 shows two sets of similar marks. The marks on left are utilized for alignment of mask2 (Gold1) with mask1 (TaN) and mask3 (Nitride). The marks on right are utilized for alignment of mask2 (Gold1) with mask4 (sacrificial layers) and mask5 (Gold2). All layers are
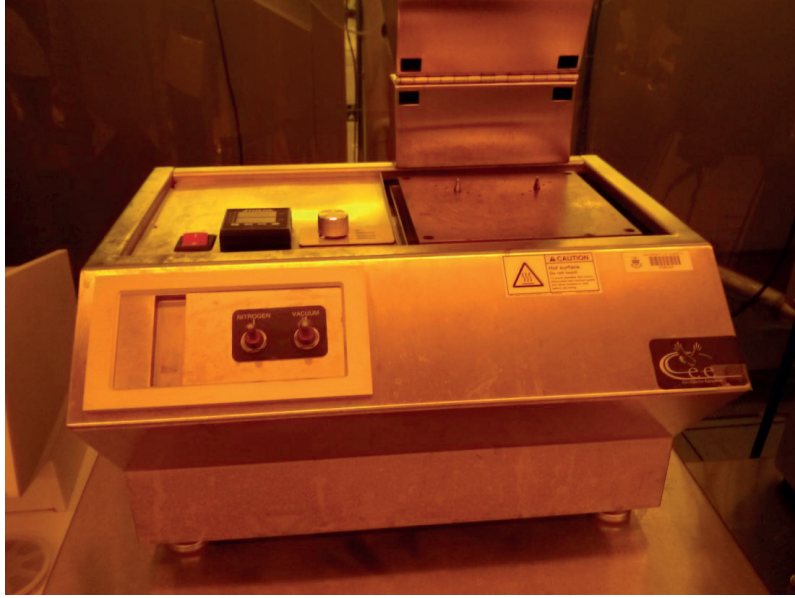
Figure A.3. Hot plate used for baking the photo-resist.

aligned with respect to mask2 (Gold1) since Gold makes a shiny layer which is easily observable under mask aligner lenses. It is possible to have a single set of marks with all layers on top of each other. Here, this is avoided since the accumulation of marks from different layers on top of each other deteriorates the accuracy. The smallest mark used on the mask has a feature size of 1.5 um which ensures the accuracy required for MEMS devices in these experiments. The big marks in the middle are used for alignment with naked eye.

A.1.2 Sputtering

Sputtering is a technique for physical deposition of a very thin film of material on wafer. The target and the wafer are both put in parallel and at a close distance inside a vacuum chamber (Figure A.9). A plasma is formed in chamber by high voltage electric discharge and the target is bombarded by plasma particles. The bombardment ejects the target particles. These particles start depositing on wafer and form a thin film. The Nanofab sputtering tool is demonstrated in Figure A.10(a) and A.10(a).

A.1.3 PECVD

In a Plasma Enhanced Chemical Vapor Deposition (PECVD) process, the gaseous product of a chemical reaction deposits on the wafer in form of a solid film. The wafer is placed inside a vacuum chamber and a plasma is formed by electric discharge from the reacting gas. As an example, for deposition of Silicon-Nitride film, the required gases are Ammonia (NH_3) and Silane (SiH_4). Figure A.11 shows the Trion PECVD tool used in Nanofab facility.
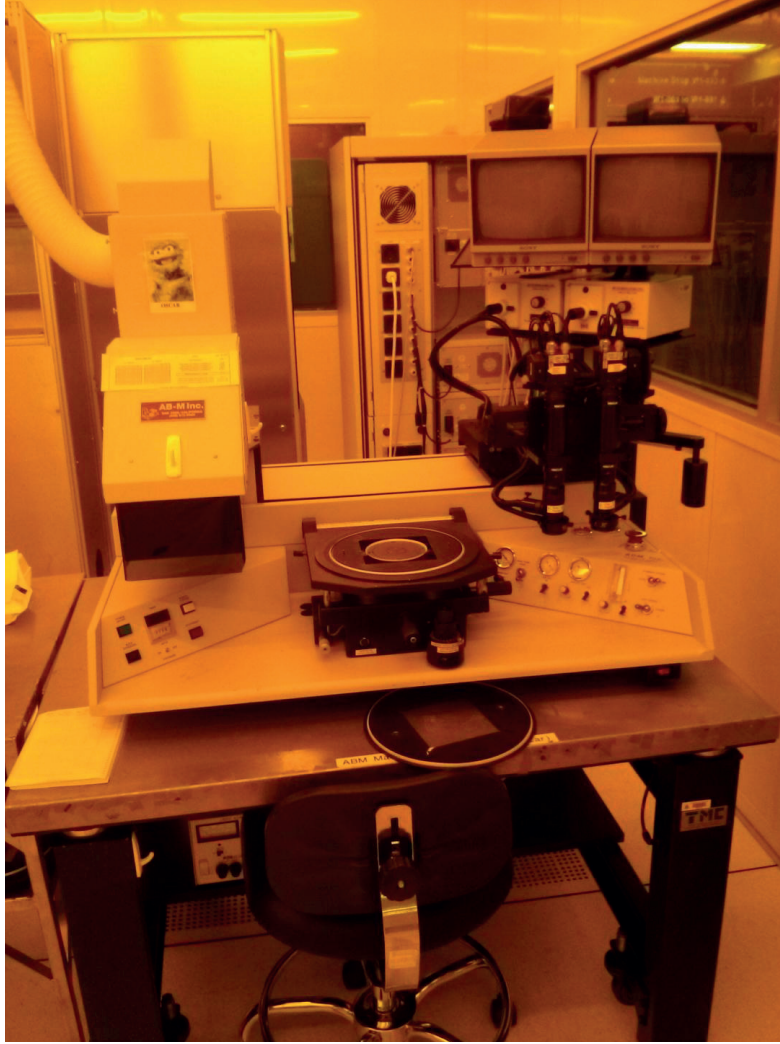
(a)
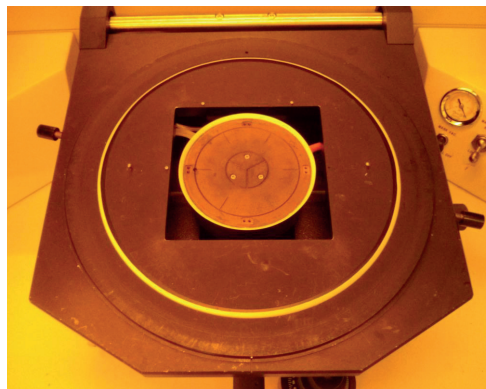
(b)

Figure A.4. (a) ABM mask aligner. (b) The chuck for fixing the wafer.

A.1.4   RIE

In Reactive Ion Etching (RIE), a chemically reactive plasma removes the desired material from the wafer. Plasma particles with high-energy bombard the wafer and

Figure A.5. Wet-deck used for developing the photo-resist.

Covering the wafer with resist

Chromium features that stop
UV exposure on some resist
areas

UV exposure

After developing
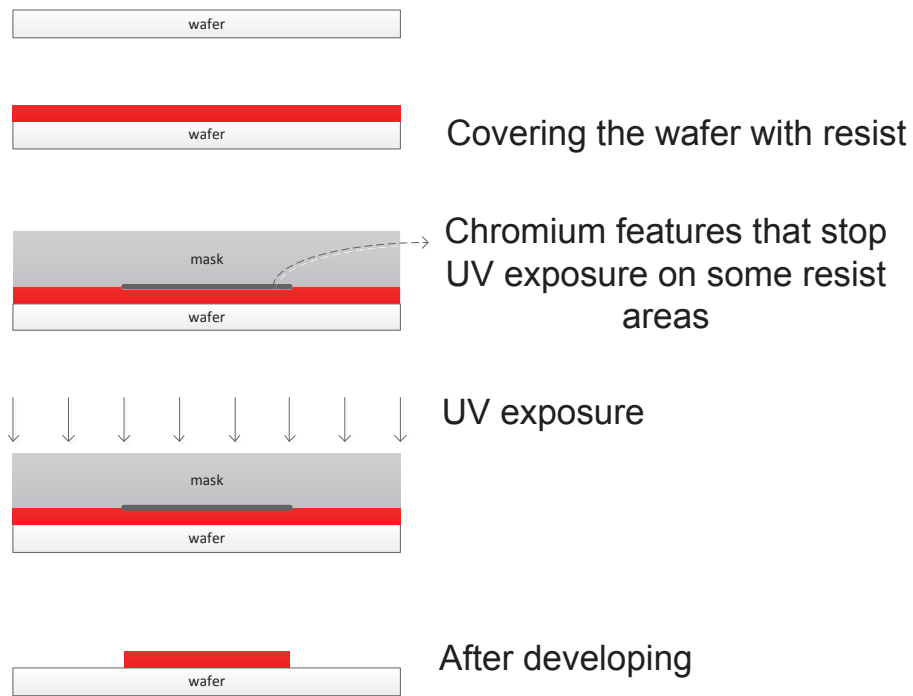
Figure A.6. Wafer cross-section and the steps taken in lithography.

Alignment
marks

HAMID MOGHADAS
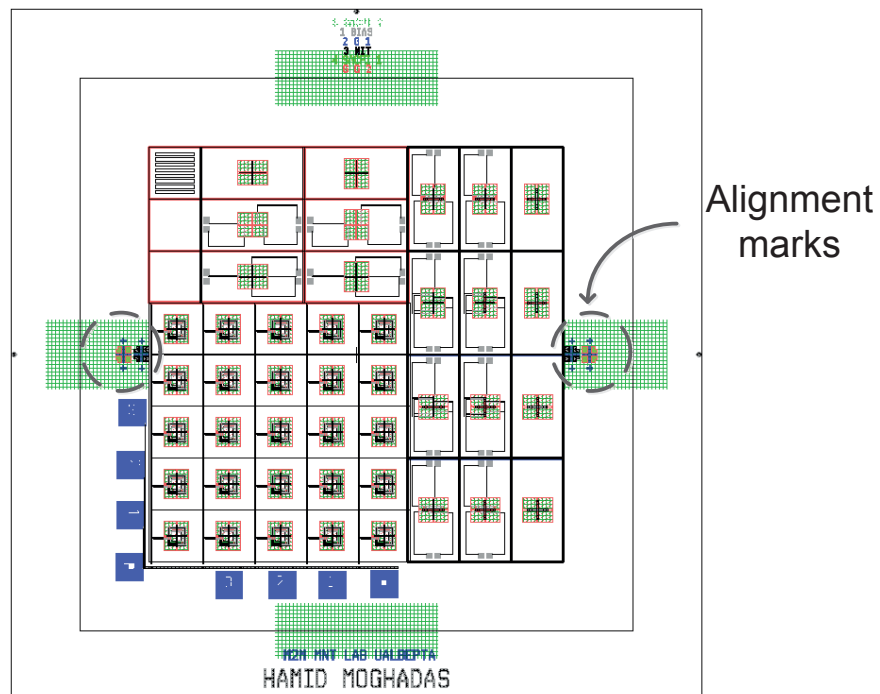
Figure A.7. All 6 masks on top of each other drawn in LEdit software and the optimum
position for placement of alignment marks.
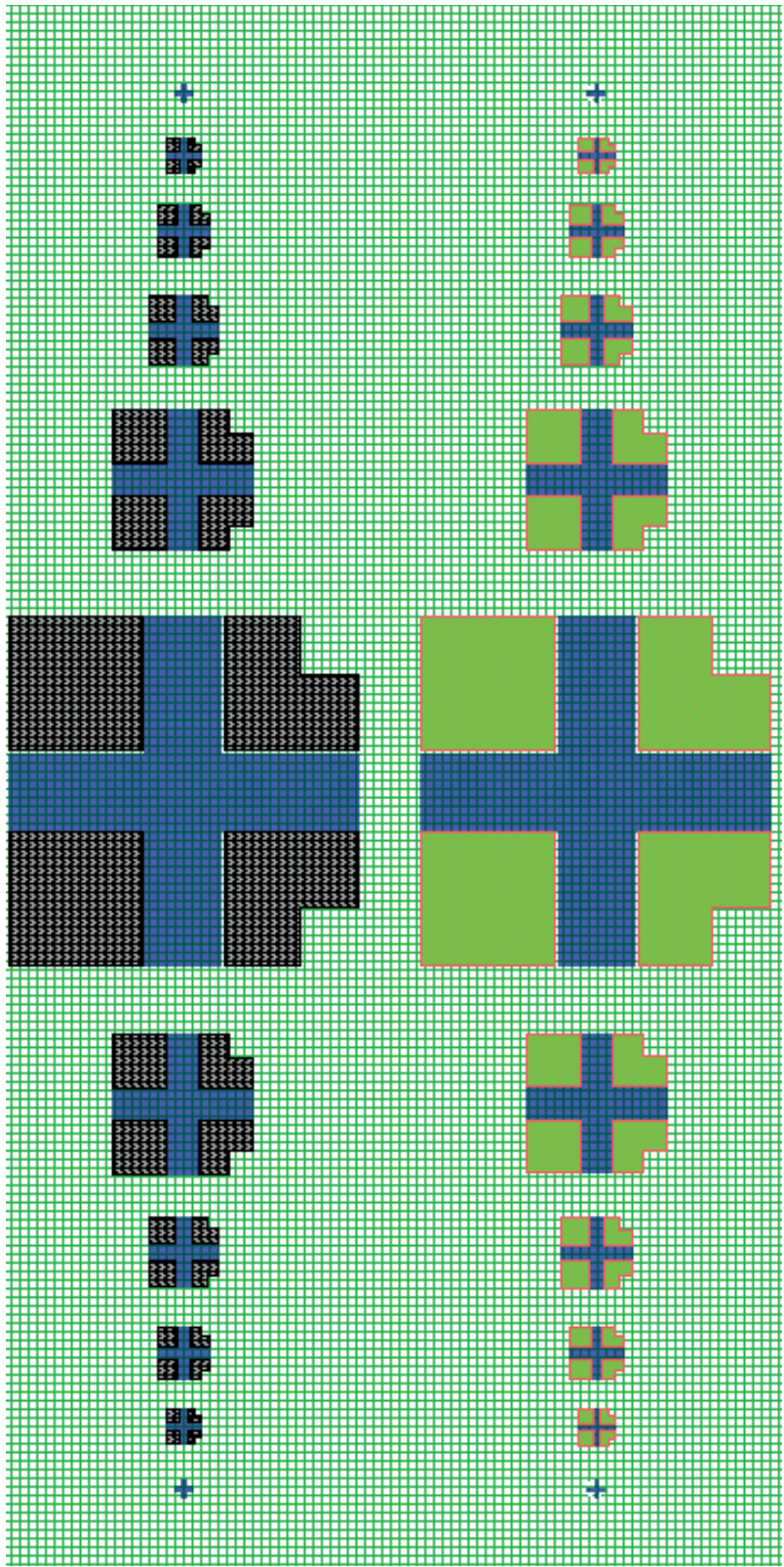
Figure A.8. Two sets of similar alignment marks.

113
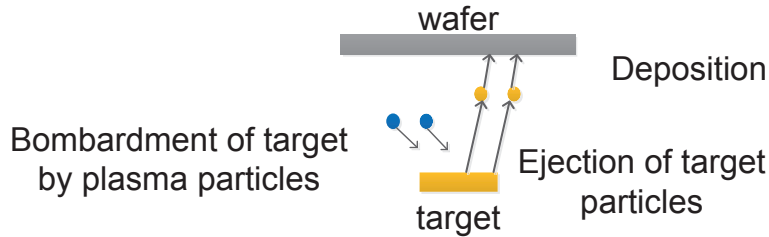
Figure A.9. The schematic of the sputtering process inside a vacuum chamber.

react with the material. As an example, Sulfur Hexa-Fluoride (SF_6) gas is used to etch Silicon Nitride. Figure A.12 shows the Trion RIE tool used in Nanofab facility.

A.1.5 Metal Electroplating

In electroplating process, both the wafer and a platinum coated electrode are kept inside a solution containing metal ions. Using a stir bar or a pump, the solution is circulated and a constant DC current is created between the wafer and the electrode. The DC current reduces the metal ions and forms a film of metal on the wafer. Prior to electroplating, the wafer has to be covered with a continuous conductive film in order to facilitate the current flow all over the wafer surface. In comparison to sputtered films, the electroplated films have much lower stress and are allowed to be much thicker. This is of significance for the MEMS cantilevers which need to be thick and low-stress. Figure A.13 shows the electroplating station used in Nanofab facility. The DC current source is shown in Figure A.14.

A.2 A Fabrication Process for Monolithic-Integrated MEMS-Tunable Antennas

Cleaning Wafers

Piranha cleaning is the standard process for removing organics and metallic contaminants from wafers in all cleanroom facilities. Piranha solution includes 96% Sulfuric Acid ($H_2 SO_4$) and 30% Hydrogen Peroxide ($H_2 O_2$) with a ratio of 3:1. Special care has to be taken during this process. The organics such as Acetone, IsoPropyl Alcohol (IPA) , and photo-resist are not allowed to be put into Piranha or even around the wet-deck where the process is performed since it will result in an explosion. In preparing the solution, Sulfuric Acid is added first because its volume is higher and chemically it is weaker. The solution temperature raises $100°C$. Hence, instead of plastic lab-ware, glass should be used. The wafers are kept in the solution for 15 minutes in Teflon carriers, then washed in dump rinser for 5 cycles and finally dried with Nitrogen gun. The process of the first layer is preferred to be done immediately after Piranha.

(a)

(b)

Figure A.10. (a) Magnetron Sputtering tool. (b) The control board

Washing with Acetone/IPA is an alternative for Piranha which is less dangerous and is practical for the precision and cleanliness that is sought for MEMS switches. The process steps are as follows:

✓ keep wafer in Acetone for 3 minutes

Figure A.11. Trion PECVD.

✓ agitate for 1 minute

✓ transfer the wafer from Acetone to IPA. This has to be done quickly since Acetone dries quickly on the wafer and leaves gunk and stain

✓ keep wafer in IPA for 3 minutes

✓ agitate for 1 minute

✓ wash with DeIonized (DI) water

✓ dry with Nitrogen gun

Deposition of DC Bias Lines

Layer 1 is a 80 nm thick and 10 μm wide, reactively sputtered Tantalum Nitride (TaN) layer forming DC bias lines of a resistivity value which varies between 1.6×10^5 to 1.3×10^5 Ω/Sq moving from wafer center to edges. Since TaN targets are not available, Ta targets are used and the presence of Nitrogen flow results in sputtering of TaN. Also, it should be noted that different Ta targets have to be used for regular and reactive sputtering in order to prevent cross-contamination between different processes. The steps are as follows:

✓ the vacuum chamber is pump-downed for 35 minutes to a base pressure of about 2×10^{-6} Torr. The pump-down step decreases the oxygen level in the chamber. For deposition of pure layers such as Gold, the pump-down time should be around 1 hour. But for a resistive layer, a 35 minute pump-down is enough since the Oxygen content is not going to damage the layer properties.

✓ an Argon flow of 30 standard cubic centi-meter (sccm) is turned on in the chamber

Figure A.12. Trion RIE.
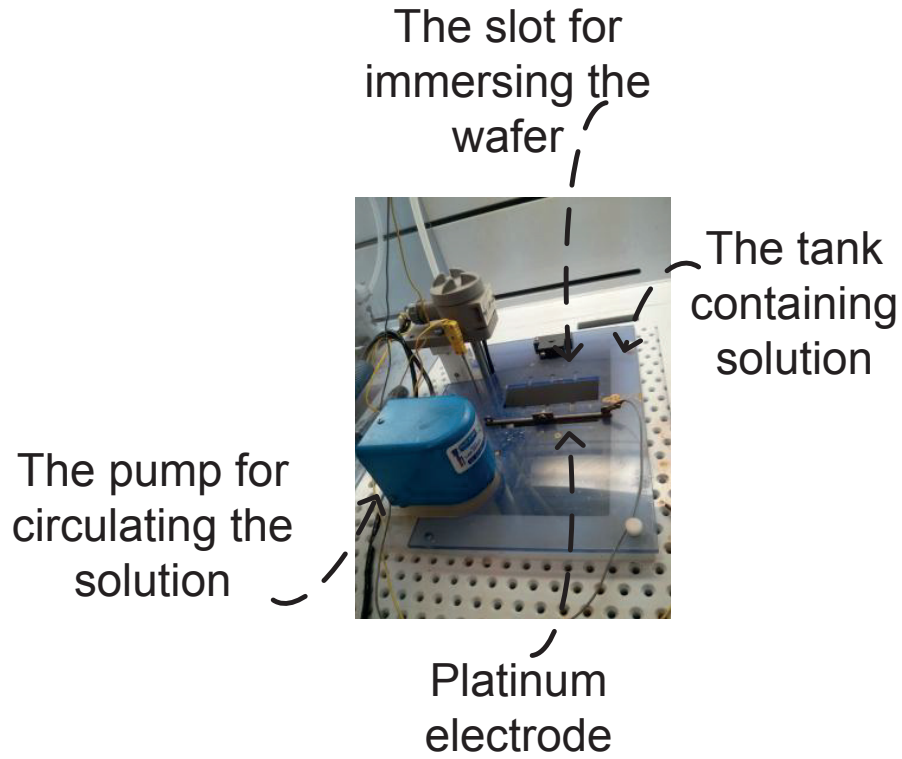
Figure A.13. Electroplating station.
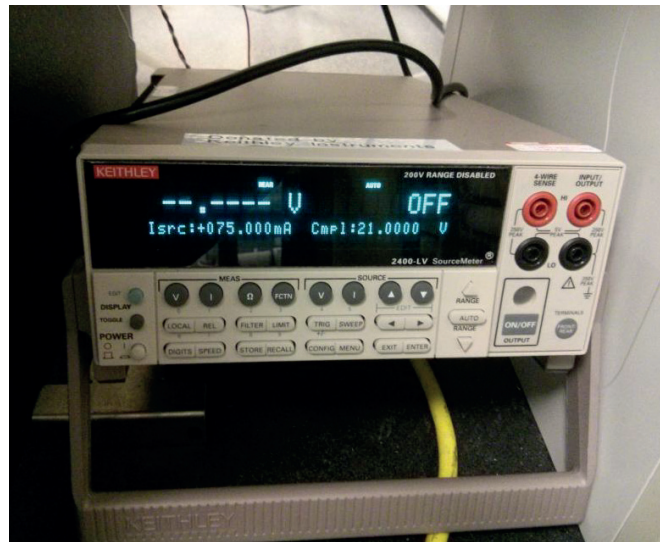
Figure A.14. DC current source used at electroplating station.

✓ the chamber pressure is set at 0.007 mTorr to form a plasma under a power of 300 Watt and frequency of 150 kHz

✓ after the plasma is stabilized, the Nitrogen flow of 20 sccm is turned on and the chamber pressure is set at 0.004 mTorr

✓ the deposition of about 8:20 minutes results in the desired thickness and resistivity

Patterning DC Bias Lines

This layer can be patterned by either etching or lift-off depending on availability of tools:

Etching Bias Lines

A photo-lithography by positive optical mask and a positive-tone photo-resist such as HPR504 prior to etching, transfers the desired patterns to wafer. After lithography, the wafer should be hard-baked at about $130°C$ to prevent total burning and etching of the resist inside the etching tool. The hard bake temperature of $130°C$ is picked since it is about 10% above HPR504 regular baking temperature. Etching of TaN is done by ion mill tool. In this machine, TaN is physically removed by bombardment of ions in an Argon plasma.

Usually, the photo-resist mask on the wafer is washed by Acetone and IPA after etching. But with this method, an extra step is required to remove it because the resist hardens under ion bombardment and sticks to TaN features. Oxygen stripping process inside Trion Reactive Ion Etching tool can remove the hardened resist. The etch rate for regularly baked HPR504 is about 1.9 nm/sec. In order to calculate the required stripping time, half of this removal rate is assumed.

It is important to make sure that the HPR504 is totally removed. Leaving a very thin layer of resist on the wafer can easily disrupt the next layers and ruin the operation of MEMS devices. Hence, the TaN features have to be inspected carefully for resist gunk under microscope afterwards. Another way to make sure about removal of resist is to use step-height profilometer. This device has a fine stylus that can move on top of features and draw its exact step profile within an accuracy of 10 nm. Presence of unexpected roughness and features on top of the TaN features can be a sign of presence of resist gunk.

Bias Line Lift-Off

If the ion mill tool is not available, lift-off has to be performed. In this method, the reverse of the desired pattern is transferred to the wafer before sputtering of TaN. The pattern transfer is performed by optical-lithography of a dual layer positive resist with a negative mask. The dual layer resist includes a 1200 nm thick HPR504 on top of LOR5B which is a 460 nm thick non-photo-sensitive resist. The process steps are as follows:

✓ Clean bare wafers are put inside HMDS chamber. This process form a layer on top of Quartz to promote the adhesion of resists.

✓ Pour 5 mL of LOR5B at the wafer center, spread for 10 sec at 500 rpm , spin for 40 sec at 3000 rpm

✓ Bake on hot-plate for 5 min at 150°

✓ Let the wafer cool and rehydrate for 5 min.

✓ Pour 8 mL of HPR504, spread for 10 sec at 500 rpm, spin for 40 sec at 4000 rpm

✓ Bake for 90 sec at 115°

✓ Let the wafer cool and rehydrate for 10 min

✓ Expose as single-layer HPR504 for 2.2 sec

✓ Develop for 45 sec inside Dev354

✓ Rinse with DI water and dry using Nitrogen gun

✓ Bake for 120 sec at 115°

✓ Let the wafer cool and rehydrate for 12 min

✓ Develop for 15 sec inside MF319 for an undercut of up to 5 um

Immediately after TaN sputtering, the wafers are put in PG Remover bath for 24 hours in face-down position. The face-down position helps the separation of the unwanted TaN features from wafer. The long time required for the process is due to using the PG Remover at ambient temperature. If the solution warm-up to $60°C$ is allowed in the clean-room facility, the process time will be much shorter.

Deposition of Bottom Metal Layer

A magnetron-sputtered 10/150/10 nm Cr/Gold/TiW forms RF-MEMS switch bottom plates at layer 2. TiW is a 20:80% alloy of Titanium(Ti):Tungsten(W) used as the adhesion between Gold and Quartz wafer underneath and also between Gold and top dielectric layer. Also, the Chromium (Cr) layer is the adhesion between the Gold layer and the Nitride layer on top. If the same material is used for the adhesion layers on bottom and top of Gold, the wet etching of bottom adhesion layer causes over-etching of top adhesion layer. The sputtering of these 3 layers is performed consecutively in the same sputtering chamber without breaking the vacuum. The process steps are as follows:

✓ the vacuum chamber is pump-downed for 1 hour to a base pressure of about 1×10^{-6} Torr

✓ an Argon flow of 50 sccm is made in the chamber

✓ the chamber pressure is set at 0.007 mTorr to form a plasma under 200 Watt for TiW, 75 Watt for Gold, and 300 Watt for Cr

✓ the deposition of about 2 minutes for TiW, 18 minutes for Gold, and 2 minutes for Cr results in the desired thickness

Patterning of Bottom Metal Layer

The patterns are transferred to wafer using optical lithography with positive mask and positive-tone HPR504 photo-resist. To etch the metal layers, wet process is performed. The TiW is etched by 30% Hydrogen Peroxide with a rate of about 4.1 nm/min. Since Hydrogen Peroxide is transparent, the process is visually controllable. As soon as the silverish color of wafer turns to shiny yellow, the etching is

enough.

The Gold etchant is a dark amber pre-made solution containing water, Iodine, and Potassium Iodine. Although this process happens at the known and approximate etching rate of 5.3 nm/sec, the wafer can not be left inside the solution since it is dark. During etching, the wafer has to taken out of the solution by the tweezers in order to visually check the color. The process finishes as soon as the yellow color of wafer turns to silver.

The Cr etchant is a bright orange liquid which contains Ceric Ammonium Nitrate, Nitric Acid and water. Since this liquid is a super fast etchant and the Cr layer is thin, the process is not controlled with time. The whole process takes less than 15 sec depending on agitation. The wafer should be transferred out of etchant as soon as the Quartz surface appears.

Immediately after the patterning of the 3 metal layers, the HPR504 mask has to be cleaned by acetone and IPA. The Gold sputtering results in a very flat layer. But the presence of two different and thin adhesion layers on top and bottom of Gold results in high roughness. Keeping the HPR504 mask on wafer for several days on such rough layer can make the complete removal of resist impossible.

Deposition of Insulating Layer

Layer 3 is a Plasma Enhanced Chemical Vapor Deposition (PECVD) Silicon Nitride (SiN) which insulates switch top and bottom plates. Trion PECVD tool deposits a 400 nm thick layer of SiN in about 1050 seconds. This step happens at pressure of 500 mTorr, RF power of 40 Watts, and temperature of $300°C$. Prior to deposition, the initial steps of chamber cleaning and conditioning have to be performed without any wafer inside, to remove the depositions from previous users inside the chamber and make the chamber conditions ready. After conditioning, the wafer chuck is hot. Special care has to be taken for placing wafers on the hot chuck. To prevent wafer breakage due to thermal stress, the wafer should be kept for a while by tweezers at several centimeters on top of chuck to warm up. Using plasma in this process allows it to happen at a much lower temperature. After deposition of metal layer on wafer, special care has to be taken about the temperature of next layers since high temperature can easily melt and re-sputter the metal layer.

Patterning of Insulating Layer

The desired pattern of Nitride layer is transferred to the wafer by positive mask and positive-tone photo-resist optical-lithography. The dry etching of Nitride is performed by Trion Reactive Ion Etching (RIE) tool in 150 seconds. It should be noted that the etch rate of HPR504 mask is equal to Nitride. Prior to RIE, the chamber is cleaned at high power for 20 min.

Dual Sacrificial layers

Layer 4 and 5 are the dual photo-resist sacrificial layers made of LOR 5B and HPR504. This layer is implemented exactly the same as the dual-layer resist that is used for lift-off of the first layer.

Deposition of Top Metal Layer

A 30/100 nm Cr/Gold layer should be magnetron-sputtered as the seed for electroplating of a 1.5 um thick Gold layer under 75 mA in a Techni-Gold 25 E S non-cyanide solution of pH 7.23. In this method, the wafer is kept at a fixed distance of 4 cm parallel to a Platinum electrode inside the solution at $60°C$ while the solution is circulated inside the tank using a pump. A voltage of about 2.8 Volts is read between the wafer and electrode. The deposition rate, the uniformity, and the roughness of the resulting Gold layer depends on the DC current applied to the wafer. The current value should be optimized for the specific setup and wafer area.

Patterning the Top Metal Layer

The desired patterns are transferred to the wafer using optical lithography, positive mask, and positive-tone photo-resist. The etching is done the same as the wet process used for bottom metal layer. Special care has to be taken while etching of this 1.6 um thick layer. Because of the non-uniformity of etch rate across the 4 inch wafer, when the wafer edges are etched completely, the wafer center will be incomplete. This can result in over-etching of the Gold features around the wafer edges. Hence, an alternative method should be adopted for thick layers. Instead of using tweezers to hold the wafer edges and intermittently immersing the wafer in the etchant, the wafer should be placed in a Teflon wafer cassette and gently moved back and forth inside the solution. The solution level of several millimeters on top of wafer makes it easy to observe the process advancement.

Wafer Dicing and Release

Prior to dicing, the wafer is coated by a protective HPR504 photoresist layer and then baked for 1 minute at 100° C. The switch dies and unit cells are diced and then released in a combination of dry and wet steps. The dry step is done by Reactive Ion Etching (RIE) under Oxygen-sripping recipe for 2700 seconds. The wet step includes soaking in Actone, MF319 and Isopropyl Alcohol for 30, 5, and 5 minutes respectively. MF319 is the commercial developing solution for LOR 5B. There is a high risk of stiction of MEMS cantilever to bottom electrode after samples are transferred out of Alcohol dish. Hence, the samples are finally dried in a Critical Point Drier by Carbon Dioxide to avoid stiction.